NONLINEAR DYNAMICS OF COUPLED CAPILLARY-SURFACE OSCILLATORS

A Dissertation

Presented to the Faculty of the Graduate School

of Cornell University

in Partial Fulfillment of the Requirements for the Degree of

Doctor of Philosophy

by

David Michael Slater

August 2011

NONLINEAR DYNAMICS OF COUPLED CAPILLARY-SURFACE OSCILLATORS

David Michael Slater, Ph.D.

Cornell University 2011

The nonlinear dynamics of coupled liquid droplets and bridges are examined. By restricting droplet and bridge shapes to equilibrium states, the quasi-static dynamics of such systems may be studied using ordinary differential equations, and the techniques of nonlinear dynamics may be applied. For example, liquid droplets are restricted to spherical-caps, whose shapes may be deduced solely from their volume.

Networks of liquid droplets are first considered. Static solutions are grouped into families, each with some p droplets large and some $q = n - p$ small. The two-droplet system is modeled as a conservative second-order oscillator and fixed points undergo a pitchfork bifurcation as the total volume is increased; furthermore, when subjected to periodic forcing, chaotic dynamics are possible. Bounds for chaotic dynamics are investigated by using Melnikov's method and calculating Lyapunov exponents. Results are compared qualitatively with experimental results, thereby confirming the existence of chaotic motions.

The two-droplet model is then extended to a n-droplet frictionless S_n symmetric model that consists of $n - 1$ second-order differential equations. Symmetry of the system is fundamental. In particular, independent of the equations, fixed-points may be grouped into families by the number of small and large droplets. Within the families, stability is invariant and hence significantly reduces the number of equilibria to be considered. All equilibria, and their associated stability, are

calculated analytically for an arbitrary number of droplets.

For three droplets, the system is fourth order and thus trajectories are (in general) quasi-periodic or chaotic. Because the equations are S_3 symmetric, trajectories may also possess S_3, or one of the three flip symmetries. Since there is no dissipation there are no asymptotically stable attractors. As such, trajectories of interest are away from equilibrium. In particular, trajectories with no initial velocity are analyzed to ascertain their symmetry as well as their dynamic nature. Both these determinations may be done in an automated fashion through the use of symmetry detectives and Lyapunov exponents, respectively. For this system, the results of these two methods reflect a strong correlation between symmetry and nonlinear dynamics; chaotic trajectories are S_3 symmetric while quasi-periodic trajectories possess one of the three flip symmetries.

Next, a non-smooth switching bridge-droplet system is considered. The system has two states: droplet-droplet and bridge-droplet. The switching system can be obtained from the two droplet system by introducing a planar substrate below one of the droplets. As the system oscillates, it may transition between states if the droplet impacts the wall or the liquid bridge breaks. The two transitions occur at different places in state space which results in a region for which the system is multiply defined. In addition, transitions are assumed to be instantaneous with no loss of velocity. The two states are first analyzed separately. The bridge-droplet state undergoes a cusp bifurcation in a two parameter expansion. Boundary equilibrium bifurcations also occur when an equilibrium point collides with a non-smooth boundary. If the bridge-droplet and droplet-droplet states are combined, a two parameter bifurcation diagram for the switching system is realized. Switching trajectories are of particular interest because each switching cycle dampens the system until it no longer switches. These trajectories are mapped into a semi-

infinite cylindrical space in which long-term behavior can be described solely by the dynamics in the multiply defined region.

In the final chapter models for pull-off adhesive failure are considered. Recognizing engineering applications (i.e. a capillary adhesion device) as well as a phenomenon found in nature (i.e. defense mechanism of palm beetle), models for pull-off adhesive failure are developed for different loading conditions and compared with available observations. In particular, array geometry and the relationship of adhesive failure to the instabilities of a single liquid bridge are emphasized.

BIOGRAPHICAL SKETCH

David Slater has always been drawn to the variety of complex problems found in Mathematics (his other true interest being ice hockey).

While studying Mathematics at Michigan Technological University, David was recognized in 2005 as the Norman E. Scholz Math Department Scholar (top graduating mathematics major); in 2004, he received a Mathematics Achievement Award (one of the top junior Mathematics majors). During Summer 2004, he attended a Math REU at Carnegie Mellon University, at which he met his wife (and also studied Variational Calculus). In Fall 2005, he became an Applied Mathematics Student and Teaching Assistant at Cornell University. Assuming this dissertation was well received, he earned a Ph.D. in Applied Mathematics with Minors in Theoretical & Applied Mechanics and Mathematics in May 2011.

For Anna, without whom none of this would have been possible.

ACKNOWLEDGEMENTS

I would first like to thank my wife for pushing me when I needed it, always being there when I needed her, and critiquing my work as 'Editor' of my papers. Thank you to my parents, and my brother and the rest of my family for their support.

Over the years, a variety of my fellow graduate students have helped me in this work as well as helped me keep my sanity. I have also had the privilege of learning from some of the world's best faculty. Special thanks to my committee: Richard Rand, Steven Strogatz, Timothy Healey, and, of course, my advisor Paul Steen (who helped me even *before* I attended Cornell). Thank you to the Math and Computer Science Departments for the opportunity to teach a variety of classes, and finally, the approximately 1,000 undergraduate students who have had to listen to my rambling.

TABLE OF CONTENTS

LIST OF TABLES

LIST OF FIGURES

CHAPTER 1

INTRODUCTION

A capillary surface is a liquid-gas (or liquid) interface whose shape is determined primarily by surface tension[3]. Since force due to surface tension scales with surface area, capillary surfaces occur (for typical liquids such as water) on the millimeter or smaller scale where the ratio of surface area to volume is high. A coupled set of capillary surfaces is a capillary system; these systems often exhibit highly complex dynamics. It is important to note that, in such a system, the surfaces must be small but they may be part of a larger system (e.g. the veins of a leaf in a tree). Examining the nonlinear dynamics of microfluidic capillary systems is the objective of this dissertation. In particular, the focus of study is motion of coupled liquid droplets and bridges.

When a capillary system is set in motion, inertia and/or viscous forces may (in addition to surface tension) influence the shape of liquid-gas interfaces as well as the overall system's motion. In general, when analyzing the system, the dynamics are found via solving the Navier-Stokes equations for the underlying flow. As these are partial differential equations, their solutions reside in an infinite dimensional space, in which it is often difficult to apply the methods of nonlinear dynamics. In many cases, the dynamics "shadow" trajectories of static equilibrium shapes – a phenomena referred to as 'quasi-static dynamics.' In such quasi-static systems, each element is in equilibrium with a fixed pressure. However, different elements may have different pressures so that the *system* is out of equilibrium even though each element is in equilibrium. In this way, a good approximation of a system may be obtained by limiting capillary surfaces to one-dimensional families of static equilibrium shapes. Such an approximation has the advantage that systems may

be modeled with ordinary differential equations rather than partial differential equations.

In this work, the shapes of individual capillary surfaces in 'capillary-inertia' models are restricted to static equilibrium states. Liquid viscosity and other sources of dissipation are assumed to be either negligible or small whereas liquid inertia and capillary pressure are influential due to their tendency to distort and restore deviations from equilibrium shapes. It has been shown that water droplets in air (on earth) are well approximated by their static equilibrium shapes on scales ranging from a few millimeters to tens of microns[4]. Note that a low-gravity environment (e.g. the space station) considerably expands the range of appropriate sizes. As such, examination of capillary-inertia models at these length scales is justified.

For example, consider a millimeter-size droplet resting on a flat plate. A liquid droplet is in static equilibrium when surface tension (due to curvature of the surface) balances the pressure difference across its interface. This balance is given by the Young-Laplace equation

$$\Delta P = \gamma \left(\frac{1}{R_1} + \frac{1}{R_2} \right) \tag{1.1}$$

where ΔP is the pressure difference, γ surface tension, and R_1 and R_2 the interface's principal radii of curvature. Since the droplet has fixed volume, the Young-Laplace equation must be solved subject to a volume constraint. The resulting spherical-cap shape persists if volume is changed quasi-statically. Note that a spherical-cap is S_1 symmetric; it then follows that a family of spherical-cap droplets is one-dimensional. Hence, the family may be parametrized in terms of droplet volume, height, or center-of-mass, knowing any of which yields the droplet shape.

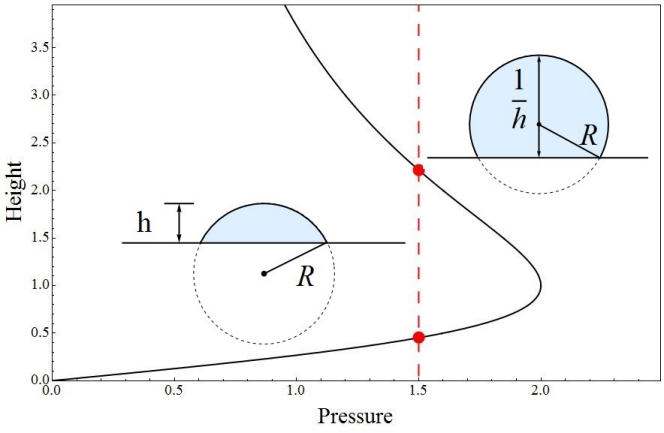

Figure 1.1: Pressure-height diagram for a single droplet with height scaled by droplet radius. For any pressure, two droplet static equilibria corresponds to droplets with height h and $1/h$.

Under the quasi-static assumption, a fixed volume droplet cannot oscillate. Therefore, in order to achieve oscillation two coupled droplets are required. For example, consider two droplets pinned at the ends of a cylindrical tube so that volume may exchange between them. The droplets' static equilibrium shapes are spherical caps, which implies the entire system is symmetric about the center line and, as such, may be modeled by tracking the center of mass axially. Using Newton's second law results in a second order ODE with two parameters: total volume and tube length[1]. In this manner, an infinite dimensional problem (PDE) is reduced to finite dimensions (ODE) where stability may be calculated analytically and methods of nonlinear dynamics may be applied.

For any number of coupled droplets, the criterion for static equilibrium is that they share a common pressure difference ΔP across their respective interfaces. When viewing ΔP in the context of the Young-Laplace equation (1.1), coupled with the fact that a spherical-cap has a single radius of curvature, we know $R_1 = R_2$ and hence all droplets have equal radius of curvature. Plotting the spherical-cap pressure against its height (Figure 1.1) shows that for any given pressure a droplet

may be in one of two states: 'small' or 'large'. Since any of the droplets may assume either state, there are 2^n equilibrium configurations, consisting of p small droplets and q large for all p and q such that $p + q = n$[5].

The two droplet system is considered in greater detail in Chapter 2 in which the system, subject to small forcing and dampening, is analyzed. Under these conditions, the system may exhibit chaotic dynamics. Bounds for chaos are obtained through the use of Melnikov's method and the computation of Lyapunov exponents. Although the model has been reduced to two dimensions, it remains highly nonlinear and convoluted. As such, analytic results are obtained when possible and numeric techniques are used when appropriate. Predictions obtained from the model are compared with experiments for water droplets of millimeter size. Such comparisons also exist for the unforced droplet-droplet oscillator[1] and reaffirm the validity of the models.

If an arbitrary but substantial number of droplets, n, are coupled through a central chamber (or reservoir of sufficient size), the system may be thought of as S_n symmetric (Chapter 3). Due to symmetry the ordering of droplets is arbitrary. The symmetry of the system is two-fold; the spherical-cap assumption allows a $2n - 2$ degree ordinary differential model, while the symmetric network plays a fundamental role in the structure of equilibria and the dynamics of trajectories. Since ordering of droplets is arbitrary, of the 2^n equilibria, only $n + 1$ need be considered. In other other words, instead of examining all equilibria with p large and q small, only one in the equivalence class need be considered. Equilibrium branches, bifurcation points and stability of equilibria are calculated *analytically* for a network of arbitrary size.

All equilibria from the frictionless model presented in Chapter 3 are centers

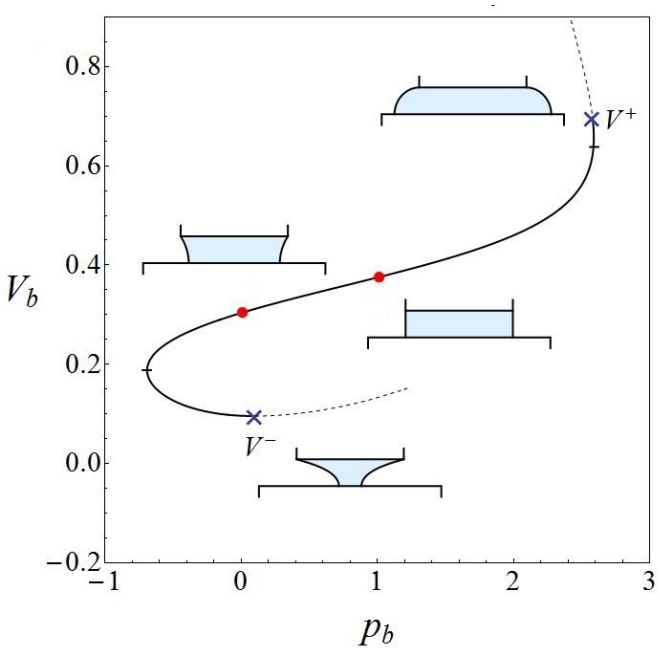

Figure 1.2: Pressure-volume diagram for liquid bridge with pinned contact at one end and fixed contact angle 90° at the other.

and saddle-points, implying there are no traditional stable attractors. Thus, when examining trajectory dynamics, solutions away from equilibria are of most interest. The three droplet four dimensional system is discussed in Chapter 4. In this system, trajectories are quasi-periodic or chaotic, but also may possess symmetry. For trajectories starting from rest, Lyapunov exponents are calculated to ascertain if a solution is chaotic and the method of symmetry detectives is employed to determine possible symmetry. Both methods can be applied in an automated fashion on a grid of initial conditions. Note that this use of symmetry detectives differs from its traditional use (symmetries of attractors). With respect to the three droplet model, there is a strong correlation between symmetry and nonlinear dynamics; chaotic trajectories are found to be S_3 symmetric while quasi-periodic trajectories possess one of the three possible flip symmetries (Z_2).

Thus far, only considered one type of capillary surface – a liquid droplet – is

considered. Chapter 5 incorporates a second class of capillary surfaces, namely liquid bridges with a pinned circular contact line at one end and a fixed contact angle of 90° at the other. For such bridges, the static equilibrium shapes are, as with liquid droplets, determined by solving the Young-Laplace equation (1.1). Equilibrium shapes are axisymmetric and may be written in terms of incomplete elliptic integrals[6]; however, in this study, it is more convenient to solve the Young-Laplace equation numerically. The family of equilibrium shapes is one dimensional (like with the droplet), and may be parameterized in terms of the bridge volume. Note that while multiple bridge equilibria may occur at a single bridge volume, only one is stable.

The family of bridge equilibria differs from that of the droplet since it has both a maximum and minimum admissible volume (Figure 1.2). Upon reaching either the maximum V^+ or minimum V^-, the bridge breaks. At V^+, the bridge blows out, whereas at V^- it breaks and reforms as a liquid droplet. Let us now reconsider the two droplet system. If a substrate is introduced, in the course of oscillation, one of the droplets may impact and form a liquid bridge. The system is then in a bridge-droplet state and will continue to oscillate; a second transition may occur if the liquid bridge breaks. These transitions are treated as non-smooth instantaneous events. Furthermore, these transitions occur at different places in phase space, resulting in a region where the system is multiply defined. A model for this non-smooth switching system is formulated and analyzed in Chapter 5. The bridge-droplet state is discussed first and a two parameter bifurcation diagram is obtained. The bridge-droplet and droplet-droplet states are then joined in a switching model. Bifurcation structure and the behavior of trajectories are discussed.

Motivation for this study of droplets and bridges arises from practical applica-

tions such as liquid lenses and capillary adhesion devices. For a traditional hard lens the focal length is changed by mechanically moving it. In contrast, a *liquid* lens has the advantage that focal length may be altered by varying its shape. In the context of liquid lenses, regular oscillations are desirable. As such, the bounds obtained are used to avoid chaotic dynamics. The two droplet system studied in Chapter 2 has successfully been used as a liquid lens[7, 8].

The second application is development of capillary adhesion devices. Such a device consists of an array of some large number of liquid droplets coupled via a central reservoir. If a substrate is pressed against the droplets they, will switch to bridges, causing the array to adhere to the surface by capillary adhesion. The study of capillary adhesion is inspired by the defensive abilities of the palm beetle. The beetle adheres to a surface by manipulating a multitude of tiny oil liquid bridges between its feet and a surface[9, 10]. This adhesion is remarkable because the beetle can attach and detach repeatedly in a fraction of a second and withstand being pulled on by a force of up to sixty times its own weight. Naturally, in an attempt to achieve reversible adhesion on the scale of permanent bonding adhesives, there is continued interest in duplication of the beetle's attributes[2]; this can be achieved by the use of arrays of liquid droplets[11]. Models for pull off adhesive failure for both a capillary adhesion device and the beetle are posed in Chapter 6. Results are discussed relative to available experimental observations. The effect of varied array geometry and the relationship between adhesive failure and the instability of a single liquid bridge is discussed.

Historically, the study of liquid droplets and bridges has focused primarily on the determination of static equilibrium states and their stability[12, 13, 14, 15]. More recently, scavenging models for networks of droplets has been studied, where

liquid flows between droplets due to pressure differences[16, 5]. In such models, the rate of change of droplet volumes are determined entirely by pressure differences. In contrast, in this work Newton's second law is used to to model the center-of-mass of the system. This results in models that include both the force due to the pressure differences and the effect of inertia due to the velocity of the flow. Such 'capillary-inertia' models describe both the position and the velocity of the center-of-mass of the system. Prior to this dissertation, a model for two coupled droplets was proposed by Theisen et. al[1], and serves as a base case for the systems described here.

The 'capillary-inertia' models obtained in this dissertation consist of ordinary differential equations. This is ideal as the techniques of nonlinear dynamics may be applied, allowing equilibrium states, bifurcations and transitions to chaos to be described in clear and understandable ways. In contrast, using the Navier-Stokes equations to model the fluid flow involves the analysis of partial differential equations[17, 18] where the methods of nonlinear dynamics are far more complicated. In Chapter 2 as well as in Theisen et. al[1] it can be seen that experiments are well approximated by ordinary differential equation models on length scales of interest.

This dissertation is structured as follows. In Chapter 2 the chaotic motions of the two droplet system are studied. Bounds for chaotic dynamics are obtained and compared with experiments. The two-droplet model is extended to any number of S_n symmetric droplets in Chapter 3. Analytic bifurcation and stability results are obtained for a system of arbitrary size. Chapter 4 explores the dynamics of three frictionless S_3 symmetric droplets. Solutions are classified as chaotic or quasi-periodic through the use of Lyapunov exponents and their symmetry is determined

using symmetry detectives. In Chapter 4, the class of capillary surfaces is extended to include liquid bridges. In particular, a switching non-smooth bridge-droplet model is considered. Bifurcation results are obtained and the dynamics of switching trajectories are discussed. In Chapter 6, models for pull-off adhesive failure are discussed for various loading conditions and geometries. Finally, in Chapter 7 future work is discussed.

CHAPTER 2

CHAOTIC MOTIONS OF A FORCED DROPLET-DROPLET OSCILLATOR[1]

Abstract

A model for the motion of two coupled spherical-cap droplets subject to periodic forcing is studied. The inviscid unforced model is a conservative second-order system, similar to Duffing's equation. Surface tension resists the inertia of deformations from the spherical shape. Steady-states of the system are parameterized by the total combined volume of the two droplet caps. The family of equilibria exhibits a classical pitchfork bifurcation, where a single lens-like symmetric steady state bifurcates into two droplet-like asymmetric states. The existence of homoclinic orbits in the unforced system suggests the possibility of chaotic dynamics in a forced, damped system. The forced damped extension is investigated for chaotic dynamics using Melnikov's method and by calculating Lyapunov exponents. Observations are compared qualitatively with experimental results, confirming the existence of chaotic motions.

2.1 Introduction

With the recent advances in microfluidics, the dynamics of small liquid droplets has increased in interest. At such scales, where surface tension often dominates, a liquid droplet will tend to a spherical shape under the action of capillarity. A

[1]D.M. Slater, C. A. López, A. H. Hirsa, P. H. Steen, *Chaotic motions of a forced droplet-droplet oscillator,* Physics of Fluids, **20** (2008), p. 092107 Reprinted with permission.

classic example of capillary dynamics is the Rayleigh vibration of a sphere where surface tension tends to restore shape deviations due to liquid inertia[19]. The system we consider is a variation on the Rayleigh problem.

Consider two spherical droplets each pinned to opposite ends of a cylindrical tube of length $2L$ (Figure 2.1). Liquid is allowed to flow through the tube from droplet to droplet. By restricting to spherical-cap deformations, the dynamics of this system can be modeled as a second-order nonlinear dynamical system. Theisen *et al.* explored the dynamics of the unforced (conservative) model of this coupled droplet oscillator [1]. The steady-states are parameterized by the total droplet volume, $V_1 + V_2$. As $V_1 + V_2$ is increases a pitchfork bifurcation occurs, whereby a symmetric steady state (lens-like), corresponding to two symmetric caps, bifurcates into two mirror-symmetric steady states (droplet-like), corresponding to one large and one small cap. Figure 2.1 shows typical lens-like and droplet-like configurations.

In this paper, we study the system subjected to sinusoidal forcing of amplitude γ and frequency ω, where a viscous resistance δ is also included. In experiment, this forcing might be supplied by ambient pressure oscillations on one side relative to the other. The unforced model is of second order; the addition of small amplitude sinusoidal forcing adds a third degree of freedom, allowing for the appearance of chaotic dynamics. We use the theory of nonlinear dynamics to explore the existence of chaos. The unforced model has homoclinic orbits for volumes past the bifurcation point. As a result, if the small forcing causes the stable and unstable manifolds of the saddle point to intersect, chaos is possible.

We employ two different approaches in our analysis. The first is Melnikov's method, which gives lower bounds for chaotic behavior. The second involves cal-

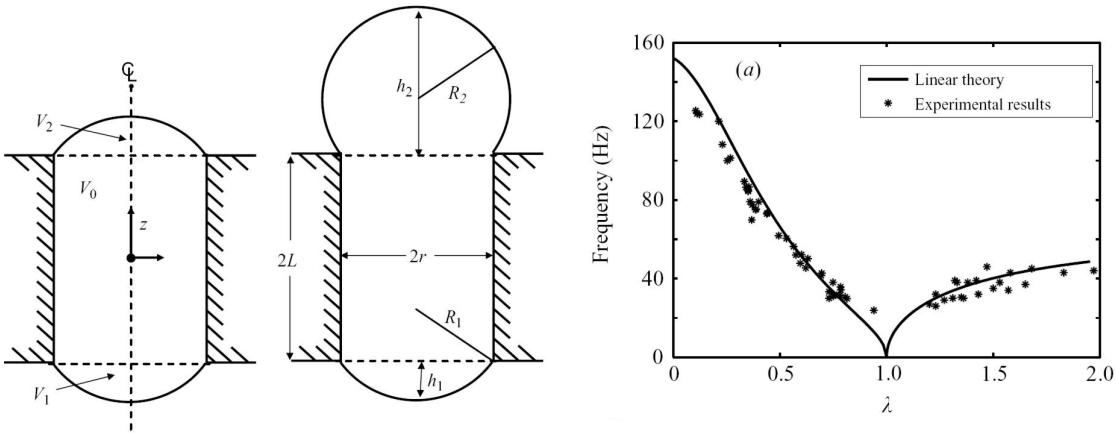

Figure 2.1: (a) Schematic of coupled droplets pinned at the ends of a tube of radius r. V_1 and V_2 are the volumes of the droplets. Typical equilibrium positions for droplets are a) lens-like for $V_1 + V_2 < (4/3)\pi r^3$ and b) droplet-like for $V_1 + V_2 > (4/3)\pi r^3$. (b) Dimensional vibration frequency for linear theory (solid line) and experiments (symbols)[1].

culating Lyapunov exponents for a grid of two parameters, which allows us to further characterize the chaotic regions of $(\gamma/\delta, \omega)$ parameter space. To our knowledge, this second approach has not been used to study the dynamics of coupled droplets or bubbles. Combined, results from these two methods provide a guide to experiments. The goal is to predict where chaotic behavior might be expected in parameter space for a system of two coupled micro-droplets.

The approach of this study is inspired by similarities of the oscillator model to Duffing's equation. Duffing's equation provides a simple model for the forced vibrations of a cantilever beam in the presence of two magnets[20], among others. Owing to the simplicity of the model, an explicit lower bound for chaos using Melnikov's method is obtained [20]. Additionally, Lyapunov exponents for Duffing's equation are calculated for a grid of forcing amplitudes and frequencies [21]. This further characterizes the chaotic parameter regime. For vibrations of the cantilever

beam, a sequence of experiments shows the existence of a strange attractor[22, 23]. These studies derive an experimental criterion for chaotic oscillations and thereby test the validity of Duffing's equation as a model for this mechanical system [24].

Techniques of nonlinear dynamics have been applied to bubble and droplet problems for several decades now. A review of such work up until 1997 is available [25]. Bifurcation diagrams and Poincaré maps, primarily, are used to illustrate the existence of chaotic dynamics, as well as to find bounds for cavitation of bubbles. Smereka et. al. use Poincaré maps to explore the vibrations of a single bubble under periodic forcing as well as the transition to chaotic dynamics using bifurcation diagrams[26]. Oh *et al.* examine chaotic bubble oscillations under the influence of electric fields using bifurcation diagrams and Poincaré maps [27]. Parlitz *et al.* use bifurcation diagrams to examine the period-doubling cascade to chaos for a driven spherical gas bubble in water [28]. Macdonald and Gomatam perform a bifurcation study of coupled free gas bubbles [29]. Simon *et al.* compute Poincaré maps and bifurcation diagrams to investigate an acoustically driven air bubble in water [30]. Szeri and Leal apply Melnikov's method to numerically compute lower bounds for spherical bubbles in an incompressible liquid under single and multiple forcing frequencies [31]. Chang and Chen use Melnikov's method to estimate the cavitation pressure of a spherical gas bubble [32].

Motivation for this study draws from a variety of applications. In a micro gravity environment, surface tension determines the shape of liquid/gas interfaces up to 1 meter length scales. Small fluctuations in the gravity level can give rise to forcing known as g-jitter [33]. These small fluctuations are often modeled as forcing perturbations. In earth's gravity, the shape of static droplets smaller than about a millimeter is nearly spherical. These droplets can be driven by external

forcing, such as ambient sound waves as in the experiments described below, or by internal forcing as by a periodically driven electro-osmotic pump placed in the tube between the droplets [11]. In the driven electro-osmotic switch, the pump is a porous material and, consequently, viscous effects tend to be more dominant in this application. Another application is liquid lenses. Droplets can be used as liquid lens, which have the advantage that focal length can be changed in real time by controlling the interface curvature [34]. In all of these cases, it is advantageous to have an understanding of when chaotic oscillations might occur, whether one wants to avoid chaos or to exploit chaotic dynamics to some benefit.

2.2 Conservative Oscillator Model

2.2.1 Model formulation

A dynamical model for the center-of-mass motions of two coupled spherical-cap droplets is first presented by Theisen *et al* [1]. The spherical caps of heights h_1 and h_2 are connected by a cylindrical tube of length $2L$ and radius r (Figure 2.1). Let V_1 and V_2 be the protruding volumes of the droplets. By symmetry, the center-of-mass of the system moves along the z-axis. Furthermore, the spherical-cap restriction means that deformation is characterized by one degree-of-freedom, $V_1 - V_2$, say.

Let Z_{cm} be the center of mass of the total volume. Assuming, for now, that viscous resistance is negligible, Newton's second law can be written,

$$\rho \frac{d^2}{dt^2}((V_1 + V_2 + 2\pi L r^2) Z_{cm}) = F_1 - F_2. \tag{2.1}$$

The capillary pressure gives rise to a force acting from the bottom droplet upwards, $F_1 = (\pi r^2)2\sigma/R_1$, and one acting from the top droplet downwards, $F_2 = (\pi r^2)2\sigma/R_2$, where R_1 and R_2 are the radii of curvature of the respective droplets.

As outlined in [1], a variety of variables can be chosen to characterize this system. A convenient choice is $(\theta, \lambda) \equiv (V_1 - V_2, V_1 + V_2)$ where volumes are scaled with $(4/3)\pi r^3$. Total volume corresponds to λ so that volume is conserved for λ constant. Furthermore, $\theta = 0$ is always an equilibrium solution in this coordinate system. Writing (2.1) in terms of (θ, λ), and scaling lengths with r and time by $\sqrt{\rho r^3/\sigma}$, one obtains the nonlinear oscillator equation,

$$\frac{d}{dt}(A(\theta,\lambda)\frac{d\theta}{dt}) + C(\theta,\lambda) = 0, \tag{2.2}$$

where

$$A(\theta,\lambda) = h_1 + h_2 + 3\ell \tag{2.3}$$

$$C(\theta,\lambda) = 9\frac{(h_1 - h_2)(1 - h_1 h_2)}{(h_1^2 + 1)(h_2^2 + 1)}. \tag{2.4}$$

Here h_1 and h_2, non dimensional but using the same notation as previous dimensional quantities, are given implicitly as $V_i(h_i) = 1/8h_i(3 + h_i^2)$ and $\ell \equiv L/r$ is the scaled half-length of the tube.

2.2.2 Equilibria and phase-plane dynamics

The oscillator equation is a conservative second-order ordinary differential equation. Figure 2.2(a) shows the bifurcation diagram for this system with corresponding typical steady shapes. For each $\lambda < 1$, equilibria consist of the unique lens-like state. At $\lambda = 1$, a pitchfork bifurcation occurs, resulting in two symmetric stable branches (anti-symmetric configurations) and one unstable branch (symmetric

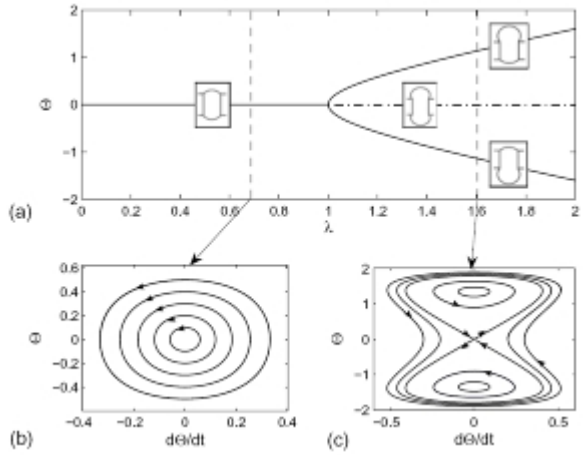

Figure 2.2: (a) Bifurcation diagram with typical equilibrium shapes sketched. Typical phase-plane solution for (b) $\lambda < 1(\lambda = 0.75)$ and (c) $\lambda > 1(\lambda = 1.6)$ (Adapted from [1]).

configuration). The two stable branches have one large droplet and one small droplet, while the unstable branch corresponds to two large droplets. This pitchfork bifurcation was confirmed in experiment in the context of the electro-osmotic switch [11] and pressure-activated switch [34]. For $\lambda < 1$, the dynamics consists of periodic orbits while for $\lambda > 1$ two families of periodic orbits surround the stable states. These periodic orbits are separated from a family of 'looping' orbits by two homoclinic orbits, spawned at the bifurcation. These homoclinic orbits, when perturbed by forcing and damping, can give rise to chaotic oscillations through a homoclinic tangle.

2.3 Weakly-damped Oscillator with Forcing

The conservative oscillator model is an idealization. For any experiment where liquid contacts a solid boundary, viscosity will play some role. For the theory, dissipation plays an important role in breaking the homoclinic orbits to form a tan-

gle. Viscous effects are characterized by a Reynolds number, $Re \equiv (r\sigma/\rho)^{1/2}(\rho/\mu)$, where μ is the liquid viscosity. Equation (2.2) has been generalized to include viscous damping [1],

$$\frac{d}{dt}(A(\theta,\lambda)\frac{d\theta}{dt} + C(\theta,\lambda) = -18Re^{-1}\ell f_* \frac{d\theta}{dt} \tag{2.5}$$

where the damping coefficient $f_* \sim 3.4$ has been estimated from transient decay experiments at conditions $(\lambda, \ell) = (1.2, 1.1)$ and has been shown to give predictions consistent with observation at other parameter values. For water and a tube diameter of $2r = 1.66\ mm$, one estimates $Re \sim 240$ from which the order of the viscous effects in equation (2.5) is immediate. Theisen *et. al.* discuss the range of Reynold's numbers for which the model is valid. The validity criterion is that the dampening term is small relative to the inertial term. For the range of λ values considered, this translates to the requirement $Re \gg 13$[1]. Thus for water and our tube size, the viscous effects are small, but non-negligible.

In experiment, forcing amplitude is controlled so as to be on the order of the damping. A forcing term $\epsilon\gamma cos(\omega t)$ is added to the eqn(2.5) where γ is the scaled forcing amplitude. The smallness of damping and forcing relative to inertia are characterized by $\epsilon = 18Re^{-1}$ and, since $\epsilon\delta \equiv 18Re^{-1}\ell f_*$, damping relative to forcing is given by $\delta = \ell f_*$, so that equation (2.5) with forcing can be written,

$$\frac{d}{dt}(A(\theta,\lambda)\frac{d\theta}{dt}) + C(\theta,\lambda) = \epsilon(\gamma cos(\omega t) - \delta\frac{d\theta}{dt}). \tag{2.6}$$

Here, for water and $\ell = 1.1$, $\epsilon \sim .075$ and $\delta \sim 3.73$.

Equation (2.6) is the equation studied in this paper. Fixing the forcing amplitude and frequency in experiment fixes the point $(\gamma/\delta, \omega)$ in the parameter-plane.

Note that the parameter with greatest experimental uncertainty is f_* and that f_* occurs only in δ. Hence, any change in f_* would result in a vertical shift of the point $(\gamma/\delta, \omega)$.

If $A = 1$ and $C = -\theta(a - 2b\theta^2)$ for $a, b > 0$, rather than the A and C given by equations (2.3) and (2.4), respectively, then putting $\theta(t) = x(t)$, equation (2.6) becomes the forced Duffing equation,

$$\frac{d^2x}{dt^2} - ax + 2bx^3 = \epsilon(\gamma cos\omega t - \delta\frac{dx}{dt}). \tag{2.7}$$

This equation has been analyzed extensively for its chaotic dynamics, as outlined in the Introduction. Two approaches are standard. Melnikov's method delivers a curve in the parameter-plane, above which chaos is possible. That is, sign changes in the Melnikov function imply the existence of a homoclinic tangle via the Smale-Birkhoff theorem; this in turn implies the existence of a horseshoe which may be stable or unstable. If stable, a strange *attractor* exists and chaos can be expected in experiment. Otherwise, the long-time solution need not be chaotic [21]. The second approach is to compute Lyapunov exponents along a trajectory in phase-space. Points in the parameter-plane are labeled as chaotic or not, depending on the behavior of the Lyapunov exponents, as judged by computation [21]. For equation (2.7), much is known about where chaos occurs in the $(\gamma/\delta, \omega)$ plane.

Ideally, a transformation between the orbit structure of the forced-Duffing (2.7) and that of equation (2.6) would be available. In particular, a transformation that preserves chaotic attractors would allow regions of chaos in one system to be mapped over to the other system. Unfortunately, such a transformation is not available, as far as we are aware.

Nevertheless, we proceed in the spirit of the ideal situation to obtain the results of the next section. First, the Melnikov approach is formulated and, for reference,

analytic expressions for the homoclinic orbit and the Melnikov bound for equation (2.7) are written down. Analogous analytic expressions for equation (2.6) are not available for arbitrary $\lambda > 1$, so attention is first restricted to $0 < \lambda - 1 \ll 1$. In this neighborhood, the homoclinic orbit is local to the origin of the phase-plane and a Taylor expansion in θ is productive. In this limit, an analytic expression for the homoclinic orbit is obtained and then inserted into the Melnikov function. Numerical integration then delivers a local approximation to the bound. Alternatively, for arbitrary λ, the homoclinic orbit is obtained computationally, inserted into the Melnikov function and numerically integrated. All approximations are restricted to the forced Duffing case as a check on the computational accuracy. Finally, to flesh out the Melnikov results, Lyapunov exponents are computed over a grid in the $(\gamma/\delta, \omega)$ plane.

2.4 Results of the Melnikov approach

The Melnikov function (e.g. [20]) is defined as

$$\Delta(\tau) = \int_{-\infty}^{\infty} \theta_o'(t-\tau)(\gamma cos(\omega t) - \delta\theta_o'(t-\tau))dt \tag{2.8}$$

where θ_o is an unperturbed homoclinic orbit and prime denotes derivative along an orbit. Here $\Delta(\tau)$ represents the distance between the perturbed stable and unstable manifolds of the saddle point as a function of time τ along the orbit. If $\Delta(\tau)$ changes sign, then the manifolds intersect to $O(\epsilon^2)$ and there exists a homoclinic tangle.

For the Duffing equation (2.7), the homoclinic orbits are

$$x_o(t) = \pm\frac{2ae^{\sqrt{a}t}}{1 + abe^{2\sqrt{a}t}}, \tag{2.9}$$

from which the Melnikov function can be obtained as,

$$\Delta_D(\tau) = \sqrt{\frac{2}{b}}\,\pi\,\gamma\,\omega\ \ \mathrm{sech}\,\frac{\pi\,\omega}{2\sqrt{a}}\sin\omega\tau + \frac{4a^{3/2}}{3b}\delta. \tag{2.10}$$

Solving $\Delta_D(\tau) = 0$ for the first zero yields the Melnikov bound for chaos in equation (2.7),

$$\frac{\gamma}{\delta} \geq \frac{2\sqrt{2}a^{3/2}\cosh\frac{\pi\omega}{2\sqrt{a}}}{3\sqrt{b}\pi\omega}. \tag{2.11}$$

One would like to proceed analogously for equation (2.6); however, in general, finding $\Delta(\tau)$ explicitly is not tractable. The difficulty arises already with finding θ_0 explicitly. Normally, one would put $E = 0$ and solve for θ_0' using the first integral,

$$\frac{1}{2}(A(\theta,\lambda)\frac{d\theta}{dt})^2 + \int_0^\theta A(s,\lambda)C(s,\lambda)ds = E. \tag{2.12}$$

However, this integral has no known solution for the homoclinic orbit. Instead we turn to numerical evaluation.

2.4.1 Local analysis near $\lambda = 1$

For $0 < \lambda - 1 \ll 1$, the homoclinic orbits become local to the saddle point $(\theta, \dot{\theta}) = (0, 0)$. In this case, we expand expand (2.12) for $E = 0$ using Taylor expansions about $\theta = \theta_0 = 0$ and $\lambda = 1$ to approximate to order θ^6 the homoclinic orbit by

$$\frac{1}{2}\theta'(t)^2 + c_1\theta(t)^2 + c_2\theta(t)^4 + c_3\theta(t)^6 + O(\theta(t)^8) = 0 \tag{2.13}$$

where to order $(\lambda - 1)$,

$$c_1(\lambda) = -0.38(\lambda - 1) \tag{2.14}$$

$$c_2(\lambda) = 0.17 - 0.57(\lambda - 1) \tag{2.15}$$

$$c_3(\lambda) = 0.08 - 0.37(\lambda - 1). \tag{2.16}$$

For θ sufficiently small, we can neglect the c_3 term and (2.13) becomes the exact first integral for Duffing's equation, with the identification $a = c_1(\lambda), b = c_2(\lambda)$. Thus, for $(\lambda - 1) \ll 1$, we can approximate the first-integral using Duffing's equation, which yields (2.11) as the necessary condition for chaos.

What is meant by 'sufficiently small' can be estimated by comparing the maximum value of the $c_2\theta(t)^4$ term along the homoclinic orbit against the maximum of value of the $c_3\theta(t)^6$ term. We find that as λ increases, the $\theta(t)^6$ term quickly grows to be comparable to the $\theta(t)^4$ term. Indeed, we find that the Duffing approximation satisfies this consistency requirement for $\lambda - 1 < 0.01$, which is too small to be observed at the current scale of the experiment.

On the other hand, equation (2.13) to 6^{th} order is sufficient for the neglected terms to be an order of magnitude smaller than those retained for our experimental range, $\lambda - 1 < 0.55$. Using (2.13) as an approximation to the first integral of the homoclinic orbit, we extract the specific homoclinic orbit as

$$\theta_0(t) = \pm \frac{2c_1 e^{\sqrt{c_1}t}}{\sqrt{(1 + c_1 c_2 e^{2\sqrt{c_1}t})^2 + 4c_1^3 c_3 e^{4\sqrt{c_1}t}}}. \tag{2.17}$$

As expected, for $c_3 = 0$ we recover equation (2.9). Efforts to solve (2.8) with equation (2.17) have yet to be successful. On the other hand, numerical integration of (2.8) using (2.17) for fixed λ gives an approximate Melnikov curve in the parameter space $(\gamma/\delta, \omega)$. As we are interested in this parameter space, we fix λ at values relative to experiment and only expand in θ. This yields exact c_1, c_2, and c_3 values in (2.13). Example curves are given in figure 2.3.

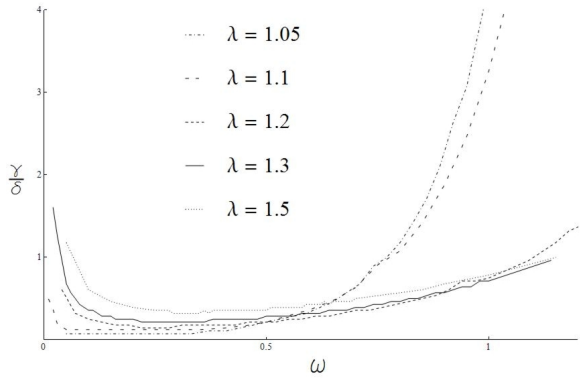

Figure 2.3: Melnikov Curves for various volumes λ, and $(\delta, \ell) = (3.73, 1.1)$. Above each curve chaotic oscillations are possible.

2.4.2 Numerical approximation of the seperatrix

For arbitrary $\lambda > 1$, we approximate the homoclinic orbit by numerically solving (2.2) for $\epsilon\delta = .65, \ell = .55$ with initial conditions near the saddle point. This solution is then used to numerically integrate (2.8) for a variety of τ values. Confidence in this numerical scheme is obtained by applying it to Duffing's equation and comparing the results to the known exact solution (2.11). A similar approach has been implemented elsewhere[31]. Sample curves for varying λ values are given in Figure 2.3. As λ increases, the parameter range where chaos is possible increases for high frequency but decreases for low amplitude forcings. Furthermore, the bound on chaos is sensitive to volume perturbations near $\lambda = 1$. For $1 < \lambda < 1.5$, this method yields nearly identical curves to the approximation obtained in Section 4.1.

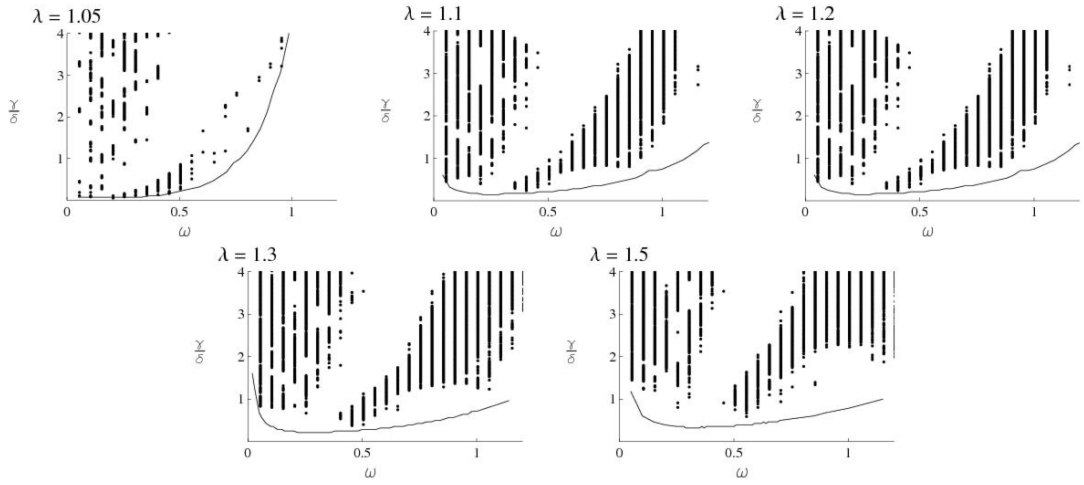

Figure 2.4: Lyapunov exponents for various values of λ computed on a rectangular grid in the parameter plane. Dots represent a positive Lyapunov exponent. Solid curves are the corresponding Melnikov bounds.

2.5 Lyapunov exponents approach

Lyapunov exponents measure the stretching of phase space and are computed numerically [35]. Consider two initial conditions, initially separated by a distance ϵ_o. Their separation grows on average as

$$\epsilon(t) = \epsilon_o e^{\nu t} \tag{2.18}$$

where ν is the largest Lyapunov exponent. For ν positive, solutions are exponentially separating and for ν negative, exponentially contracting. A positive Lyapunov exponent implies either chaotic behavior or escape to infinity (the latter case cannot occur in our system).

We rewrite (2.6) as $\dot{\mathbf{x}} = \mathbf{f}(\mathbf{x}, t)$ and numerically solve this equation and the first variational equation $\dot{\xi} = D\mathbf{f}(\theta_0(t), t)\xi$ simultaneously. The largest Lyapunov exponent is then approximated by

$$\nu = \frac{1}{t} \ln |\xi(\mathbf{t})| \tag{2.19}$$

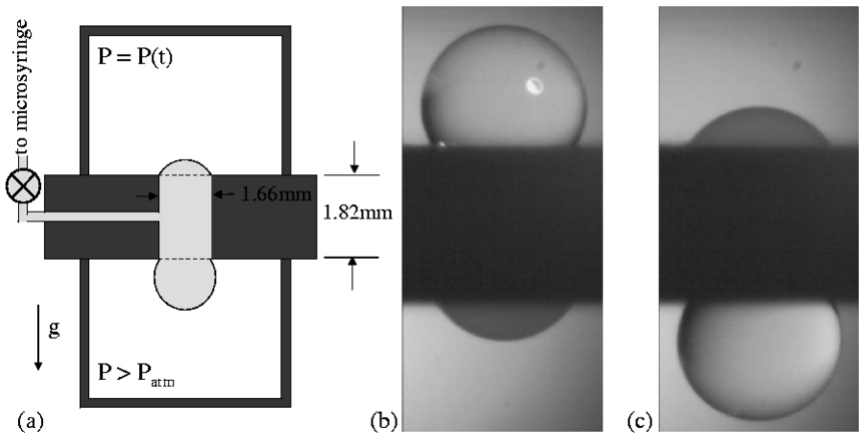

Figure 2.5: (a) Experimental setup for droplet system with applied sinusoidal pressure in upper chamber. (b), (c) Sample images depicting the asymmetric steady states for $\lambda > 1$ of the unforced system (Adapted from [1]).

for large t. Figure 2.4 shows grids of positive Lyapunov exponents for different λ values as well as the corresponding Melnikov curves. As expected, positive Lyapunov exponents occur only above the Melnikov curves. In each case, there is a band of periodic solutions, surrounded by predominantly chaotic behavior. Also, periodic behavior tends to prevail close to the Melnikov boundary. This is in contrast with the result for Duffing's equation, where two chaotic bands are surrounded by predominantly periodic dynamics [21].

2.6 Qualitative comparison with experiments

A loud-speaker is used to create pressure-driven oscillations in a system of two coupled water droplets. Images are recorded using a high-speed camera to capture the dynamics of the system. Image analysis with edge detection gives the droplet volumes, from which θ and λ are easily retrieved. For details of the experimental

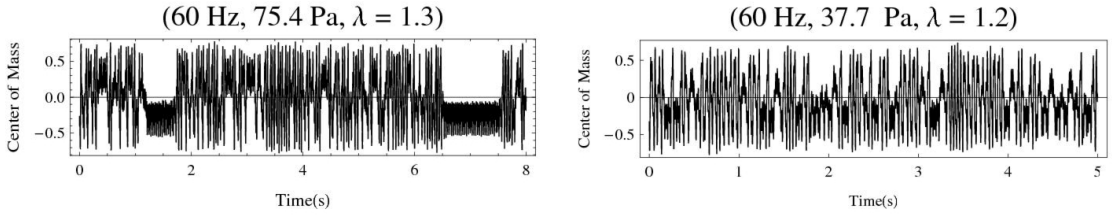

Figure 2.6: Selected experimental time series. The first shows intermittent chaotic oscillations, while the second shows a purely chaotic signal. These time series cooresponds to the sixth and seventh experiments listed in Table 1.

set-up, see [36].

Figure 2.6 shows sample time series for two chaotic experiments. Chaos is confirmed based on a time-series analysis using a standard tool [37]. Both Lyapunov exponents and correlation dimension indicate chaos. Periodic motions are also observed, as well as periodic non-axisymmetric precessing-like motions.

Quantitative comparison with experiments is complicated by a number of factors. First, there can be deviations from the assumptions of the model including non-spherical-cap shapes, non-axisymmetry, contact-lines which break from circular and, at large driving amplitudes, complete blow-out of the liquid. All these have been seen in experiment. The foremost complication, perhaps, occurs because of the inherent competition between the need for a lengthy time-series to confidently ascertain chaotic behavior and evaporation that diminishes the system volume continuously with time. The smaller the droplets, the greater effect the evaporation. Hence, in experiment, λ is slowly varying with time. Table 1 gives selected experimental observations where the selection is based on the extent to which λ measured at the beginning of a time series remains close to that measured at the end. Column 1 shows that the driving frequency has been varied by about a

Table 2.1: Experimental Data.

Forcing Frequency (Hz)	Forcing Amplitude (Pa)	γ/δ	ω	λ	Type of Motion
60	37.7	1.15	1.07	.9	Periodic
60	87.9	2.69	1.07	1.1	Periodic
60	82.8	2.54	1.07	1.1	Periodic
90	19.5	0.59	1.56	1.1	Periodic
45	12.4	0.38	0.82	1.2	Chaotic
60	37.7	1.15	1.07	1.2	Chaotic
60	75.4	2.30	1.07	1.3	Chaotic
42	13.5	0.36	0.41	1.5	Chaotic

factor of two, from 42 to 90 Hz. Column 2 indicates the corresponding forcing amplitudes, which vary by a factor of about 6. Column 3 gives the measured (average) total volume (scaled). Although it is difficult to prescribe λ beforehand in experiment, λ can be measured with reasonable accuracy. Note that the computations presented in the five panels of Figure 2.4 correspond closely to the five different λ reported in Table 1 for $\lambda > 1$. These data have not been plotted on Figure 2.4 since at most 2 points would appear on each panel. In summary, a quantitative test of the model is not reported in view of the limited range of experiments. A redesign of the experimental apparatus would be required to make such a test.

2.7 Discussion and Summary

A two-droplet oscillator operating under inviscid conditions is considered. Provided that droplet shapes are restricted to spherical-caps, the inviscid dynamics are described in the phase-plane by the behavior of a conservative oscillator. Total

volume of the droplet system is a parameter that tunes the depth and separation of the two energy wells. For small enough volume, there is a single well only while, for $\lambda > 1$, there are two stable states that yield bi-stable behavior. For $\lambda > 1$, dynamical trajectories about the stable states are limit cycles which, for increasing amplitude, have longer and longer periods. These limit cycles eventually coalesce to homoclinic orbits. For larger amplitudes yet, the dynamics is a single 'looping' orbit that encloses both stable states. For decreasing amplitudes, the looping orbits have increasing periods until they coalesce to the same homoclinic orbits.

In view of the similarity of the phase-plane of the un-forced droplet-droplet oscillator to the un-forced Duffing oscillator, one may anticipate that the droplet system, weakly-forced by a periodic pressure pulse of controlled amplitude and frequency and weakly-damped by viscosity, will exhibit chaos since the Duffing system does so under similar conditions. We report that, indeed, this is the case.

Although we are unable to establish a strict homotopy between orbits of the forced Duffing and droplet oscillators for all $\lambda > 1$, we can identify the two systems in the limit $\lambda \to 1$. That is, all the literature results for chaos in the forced Duffing, including the Melnikov bounds, apply for λ just super-critical.

For larger λ, we may expect a qualitative similarity between the systems to continue. Computational bounds using Melnikov's method shows that this is indeed the case. The calculation of Lyapunov exponents shows that chaotic trajectories actually do exist in the region where the Melnikov necessary condition is satisfied. On the other hand, the pattern of amplitudes and frequencies where the Lyapunov exponents give chaos (figure 4) is quite different from that for the Duffing, even for λ within 5% of critical. These qualitative differences are important, of course, if one would like to use the predictions as a guide to finding chaotic behavior in

the laboratory.

A number of approximations lead to the model whose dynamics are analyzed. Most prominent among these is that the droplet shapes are pieces of spheres. This condition is most favored for drops smaller than a few millimeters in size. Previous experiments have demonstrated that this condition is compatible with inviscid oscillations. The difficulty with identifying chaos is that long time series are required and mitigating against this is evaporation that is enhanced by the heat from lighting needed for quality images and the larger surface area to volume ratio of smaller droplets. The end effect is that the control parameter λ is a slowly-varying function of time which substantially complicates the interpretation of the observations relative to the prediction, at least from a quantitative viewpoint. Nevertheless, it can be concluded that chaos is observed in regions where the Melnikov theory predicts that it can occur and it is never observed where the theory predicts it cannot occur. Finally, the limited observations are consistent with the predictions of the Lyapunov exponent computations.

Acknowledgments

Theory and simulations are by DMS, writing by DMS and PHS, and experiments at RPI by CAL and AHH. We thank Dr. Mike Vogel for providing code to analyze images, and Dr. Eric Theisen for useful discussions. PHS thanks NSF DMI-0500311, CBET-0653831, and DARPA. AHH thanks NSF DMI-0500408.

CHAPTER 3

BIFURCATION AND STABILITY OF N COUPLED DROPLET OSCILLATORS WITH S_N SYMMETRY[1]

Abstract

Two inviscid coupled spherical-cap droplets oscillate. This paper considers a network of n spherical-cap droplet oscillators coupled via a central reservoir such that the system has S_n symmetry. Owing to a constant-volume constraint, the system reduces to a set of $n-1$ second-order differential equations. Surface tension (capillarity) resists deformations from the spherical shape. The symmetry of the system is important. In particular, independent of the equations, equilibrium solutions can be grouped into families, each with some p large and some $q = n - p$ small droplets. Within each family stability is invariant, which greatly reduces the number of cases to consider. Equilibrium curves and their stability are calculated analytically for an arbitrary number of droplets in a preferred coordinate space. For small volumes, the only equilibrium state is stable and corresponds to all identical droplets. For larger volumes, a multitude of equilibrium states exist, each having the property that all droplets have equal radius of curvature. Nearly all these equilibria are unstable, the only stable configuration being one droplet large and the rest small. Results of simulations for three droplets that show quasi-periodic and chaotic motions are also presented.

[1]D.M. Slater and P. H. Steen, *Bifurcation and Stability of n Coupled Droplet Oscillators with S_n Symmetry,* SIAM Journal of Applied Mathematics, To Appear (2011), Reprinted with permission.

3.1 Introduction

Coupled oscillators arise in a wide variety of scientific disciplines such as biology, electronics, and physics. Here the focus is on an S_n symmetric system where surface tension dominates other forces. Small-scale systems have grown in interest in recent years due to advances in nanotechnology and miniaturization. Viscous resistance can be negligible compared to inertia even at small scales[4], which we shall assume. The system studied is a network of n liquid droplets under a constant-volume constraint. In such systems, liquid droplets tend to spherical shapes under the action of capillarity. Droplet shapes are assumed to be spherical caps, making their center of mass motions one-dimensional. We consider the case where all the droplets exert the same force on all others, yielding a S_n symmetric model equivariant under reordering of droplets. Analytic stability and bifurcation results are obtained for a network of arbitrary size, including equilibrium branches, bifurcation points, and stability of equilibria.

The condition for mechanical equilibrium of a system of n coupled droplets is that they share a common pressure. From the volume-pressure response for a single droplet, Figure 3.1, each droplet can be in one of two equilibrium states, which we shall refer to as 'small' (sub-hemispherical) and 'large' (super-hemispherical), for convenience. Since pressure is inversely proportional to radius-of-curvature by the Young-Laplace condition, the n-system is in equilibrium when all droplets have the same radius-of-curvature. As droplets with heights h and $1/h$ have the same radius-of-curvature, the equilibrium states consists of some p droplets with height h and some q droplets with height $1/h$ and are $S_p \times S_q$ symmetric.

The stability of equilibria can be anticipated by physical arguments in many cases. Consider $n = 2$, for which there are four equilibrium states: large-large;

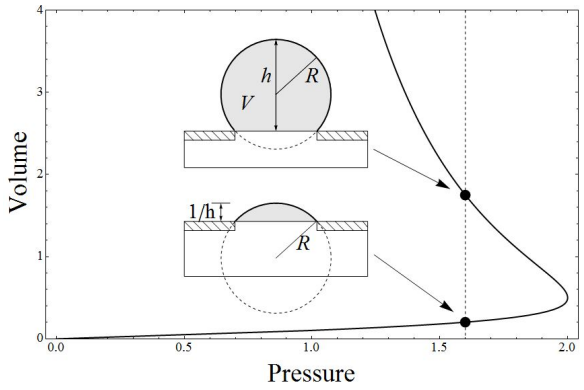

Figure 3.1: P-V diagram for a single droplet with volume scaled by $4/3\pi$. The two droplets shown share the same pressure and have heights h and $1/h$.

small-small; large-small; and small-large. Consider the large-large equilibrium state. If volume is added to one drop, making it slightly bigger, the radius increases and pressure decreases while, by conservation of volume, the same volume must be removed from the other making it slightly smaller, which increases its pressure. With the smaller drop having higher pressure, fluid will flow from smaller to bigger and the disturbance will amplify. Therefore, two coupled large drops are unstable. A similar "thought experiment" predicts that two small drops are stable. The large-small case is more subtle since the outcome depends on the different slopes of the response at the two volumes, but it can be seen similarly that the large-small state (and its twin, by symmetry) is always stable. Finally, for $p > 1$ large drops and $q = n - p$ small drops, large drops can be considered pairwise for which the above argument applies and we can conclude that these states have an unstable direction – they are saddle points.

Several comments are in order. The arguments of the previous paragraph did not depend on the type of underlying flow – viscous or inviscid. Indeed, they hold for both cases provided we interpret stability as 'Lyapunov stability' for inviscid

coupling and as 'asymptotic stability' for viscous flow (e.g. [5, 16]). In contrast, the conclusion of the previous paragraph depends crucially on the shape of the response curve. That is, if the droplet is replaced by an elastic membrane, the constitutive response changes, and the stability results are likely to change[38].

The study of capillary oscillations of droplets has its roots in the work of Lord Rayleigh. In 1879 he studied the vibrations of a sphere, where surface tension restores shape deviations due to liquid inertia [19]. More recently, equilibria of coupled droplets were studied by Wente in 1999 [39]. He examined the case of two and three droplets from a catastrophe theory point of view. His main results are universal unfoldings for the two droplet (cusp) and three droplet (elliptic umbilic) systems. He also proves, from an energy point of view, that any equilibrium with two or more large droplets must be unstable, recovered as a sub-case of this work. This work is an extension of a dynamical model for two coupled droplets[1] and reduces to their model for $n = 2$.

Motivation for this study comes from practical applications. Two pressure-coupled droplets have a double-well surface energy landscape. With a mechanism to trigger from one well to another, such as an electro-osmotic pump placed in the tube in between droplets [11], the system becomes an active 'switch'. Large systems can have multiple stable equilibria. For example, two droplets coupled through one liquid bridge can have up to five stable equilibria [40]. A number of applications exploit capillary bi-stability and active switch toggling between stable states. These include optical microlens devices [7, 8] and electronically-controlled adhesion devices [11, 2]. In this paper, we generalize to n-coupled droplets and study the phase-space dynamics of solutions to the inviscid governing equations.

The remainder of the paper is organized as follows. In Section 2 we discuss the

role symmetry plays in the problem with a particular emphasis on conclusions that can be made prior to precise formulation of the model in Section 3. In Sections 4 and 5 the cases of two and three droplets are analyzed. In section 6 analytic equilibria and stability results are obtained for the general case (arbitrarily many droplets). A discussion of the results and suggestions for further study can be found in Section 7.

3.2 Model-Independent Symmetry Results

We wish to model the dynamics of a S_n symmetric system of n coupled spherical-cap droplets. The assumption of S_n symmetry yields some basic information prior to formulating the problem precisely. As the droplets are spherical-caps we can describe a droplet's state with a single variable, e.g. height, volume or center-of-mass. Choosing volumes, suppose we can write the system as

$$\dot{x} = f(x; \lambda) \tag{3.1}$$

where $x = (\mathbf{V}, \dot{\mathbf{V}}) \in \mathbb{R}^{2(n-1)}$ is a vector of volumes and rates-of-change of volumes, $f : \mathbb{R}^{2(n-1)} \times \mathbb{R} \to \mathbb{R}^{2(n-1)}$ and λ is the total volume of the droplets. Since the total volume of the system is conserved only $n-1$ motions are independent.

S_n symmetry means $f(\gamma x, \lambda) = \gamma f(x, \lambda)$ for all $\gamma \in S_n$, $x \in \mathbb{R}^{2(n-1)}$. The advantage of symmetry is that if $f(\bar{x}, \lambda) = 0$, then $f(\gamma\bar{x}, \lambda) = \gamma f(\bar{x}, \lambda) = \gamma 0 = 0$. This implies that if $\bar{x}$ is an equilibrium solution, so are all members of its group orbit $S_n\bar{x} = \{\gamma\bar{x} : \gamma \in S_n\}$ [41]. Equivariance also implies that the identical solution must be an equilibrium state [41].

The Equivariant Branching Lemma provides a mechanism to find more equi-

librium states. It states that if a bifurcation from the identical state occurs, then for each axial subgroup Σ of S_n there exists a unique branch of solutions whose symmetry is Σ [41]. Axial subgroups are those with one-dimensional fixed point spaces. Since the total energy of the system must be conserved, it is easy to check that, up to conjugacy, the axial subgroups of S_n acting on our state space are $S_p \times S_q$ where $p + q = n$ and $1 \leq p \leq \lfloor n/2 \rfloor$. Each of these subgroups separate the droplets into two sets. Without loss of generality we assume the first and last droplet are in different sets. Thus, the first set consists of droplets each with volume V_1 and the second of droplets each with volume $V_n = (\lambda - pv)/q$. Defining

$$\theta \equiv V_1 - V_n, \tag{3.2}$$

a general two-dimensional bifurcation diagram can be constructed with the total volume λ as the bifurcation parameter.

Without explicitly formulating the dynamical system, symmetry alone implies that if a bifurcation occurs, $\lfloor n/2 \rfloor + 1$ types of equilibrium branches exist, each with a corresponding symmetry group $S_p \times S_q$. The group $S_p \times S_q$ has order $\binom{n}{q}$ so we expect a total of $\sum_{p=0}^{\lfloor n/2 \rfloor} \binom{n}{p}$ equilibrium branches. Furthermore, due to equivariance, stability must be invariant within each type of branch and one needs only calculate stability once for each family. Later we show that the equilibrium states can be easily separated by the number of small and large droplets. Symmetry does not rule out the existence of other equilibria, but, in our case, proof by inspection of the specific equations of motion will show that no others exist.

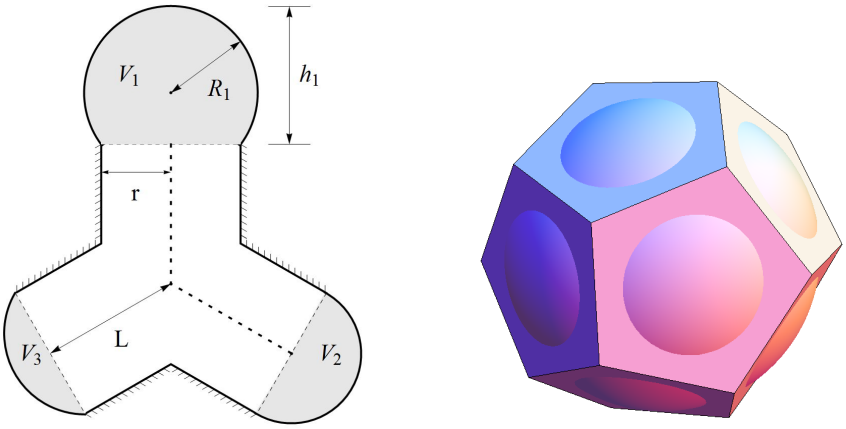

Figure 3.2: Left: A schematic of the three droplet system. Right: 12 droplets positioned on the sides of a dodecahedron

3.3 Oscillator-Model Formulation

Consider an object with n equally sized holes connected via tubes to a reservoir in the center (Fig 3.2). The holes are filled with liquid until droplets protrude. Assuming surface tension dominates other forces, the droplets may be assumed to be spherical caps, implying that each droplet's center-of-mass moves along a line. Let the total volume of the system be conserved, and let h_i be the height, V_i the volume, z_i the center of mass, L the tube centerline length, and R_i be the radius of curvature of droplet i. Volume conservation implies that $n-1$ of the droplets have independent motions.

Each droplet is a deformable region of fixed density ρ and variable volume V_i, whose linear momentum equation can be written down in terms of its center-of-mass z_i (e.g. [42] Section 5.15)

$$\rho \frac{d^2}{dt^2}\left[V_i z_i\right] + F_i^{(cap)} = F_i^{(sys)}, \quad \text{for } i = 1, \ldots, n \tag{3.3}$$

where $F_i^{(cap)}$ is the capillary force due to surface tension on droplet i and is evalu-

ated by the Young-Laplace relationship for a spherical shape

$$F_i^{(cap)} = 2\pi\sigma r^2(1/R_i). \tag{3.4}$$

The coupling term $F_i^{(sys)}$ acts like a reaction force and depends on all droplets in the system. As we assume S_n symmetry, each droplet affects all others in the same way and

$$F_i^{(sys)} = F_j^{(sys)} \equiv F^{(sys)}, \quad \forall \quad i, j. \tag{3.5}$$

For $n \leq 4$ this relationship can be derived based on the mechanics of a symmetric system of drops, while for $n \geq 5$ it is an assumption about the network. For example, in the case of three droplets the symmetry required corresponds to aligning the droplets at the vertices of an equilateral triangle (Figure 3.2). See appendix 3.9.1 for the 'mechanics' derivation of equation (3.3) and a discussion of the coupling term.

Subtracting equation (3.3) for the n^{th} droplet from each of the other equations, nondimensionalizing by rescaling volumes by $(4/3)\pi r^3$, lengths by r and time by $\rho r^3\sigma$ and rearranging yields

$$\frac{d^2}{dt^2}\left[V_i z_i - V_n z_n\right] = \frac{3}{2}\left[\frac{1}{R_n} - \frac{1}{R_i}\right], \qquad i = 1, 2, \ldots, n-1, \tag{3.6}$$

where

$$R_i = \frac{1}{2}\left(h_i + \frac{1}{h_i}\right), \tag{3.7}$$

$$z_i = \ell + h_i \frac{2 + h_i^2}{6 + 2h_i^2}, \tag{3.8}$$

$$V_i = \frac{1}{8} h_i (3 + h_i^2), \tag{3.9}$$

and the total volume is

$$\lambda \equiv \sum_{i=1}^{n} V_i. \tag{3.10}$$

Equations (3.7-3.9) follow from trigonometry, $\ell \equiv L/r$ is the scaled tube length and all other quantities are non-dimensional but use the same notation as previous dimensional quantities. Equation (3.10) allows us to write the properties of the n^{th} droplet as functions of the first $n-1$ droplets.

As outlined in Theisen et al.[1], a variety of coordinate systems can be chosen to characterize this system (volumes, heights, centers of mass, etc). Nonlinear invertible mappings exist between the coordinate representations allowing us to switch between representations freely. For example if we choose volumes, R_i, z_i and h_i can all be written as functions of V_i.

At equilibrium the droplets are organized into two sets, with droplets identical within each. Then θ as defined in equation (3.2) is the natural coordinate system for equilibrium calculations, as all equilibrium curves in each family collapse and a 2D bifurcation diagram is obtained with the total volume λ as the bifurcation parameter. In (θ, λ) space the identical solution is the null solution $\theta = 0$ and is an equilibrium state for all volumes (a typical assumption in bifurcation theory [20]). For stability calculations volumes are chosen as the dependent variables but calculations are often done using droplet heights, for convenience.

3.4 Two-Droplet Case

The model studied in this work is an extension of a model proposed by Theisen et. al[1] for two coupled spherical-cap droplets. It reduces to their model for $n = 2$. In that work, they find in the $(\theta, \lambda) = (V_1 - V_2, V_1 + V_2)$ coordinate system, a pitchfork bifurcation occurs at $\lambda = 1$, when the droplets are hemispherical. The zero solution (identical droplets) is stable for $\lambda < 1$ and unstable for $\lambda > 1$. The

symmetric pitchfork branch, on which one droplet is small and the other large is stable and parameterized as

$$\theta(\lambda) = \pm\left(\lambda^2 - \frac{3}{4}\lambda^{2/3} - \frac{1}{4}\right)^{1/2}. \tag{3.11}$$

By inspection (3.11) exists only for $\lambda \geq 1$. The stability of the branches is easily found by calculating the eigenvalues of the Jacobian. The fact that (3.11) is symmetric about the $\theta = 0$ axis results from the differential equation having $\mathbb{Z}_2$ symmetry in θ, which implies there must be a pitchfork bifurcation [43].

3.5 Three-Droplet Case

For three coupled spherical-cap droplets under a constant-volume constraint the governing equations are

$$\frac{d^2}{dt^2}\left[V_i z_i - V_3 z_3\right] = \frac{3}{2}\left[\frac{1}{R_3} - \frac{1}{R_i}\right], \qquad i = 1, 2. \tag{3.12}$$

It is easy to see that the system is at equilibrium if and only if $R_1 = R_2 = R_3$. Equal radii of curvature will also be the defining feature of equilibrium in the general case. Since R_i satisfies $R_i(h) = R_i(1/h)$, the system is in equilibrium if all the droplets have either the same height or the reciprocal of the height of the first droplet. In symmetry terms this means the equilibrium states consist of the group orbits of $h_1 = h_2 = h_3$ and $h_1 = h_2 = 1/h_3$. For clarity, the group orbit of the first case is the single given element, as its symmetry group is the trivial group $\mathbb{1}$, while the orbit of the second case has three elements since its symmetry group is $S_2 \times S_1$. For future reference, we will call a branch with all equal heights an *identical* branch and a branch with all but one droplet identical a *near-identical branch*. We will see in the case of n droplets these two types of branches have the only stable equilibria.

Let us consider a near-identical branch, characterized by the relationships $h_1 = h_2$ and $h_1 h_3 = 1$. Let $\theta = V_1 - V_3$. In order to obtain explicit stability of branches in this coordinate system, we let $(a, b) \equiv (h_1 + h_3, h_1 - h_3)$ and write

$$\theta = V_1 - V_3 = \frac{1}{32} b(12 + 3a^2 + b^2), \tag{3.13}$$

$$\lambda = V_1 + V_2 + V_3 = 2V_1 + V_3 = \frac{1}{64}(36a + 3a^3 + 12b + 3a^2 b + 9ab^2 + b^3). \tag{3.14}$$

Now $h_1 h_3 = 1$ implies $a^2 - b^2 = 4$. Using this identity, we simplify to

$$\theta = \frac{1}{8} b \left(6 + b^2\right), \tag{3.15}$$

$$\lambda = \frac{3}{16} a^3 + \frac{1}{16} b \left(6 + b^2\right). \tag{3.16}$$

Solving (3.15) for b and $a^2 - b^2 = 4$ for a yields

$$\lambda(\theta) = \frac{1}{2}\theta + \frac{3}{16} a^3 \tag{3.17}$$

as the equation of the equilibrium branch,where

$$a^3 = \left[4 + \left(\frac{-2^{2/3} + 2^{1/3}(2\theta + \sqrt{2 + 4\theta^2})^{2/3}}{(2\theta + \sqrt{2 + 4\theta^2})^{1/3}} \right)^2 \right]^{3/2}. \tag{3.18}$$

Setting $\theta = 0$ in (3.17) yields a transcritical bifurcation at $\lambda = 1.5$. This agrees with Wente's equilibrium analysis. Wente showed, using energy methods, that a bifurcation happens in the three droplet system when the three symmetric droplets reach a hemispherical state [39]. This occurs when the height of the droplet equals the radius of the droplet (scaled to one). Thus, at this point, $V_i = \frac{1}{8} * 1(3+1) = \frac{1}{2}$, which implies $\lambda = 3 * \frac{1}{2} = 1.5$. A saddle node bifurcation also occurs at $\lambda \approx 1.4355$, found by setting $\lambda(\theta) = 0$. The rational (exact) value of this turning point is found explicitly in the next section.

Equation (3.17) represents three branches in the full space, lying in the planes $V_1 = V_2$, $V_2 = V_3$, and $V_1 = V_3$ respectively. The equations in volume space can

be obtained by letting $\theta = V_1 - V_2, V_1 - V_3$, and $V_2 - V_3$ respectively. Figure 3.3 shows (3.17) along with the null solution plotted in the (θ, λ) plane as well as the linear frequencies found in the next section.

3.5.1 Stability of Equilibria for Three Droplets

To find the Lyapunov stability of the equilibrium solutions, we first expand out the derivatives in (3.6) using $\dot{V}_1 + \dot{V}_2 + \dot{V}_3 = 0$

$$\frac{2}{3}\left[\ddot{V}_1(h_1 + h_3 + 3\ell) + \ddot{V}_2\left(h_3 + \frac{3}{2}\ell\right) + \frac{dh_1}{dV_1}\dot{V}_1^2 - \frac{dh_3}{dV_3}(\dot{V}_1 + \dot{V}_2)^2\right] = \frac{3}{2}\left[\frac{1}{R_3} - \frac{1}{R_1}\right]. \tag{3.19}$$

For three droplets, there are two equations of this form and the system can be written as

$$\begin{pmatrix} h_1 + h_3 + 3\ell & h_3 + \frac{3}{2}\ell \\ h_3 + \frac{3}{2}\ell & h_2 + h_3 + 3\ell \end{pmatrix} \begin{pmatrix} \ddot{V}_1 \\ \ddot{V}_2 \end{pmatrix} = \begin{pmatrix} \frac{9}{4}\left[\frac{1}{R_3} - \frac{1}{R_1}\right] - \frac{dh_1}{dV_1}\dot{V}_1^2 + \frac{dh_3}{dV_3}(\dot{V}_1 + \dot{V}_2)^2 \\ \frac{9}{4}\left[\frac{1}{R_3} - \frac{1}{R_2}\right] - \frac{dh_2}{dV_2}\dot{V}_2^2 + \frac{dh_3}{dV_3}(\dot{V}_1 + \dot{V}_2)^2 \end{pmatrix}. \tag{3.20}$$

The inverse of the first matrix is easy to calculate and thus the model can be expressed as a system of four first-order differential equations.

First consider the identical case ($h_1 = h_2 = h_3 = h$), which corresponds to the zero solution in θ space. The Jacobian is

$$df = \begin{pmatrix} 0 & \mathbb{I}_2 \\ f(h)\mathbb{I}_2 & 0 \end{pmatrix}, \tag{3.21}$$

where

$$f(h) \equiv \frac{24(h^2 - 1)}{(2h + 3\ell)\,(1 + h^2)^3}. \tag{3.22}$$

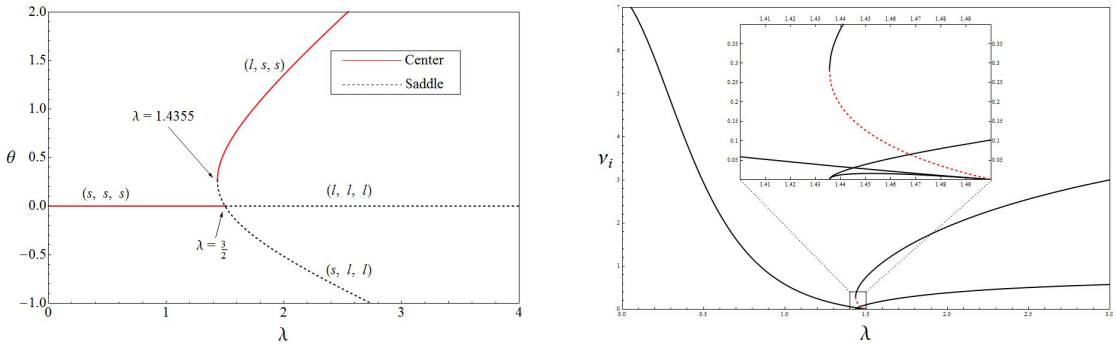

Figure 3.3: Left: Bifurcation diagram for three droplets in (θ, λ) space. A small drop is labeled s and a large drop is labeled l. The $\theta = 0$ solution is stable for $\lambda < 1.5$ and unstable for $\lambda > 1.5$. The saddle node branch is stable above the limit point and unstable below. Right: Non dimensional vibration frequencies. Solid lines indicate frequencies for stable equilibria, dotted lines unstable

Eigenvalues of df are easily computed to be $\nu_1 = \pm\sqrt{f(h)}$. $f(h)$ is negative for $h < 1$ and positive for $h > 1$ and thus the identical branch is a Lyapunov stable center for $h < 1$ ($\lambda < 1.5$) and a four-dimensional saddle for $h > 1$.

Next consider a near-identical branch ($h_1 = h_2 = h; h_3 = 1/h$), with Jacobian

$$df = \begin{pmatrix} 0 & 0 & 1 & 0 \\ 0 & 0 & 0 & 1 \\ \theta & \phi & 0 & 0 \\ \phi & \theta & 0 & 0 \end{pmatrix}, \tag{3.23}$$

where

$$\phi \equiv -f(h)\frac{h^4\xi - \xi - 1}{\xi + 2}, \quad \psi \equiv -f(h)\frac{1 + h^4\xi}{\xi + 2}, \quad \xi \equiv \frac{h(3\ell + 2h)}{2 + 3\ell h}. \tag{3.24}$$

The eigenvalues ν_2 and ν_3 are given by

$$\nu_2^2 = \phi - \psi = f(h), \tag{3.25}$$

$$\nu_3^2 = \phi + \psi = \frac{\xi}{\xi + 2}(1 - 2h^4)f(h). \tag{3.26}$$

This leads to the curves being stable for $h < 2^{-1/4}$and unstable for $h > 2^{-1/4}$. Note that when $h = 2^{-1/4}$, $\lambda = 1/2(2^{1/4} + 2^{3/4})$ gives the saddle-node bifurcation point. The other two curves in the group orbit share the same stability results. The computed eigenvalues also provide the linear frequencies of oscillation about the equilibrium states and are plotted in Figure 3.3.

3.6 Equilibria for n Droplets

Consider now the case of $n > 3$ droplets. As with the case $n = 3$, equilibrium states are characterized by equal radii-of-curvature. This allows one to classify equilibrium states by their symmetry group. Suppose the first p droplets have height h_1 and the last $q = n - p$ droplets have height $h_n = 1/h_1$. By symmetry, there are $\binom{n}{p} = n!/(p!q!)$ equilibrium curves of this type, one for each element of $S_p \times S_q$.

At equilibrium the droplets can be classified into two categories, within which the droplets are identical up to a permutation. Consequently, a natural coordinate system is the difference in volume between these two group θ, defined in equation (3.2). In this space, a single equilibrium curve is representative of all those with the same symmetry.

Suppose there are p droplets of type V_1 and q of type V_n. In this case $\theta = V_1 - V_n$ and $\lambda = pV_1 + qV_n$. To find the equilibrium curve in the (θ, λ) space let $(a, b) = (h_1 + h_n, h_1 - h_n)$ and note that $h_1 h_n = 1$ implies $a^2 - b^2 = 4$. $\theta(a, b)$ and $\lambda(a, b)$ simplify to

$$\theta = \frac{1}{8} b(6 + b^2), \tag{3.27}$$

$$\lambda = \frac{1}{16}(p+q)a^3 + \frac{1}{16}(p-q)b\left(6 + b^2\right). \tag{3.28}$$

Using (3.27) in (3.28), we obtain

$$\lambda = \frac{n}{16}a^3 + \frac{p-q}{2}\theta, \tag{3.29}$$

where a^3 is given by (3.18). When $\theta = 0$, all branches intersect the trivial branch at $\lambda = n/2$. This is precisely when all the drops are hemispherical, as expected, since each hemispherical drop has scaled volume $1/2$. Next, if n is even and $p = q$, $\lambda(\theta)$ is symmetric about the $\theta = 0$ axis. For this special case, similar calculations yield θ as a function of λ:

$$\theta(\lambda) = \pm\left(\frac{4}{n^2}\lambda^2 - \frac{3}{4}\left(\frac{2\lambda}{n}\right)^{2/3} - \frac{1}{4}\right)^{1/2},$$

which recovers (3.11) for $n = 2$.

In summary, the identical branch exists for all n. For n odd there are $(n-1)/2$ families of nontrivial asymmetric equilibrium branches, while for n even there are $(n-2)/2$ families of asymmetric and 1 family of symmetric nontrivial equilibrium branches. Figure 3.4 shows a generic bifurcation diagram in (θ, λ) space as well as linear frequencies for $n = 14$.

3.6.1 Stability of Equilibria for n droplets

To compute Lyapunov stability of the equilibrium curves for n coupled droplets one needs to first expand out derivatives and write the system in a form from

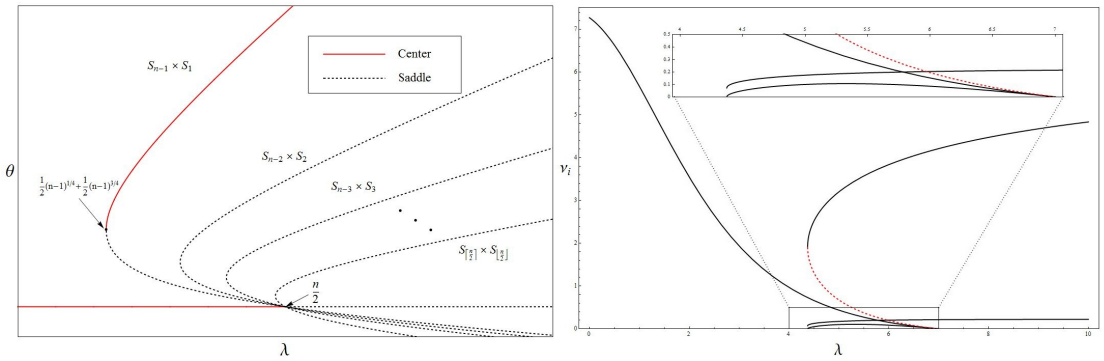

Figure 3.4: Left: Generic bifurcation diagrams. All curves intersect the $\theta = 0$ axis at $\lambda = n/2$ All nonzero branches are unstable except the left-most branch above the saddle node point. Right: Linear stability for the identical and near-identical branches for 14 droplets. Solid lines indicate stable solutions, dotted unstable.

which the Jacobian can be computed. Expanding out the derivatives in (3.6) for arbitrary n yields

$$\left[\ddot{V}_1(h_1 + h_n + 3\ell) + \sum_{i=2}^{n-1} \ddot{V}_i \left(h_n + \frac{3}{2}\ell\right)\right] = \frac{9}{4}\left(\frac{1}{R_n} - \frac{1}{R_1}\right) - \left[\frac{dh_i}{dV_i}\dot{V}_i^2 - \frac{dh_n}{dV_n}\left(\sum_{j=1}^{n-1} \dot{V}_j\right)^2\right]. \tag{3.30}$$

We can then write our system in matrix form as $A\ddot{\mathcal{V}} = \mathcal{G}$, where

$$(A)_{i,j} = \begin{cases} h_i + h_n + 3\ell & \text{if } i = j, \\ h_n + \frac{3}{2}\ell & \text{if } i \neq j, \end{cases} \tag{3.31}$$

$$\mathcal{G}_i = \frac{9}{4}\left(\frac{1}{R_n} - \frac{1}{R_1}\right) - \left[\frac{dh_i}{dV_i}\dot{V}_i^2 - \frac{dh_n}{dV_n}\left(\sum_{j=1}^{n} \dot{V}_j\right)^2\right], \tag{3.32}$$

$$\mathcal{V} = (V_1, V_2, \ldots, V_{n-1}). \tag{3.33}$$

Matrix A is clearly invertible ($h_i > 0$ is assumed) and we can write $\ddot{\mathcal{V}} = A^{-1}\mathcal{G}$. Since $\mathcal{G} = 0$ at equilibrium, the Jacobian is

$$\begin{pmatrix} 0 & \mathbb{I}_{n-1} \\ A^{-1}D\mathcal{G} & 0 \end{pmatrix}, \tag{3.34}$$

where

$$(D\mathcal{G})_{i,j} = \begin{cases} g(h_i) + g(h_n) & \text{if } i = j, \\ g(h_n) & \text{if } i \neq j, \end{cases} \tag{3.35}$$

and $g(h) = 12(h^2 - 1)/(1 + h^2)^3$. For clarity we break the stability analysis into three cases.

Case 1: Identical Branch

On the identical branch, all the droplets are of the same type. Let all drops have height h; then the Jacobian is

$$df = \begin{pmatrix} 0 & \mathbb{I}_{n-1} \\ f(h)\mathbb{I}_{n-1} & 0 \end{pmatrix}. \tag{3.36}$$

The eigenvalues of df are given by $\nu_1^2 = f(h)$, and thus the identical branch is a stable center when $h < 1$ ($\lambda < n/2$), and an n-dimensional saddle if $h > 1$ ($\lambda > n/2$). In other words, the branch is Lyapunov stable for small volumes and unstable for large volumes. Note that we use the notation as for $n = 3$ as the eigenvalues agree in this case.

Case 2: Near-Identical Branch

On the near-identical branches, all but one droplet are identical. Because of symmetry, without loss of generality we may assume the first $n - 1$ drops have height h and the last drop has height $1/h$. After computing A^{-1} (see appendix 3.9.2)

$A^{-1}D\mathcal{G}$ is given by

$$(\mathcal{D})_{i,j} = \left(A^{-1}D\mathcal{G}_{i,j}\right) = \begin{cases} \phi & \text{if } i = j, \\ \psi & \text{if } i \neq j, \end{cases} \tag{3.37}$$

$$\phi \equiv -f(h)\frac{h^4\xi - \xi - (n-2)}{\xi + (n-1)}, \tag{3.38}$$

$$\psi \equiv -f(h)\frac{1 + h^4\xi}{\xi + (n-1)}, \tag{3.39}$$

where ξ is given by (3.24). Matrix $\mathcal{D}$ is a circulant matrix, whose eigenvalues are found by evaluating $u(x) \equiv \phi + \psi(x + x^2 + x^3 + \ldots + x^{n-2})$ at the $(n-1)^{th}$ roots of unity [44]. The first root of unity is $x = 1$:

$$u(1) = \phi + (n-2)\psi. \tag{3.40}$$

For $x \neq 1$,

$$u(x) = \phi - \psi\left(\frac{x^n - x^2}{1 - x^2}\right), \tag{3.41}$$

from which it follows that

$$u(e^{\frac{k2\pi i}{n-1}}) = \phi - \psi\left(\frac{e^{n\frac{k2\pi in}{n-1}} - e^{2\frac{k2\pi i}{n-1}}}{e^{\frac{k2\pi i}{n-1}} - e^{2\frac{k2\pi i}{n-1}}}\right) = \phi - \psi \qquad (k = 1, \ldots, n-2), \tag{3.42}$$

since $e^{n\frac{k2\pi i}{n-1}} = e^{\frac{k2\pi i}{n-1}}$. Thus the eigenvalues of the Jacobian are given by

$$\nu_2^2 = \phi - \psi = f(h), \tag{3.43}$$

$$\nu_3^2 = \phi + (n-2)\psi = \frac{\xi}{\xi + (n-1)}\left(1 - (n-1)h^4\right) f(h). \tag{3.44}$$

Simple calculations show the near-identical branch is a stable center for $h < (n-1)^{-1/4}$ (one large drop) and a saddle for $h > (n-1)^{1/4}$ (one small drop). In terms of the total volume λ this change of stability corresponds to a saddle-node bifurcation at

$$\lambda = \frac{1}{2}\left((n-1)^{1/4} + (n-1)^{3/4}\right). \tag{3.45}$$

Note that, for $n = 3$, (3.45) recovers the value reported in section 5.1.

Case 3: All Other Branches $p > 0$, $q > 1$

Without loss of generality, suppose the first p droplets have height h and the last $q = n - p$ droplets height $1/h$. After computing A^{-1} and calculating $A^{-1}D\mathcal{G}$ (see appendix 3.9.2) the Jacobian for the general case is

$$df = \begin{pmatrix} 0 & \mathbb{I}_{n-1} \\ D \quad 0 & \\ & 0 \\ E \quad F & \end{pmatrix}_{n-1\times n-1}, \tag{3.46}$$

where

$$(D)_{i,j} = \begin{cases} \phi_{p,q} & \text{if } i = j, \\ \psi_{p,q} & \text{if } i \neq j, \end{cases}, \tag{3.47}$$

$$E \equiv \frac{1}{\left(\frac{1}{h} + \frac{3}{2}\ell\right)(p + q\xi)} \left(\xi g\left(\frac{1}{h}\right) - g(h)\right) \mathbb{1}_{q-1\times p}, \tag{3.48}$$

$$F \equiv \frac{g(\frac{1}{h})}{\frac{1}{h} + \frac{3}{2}\ell} \mathbb{I}_{q-1}, \tag{3.49}$$

$$\theta_{p,q} \equiv -f(h)\frac{h^4\xi - q\xi - p + 1}{p + q\xi}, \tag{3.50}$$

$$\phi_{p,q} \equiv -f(h)\frac{1 + h^4\xi}{p + q\xi} \tag{3.51}$$

By observation, the eigenvalues are simply plus and minus the eigenvalues of D and F. As F is a constant multiple of the identity and D is a circulant matrix, the eigenvalues of df are given by

$$\mu_1^2 = \frac{g(1/h)}{\frac{1}{h} + \frac{3}{2}\ell} = f\left(\frac{1}{h}\right), \tag{3.52}$$

$$\mu_2^2 = \theta_{p,q} - \phi_{p,q} = f(h), \tag{3.53}$$

$$\mu_3^2 = \theta_{p,q} + (p-1)\phi_{p,q} = \frac{\xi}{p + q\xi}\left(q - h^4 p\right) f(h). \tag{3.54}$$

As f changes sign when $h = 1$, it is easy to see that μ_1 is purely imaginary only if $h < 1$ while ν_2 is purely imaginary only if $h > 1$. Thus, as long as $p, q > 1$, both

D and F exist and there is *always* one unstable eigenvalue; hence *any equilibrium with two or more large drops must be unstable*. The calculated eigenvalues give the linear frequencies of vibration about the near-identical branches as well as the identical branch. For example, Figure 3.4 shows frequencies for $n = 14$.

Equation (3.46) is the Jacobian for all branches. The identical branch corresponds to $p = 0, q = n$. In this case the lower left block is just D and the eigenvalues are $f(1/h)$, which agrees with section 6.1.1 since the droplets labeled q have height $1/h$. For the near identical branches, $p = n - 1, q = 1.$ and the lower left block is just F. The eigenvalues are μ_2 and μ_3 which equal ν_2 and ν_3, calculated in section 6.1.2.

3.7 Discussion

A network of droplet oscillators with S_n symmetry subject to a constant-volume constraint is considered. Assuming the droplets are spherical-caps coupled through inviscid flow, the system behaves as a conservative oscillator. Using the total volume of the droplets as a parameter, families of equilibrium states and their stability are investigated with an emphasis on exploiting the symmetry of the system. In total, $\sum_{j=0}^{\lfloor n/2 \rfloor} \binom{n}{j}$ equilibrium branches are observed, all of which intersect transversely at $\lambda = n/2$. These are split into $\lfloor n/2 \rfloor + 1$ families, each with $S_p \times S_q$ symmetry, where there are p droplets with height h and q droplets with height $1/h$. All branches where both p and q are greater than 1 are always unstable. In other words, any equilibrium state with more than one large droplet is unstable. In contrast, the identical branch is stable for small volumes ($\lambda < n/2$) and unstable for large volumes ($\lambda > n/2$), while the near-identical branches are stable above

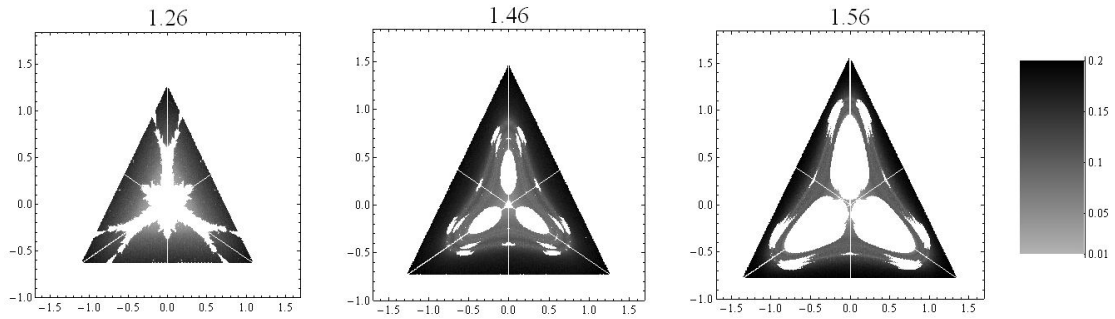

Figure 3.5: Grids of Lyapunov exponents, for $\ell = 1.1$ and $\lambda = 1.26, 1.46$, and 1.56 respectively. The darker the dot at each point the largest the Lyapunov exponent. White dots indicate quasiperiodic behavoir and gray dots indicate chaotic behavoir.

and unstable below their saddle-node bifurcations at (3.45).

In the case of two droplets the nature of trajectories is easily understood in the phase-plane as previously reported in [1]. There are three types of behavior: fixed points, periodic orbits and homoclinic orbits. For $\lambda < 1$ there is a single stable equilibrium point surrounded by a family of periodic orbits. For $\lambda > 1$ two families of the periodic orbits surround the stable states, and are separated from a family of looping periodic orbits by homoclinic orbits originating at the unstable equilibrium point. This is similar to the Duffing equation, a classic example in nonlinear dynamics. Furthermore, for λ near 1, truncated Taylor expansion about $\theta = 0$ of (3.6) yields the Duffing equation[45].

For $n \geq 3$, the nonlinear behavior of the system is more complex. Consider the case of three droplets where movement is confined to the plane. In this case, the phase space is four-dimensional and one expects complicated dynamics. Numerical exploration reveals two general forms of behavior: quasi-periodic behavior confined to a torus and chaotic phase-space-filling dynamics, with a rapid transition between the two.

To distinguish between a chaotic and a quasi-periodic solution one can calculate the largest Lyapunov exponent for a trajectory, with positive indicating chaotic behavior and a zero exponent quasi-periodic[46]. As the full phase space is four dimensional, displaying the whole space is not practical. Instead, we consider the slice of trajectories starting at rest ($\dot{V}_i(0) = 0$) with positive initial volumes for all droplets ($V_i(0) > 0$). Defining coordinates $\{x, y\} = \{\sqrt{3}/2(V_2 - V_3), V_1 - (1/2)(V_2 + V_3)\}$, this slice is triangular in shape and possesses S_3 symmetry, manifesting as reflections and rotations of an equilateral triangle. As such, we need consider only 1/6 of the space, generating the rest by group actions.

To compute the largest Lyapunov exponent, we employ the Wolf algorithm[35] as detailed by Rand[21]. Lyapunov exponents are calculated on a 0.007 sized grid, providing a graphical representation of where the different types of behavior occur. Sample grids for $\ell = 1.1$ and $\lambda = 1.26, 1.46$, and 1.56 are given in Figure 3.5. We take 0.01 to be our critical boundary for chaotic behavior, and plot all points with Lyapunov exponent greater than than 0.01 in gray-scale. Behavior is as might be anticipated. Prior to bifurcation, the only equilibrium is the stable center at the origin, which has a basin of quasi-periodicity represented by white pixels. Between bifurcations there are four stable centers, each with a basin of quasi-periodicity. Curiously, there are also other satellite regions of quasi-periodicity. Post bifurcation, the three stable centers each have a basin of quasi-periodicity. For λ near 1.5, these regions are small and as λ increases they grow in size. Again, there are also satellite regions of stability.

The bifurcation and stability results are highly dependent on the symmetry of the system, and thus we ask what happens if the symmetry of the system is broken. The model considered here has S_n symmetry because it was assumed

that the force felt by each droplet is the arithmetic average of force induced by the others. Suppose we perturb this average slightly so it is no longer perfectly symmetric. More precisely, suppose our symmetry assumption (3.5) is replaced by

$$F_i^{(sys)} \equiv \frac{1}{n-1} \sum_{j=1, j\neq i}^{n} (1+\epsilon_{i,j}) F_j^{(sys)}, \tag{3.55}$$

where $|\epsilon_{i,j}| \ll 1$. Golubitsky and Stewart[43] explain that under such perturbations, the equilibrium points will move and as such one does not expect transcritical bifurcations all at a single point. However the conclusion drawn from the analysis will not change under such perturbations. More generally, normal hyperbolicity guarantees that equilibria move continuously if the system is perturbed [43]. That is, there will still be equilibria with p large droplets and q small droplets, the difference being that droplets within the classes will no longer be identical and the stability of branches must be considered separately.

A natural area of further study is to consider external driving forces as well as small viscous resistance. The two-droplet system subject to sinusoidal forcing and small dampening is studied in [45], using Melnikov's method and Lyapunov exponents to explore the phase space for chaotic dynamics. In higher-order systems similar techniques as well as symmetry methods could be used. An exploration of the symmetries of chaotic attractors for the system may also be revealing.

3.8 Acknowledgements

PHS would like to thank Arnd Scheel for useful discussions. This research was supported in part by the Institute for Mathematics and its Applications with funds provided by the National Science Foundation and by NSF CBET-0653831 and NASA NNX09AI83G.

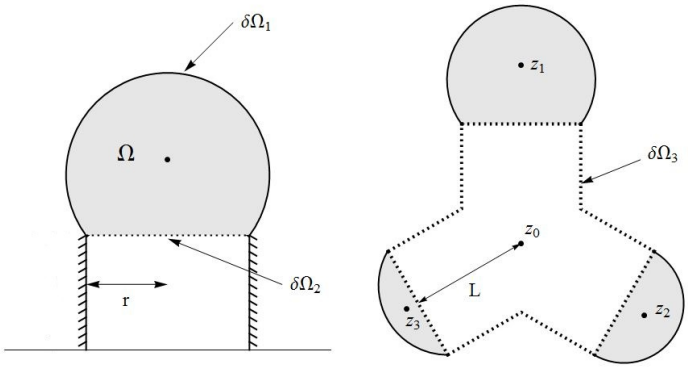

Figure 3.6: Left: Schematic of a single droplet connected to a tube. Right: Three droplet schematic

3.9 Appendix

3.9.1 Momentum Equation Derivation

Consider a spherical cap droplet Ω with boundary $\delta\Omega = \delta\Omega_1 \cup \delta\Omega_2$, where $\delta\Omega_1$ is acted on by surface tension and where across boundary $\delta\Omega_2$ fluid is free to flow owing to the tube it is connected to (Figure 3.6). The droplet control-volume has variable mass (volume). Assuming inviscid flow and an absence of body forces, the balance of linear momentum for droplet i can be written in terms of the pressure forces $f_i^{(p)}$ exerted as (e.g. [42] Section 5.15)

$$M_i \ddot{z}_i = f_i^{(p)} - \rho \int_S n \cdot (v - w)\,(v - \dot{z}_i)\,dS - \rho \frac{d}{dt} \int_S n \cdot (v - w)(c(s) - z_i) dS. \tag{3.56}$$

Here v is the velocity at which liquid leaves the control volume, w is the velocity of the interface and $c(s)$ is the surface coordinate of the boundary. As no fluid flows across $\delta\Omega_1$, $v = w$ there, while the liquid/liquid boundary $\delta\Omega_2$ does not move, so $w = 0$ there. Assuming a spatially uniform flow rate, constant density ρ and that

$\delta\Omega_2$ is connected to a tube with centerline length L to the origin, (3.56) takes the form

$$M_i\ddot{z}_i = f_i^{(p)} - \rho\int_{\delta\Omega_2} n\cdot v\,(v-\dot{z}_i) - \rho\frac{d}{dt}\int_{\delta\Omega_2} n\cdot v(c(s)-z_i)dS \tag{3.57}$$

$$= f_i^{(p)} + \dot{M}_i\left(\frac{\dot{M}_i}{\rho\pi r^2} - \dot{z}_i\right) + \frac{d}{dt}\left[\dot{M}_i\,(L-z_i)\right]. \tag{3.58}$$

Let $f_i^{(p)} = F_i^{(cap)} + f_i$ where the first term is the pressure drop over $\delta\Omega_1$ and the second over $\delta\Omega_2$. Simplifying (3.58) yields

$$\rho\frac{d^2}{dt^2}\left[V_i z_i\right] + F_i^{(cap)} = f_i + \frac{\rho}{\pi r^2}\dot{V}_i^2 + L\rho\ddot{V}_i \equiv F_i^{(sys)} \tag{3.59}$$

which is equation (3.3). The right-hand-side $F_i^{(sys)}$ is the coupling term which includes both pressure force and rate of change of fluid momentum. Computing the center-of-mass equations for the tubes allows us to derive relationships between the $F_i^{(sys)}$ terms. In order for the system to be S_n symmetric, the tubes must be in an $n-1$ dimensional space with the droplets at the vertexes of a $(n-1)$-simplex (for $n \leq 4$ this is realizable in physical space of dimension $d = n-1$, while for $n > 4$ it is a network assumption). Take, for example, the case of three droplets positioned at the vertexes of a right triangle (Figure 3.6). Treating the tubes as a control volume with boundary $\delta\Omega_3$ lying in the plane, we apply (3.56) in vector form to obtain

$$\vec{0} = F_1^{(sys)}\vec{a}_1 + F_2^{(sys)}\vec{a}_2 + F_3^{(sys)}\vec{a}_3 \tag{3.60}$$

where $\vec{a}_1 = (1,0)$, $\vec{a}_2 = (-1,\sqrt{3})/2$ and $\vec{a}_3 = (-1,\sqrt{3})/2$. The rest of the terms are zero because $z_0(t) = 0$ for all time. Equation (3.60) implies that $F_1^{(sys)} = F_2^{(sys)}$ and $F_1^{(sys)} = F_3^{(sys)}$ and hence they must all be equal.

3.9.2 Jacobian for n Droplets

To compute the Jacobian for an arbitrary number of drops we need the inverse of $A_{n\times n}$. Without loss of generality assume the first p drops have height h the other $q = n - p$ drops have height $1/h$. Then

$$A = \left(\frac{1}{h} + \frac{3}{2}\ell\right)\begin{pmatrix} y\mathbb{I}_p + \mathbb{1}_{p\times p} & \mathbb{1}_{p\times q-1} \\ \mathbb{1}_{q-1\times p} & \mathbb{I}_{q-1} + \mathbb{1}_{q-1\times q-1} \end{pmatrix} \tag{3.61}$$

whose inverse is

$$A^{-1} = \frac{1}{(\frac{1}{h} + \frac{3}{2}\ell)(p + q\xi)}\begin{pmatrix} M_{p\times p} & -\mathbb{1}_{p\times q-1} \\ -\mathbb{1}_{q-1\times p} & N_{q-1\times q-1} \end{pmatrix}, \tag{3.62}$$

where

$$M \equiv (\frac{p}{\xi} + q)\mathbb{I}_{p\times p} - \frac{1}{\xi}\mathbb{1}_{p\times p}, \tag{3.63}$$

$$N \equiv (p + q\xi)\mathbb{I}_{p\times p} - \xi\mathbb{1}_{p\times p}. \tag{3.64}$$

Note that on the near-identical branch, $p = n - 1$, $q = 1$ and A^{-1} is just

$$\frac{2h}{(2 + 3h\ell)(\xi + n - 1)}M_{n-1\times n-1}. \tag{3.65}$$

Next, we compute the Jacobian of the right hand side $\mathcal{DG}$

$$\mathcal{DG} = \begin{pmatrix} G_1 & g(1/h)\mathbb{1}_{p\times q-1} \\ g(1/h)\mathbb{1}_{q-1}\times p & G_2 \end{pmatrix}, \tag{3.66}$$

$$G_1 \equiv g(h)\mathbb{I}_{p\times p} + g(1/h)\mathbb{1}_{p\times p}, \tag{3.67}$$

$$G_2 \equiv g(1/h)(\mathbb{I}_{p\times p} + \mathbb{1}_{p\times p}). \tag{3.68}$$

Putting it together, now,

$$A^{-1}\mathcal{DG} = \frac{1}{p + qh^2}\begin{pmatrix} M_{p\times p} & -\mathbb{1}_{p\times q-1} \\ -\mathbb{1}_{q-1\times p} & N_{q-1\times q-1} \end{pmatrix}, \begin{pmatrix} G_1 & g(1/h)\mathbb{1}_{p\times q-1} \\ g(1/h)\mathbb{1}_{q-1\times p} & G_2 \end{pmatrix}, \tag{3.69}$$

which when multiplied out yields the lower left-hand block of (3.46).

CHAPTER 4

DETECTING SYMMETRY IN THE MOTIONS OF THREE COUPLED DROPLET OSCILLATORS

Abstract

Symmetry detectives offer an automated method to classify the symmetries of solutions to dynamical systems. In this paper, symmetry detectives are applied to conservative motions of coupled-droplet oscillators. Previous application of detectives has been for the determination of symmetries of attractors as well as the detection of symmetry-changing bifurcations. We analyze the trajectories of a fourth-order S_3 symmetric model of three coupled liquid droplets, where motions are assumed frictionless. Since there is no dissipation in the model, there are no asymptotically stable attractors, only centers. Solutions away from equilibrium are the focus. In particular, we examine trajectories starting with no initial velocity. Detection of symmetry is achieved by mapping a trajectory into an appropriate representation space and where distances to fixed-point subspaces of subgroups are computed. Results of the symmetry-detective approach are contrasted to the more conventional computation of the largest Lyapunov exponent as a signal of chaotic or quasi-periodic dynamics. Both methods can be applied to a grid of initial conditions in an automated fashion. Our results demonstrate a strong correlation between symmetries and nonlinear dynamics.

4.1 Introduction

Symmetry is often an important structural component of dynamical systems. For example, changes in symmetry often coincide with drastic changes in dynamics.

For a dynamical system that is Γ-equivariant, individual trajectories have their own symmetries which are typically subgroups of Γ. Determining how the symmetries of the trajectories of three S_3 coupled droplets change as the initial conditions vary is the goal of this work.

When surface tension dominates other forces, liquid droplets tend to spherical shapes. We consider a network of three such droplets, constrained to circular contact-lines and coupled via a central chamber such that the system is S_3 symmetric. Slater and Steen[47] derived a frictionless model of center-of-mass motions for n droplets, extending a two droplet model[1]. Here, we restrict to the case of three droplets in which the phase space is four dimensional and chaotic and quasi-periodic dynamics occur. Furthermore, we assume frictionless motions, which implies there are no Lyapunov stable solutions. As such, there are no classical attracting sets to analyze. Instead, we focus on chaotic and quasi-periodic trajectories away from equilibrium.

We utilize two metrics to classify solutions. First, the largest Lyapunov exponent is used to distinguish between quasi-periodic and chaotic dynamics. Second, symmetry detectives are used to classify the set-wise symmetries of trajectories. Both these methods are employed on grids of initial conditions with fixed total volumes. We find that chaotic trajectories have S_3 symmetry, while quasi-periodic trajectories have one of the three flip symmetries.

The method of symmetry detectives was introduced by Barany et al.[48] in 1993. The general idea is to map a trajectory to a point in an appropriate representation space where determining symmetry reduces to calculating distances to fixed point subspaces. The typical application of detectives is the determination of how the symmetries of attractors change as parameters are varied [49] [50]. They also have

been applied to experimentally-determined attractors[51, 52]. In contrast, we are interested in the symmetries of trajectories rather those of attractors.

The paper is setup as follows. First the model is introduced and the equilibria, their stability and the bifurcation diagram are discussed. Then Lyapunov exponents are calculated on grids of initial conditions, separating trajectories into regions of quasi-periodicity and regions of chaotic dynamics. After that, an introduction to the method of detectives is given and the particular detective employed and its corresponding representation space are discussed. The method of detectives is then used on a grid of initial conditions and the results are compared with the Lyapunov exponents calculated. Complications of the method due to small oscillations are discussed and a solution is given.

4.2 Oscillator Model

The motion of a deformable liquid mass depends on the nature of the liquid (Newtonian or non-Newtonian), the geometry of constraint, boundary conditions and the driving force, in general. Under all circumstances, the center-of-mass (c-o-m) is governed by Newton's laws. When the surface tension is sufficiently strong a droplet pinned on a circular contact-line will tend to retain its spherical shape and deform as a spherical cap. Spherical-cap deformations comprise a one-parameter family, an important class of deformations. Suppose three droplets, connected via a central chamber, have co-planar symmetry axes such that the angle between each is $2\pi/3$ (Figure 4.1). Restricting to spherical caps, it is clear that the c-o-m of each droplet moves along its axis and that the three-droplet system com moves in the plane. Let $\mathbf{Z} \in \mathbb{R}^2$ be the center-of-mass of the system and V_T be the total

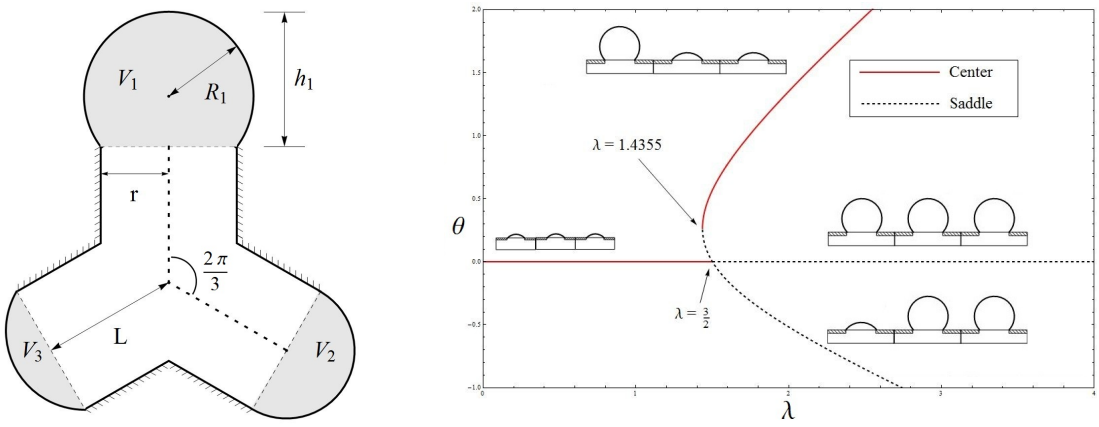

Figure 4.1: (Left) Schematic of the S_3 symmetric three droplet system. (Right) Bifurcation diagram for the three droplet system where $\theta = V_i - V_j$ for some i and j while $\lambda = V_1 + V_2 + V_3$. The zero branch (all identical) is stable for $\lambda < 1.5$ and unstable for $\lambda > 1.5$. The saddle-node branch (two identical) is stable above the limit point and unstable below.

volume. Then Newton's second law is

$$\rho \frac{d^2}{dt^2} (V_T \mathbf{Z}) = \mathbf{F}. \tag{4.1}$$

where the net force acting $\mathbf{F}$ is the net pressure force arising from surface tension σ through the radius of curvature R_i of each droplet i, as given by the Young-Laplace law. The driving force felt at the base of each drop is $2\pi r^2 \sigma / R_i$, and the net force on the c-o-m of each drop consists of the driving force and a resisting force due to the other two drops. For the symmetric arrangement shown in Figure 4.1, each drop experiences an identical resisting force which can be eliminated by pair-wise subtraction of Newton's law applied to each drop. Details are provided in [47] where the model for S_n symmetric coupled spherical-cap droplets, $n > 2$ is derived.

Using the standard basis in $\mathbb{R}^2$ and nondimensionalizing by rescaling volumes

by $(4/3)\pi r^3$, lengths by r and time by $\rho r^3 \sigma$, (4.1) may be written as

$$\frac{d^2}{dt^2}\left[V_2 z_2 - V_3 z_3\right] = \frac{3}{2}\left[\frac{1}{R_3} - \frac{1}{R_2}\right] \tag{4.2}$$

$$\frac{d^2}{dt^2}\left[V_1 z_1 - \frac{1}{2}\left(V_2 z_2 + V_3 z_3\right)\right] = \frac{3}{4}\left[\frac{1}{R_2} + \frac{1}{R_3} - \frac{2}{R_1}\right]. \tag{4.3}$$

Here, $R_i \equiv (1/2)(h_i + 1/h_i)$, $z_i = (\ell + h_i(2 + h_i^2)(6 + 2h_i^2)$, ℓ is the scaled tube length, and h_i is given implicitly by $V_i = (h_i/8)(3 + h_i^2)$. Let λ be the total volume of the three droplets defined as

$$\lambda = V_1 + V_2 + V_3. \tag{4.4}$$

Since λ is constant, one of the volumes in (4.2)-(4.3) may be replaced by λ. If V_3 is replaced a well defined dynamical system is obtained with independent variables V_1 and V_2 and parameters λ and ℓ.

The system is in equilibrium when all three droplets have the same radius of curvature. As $R(h) = R(1/h)$, this occurs when all the droplets have height h or two have height h and the third $1/h$. The second case can happen in three different ways, each with a different pair of droplets identical. Let $\theta = V_i - V_j$ be the difference in volume between droplets i and j. Then a 2D bifurcation diagram in (θ, λ) is obtained in Figure 4.1. The identical case (h, h, h) is a stable center for $\lambda < 1.5$ and an unstable saddle for $\lambda > 1.5$. This change in stability happens when all three droplets are hemispherical. The saddle-node branch represents three branches in the full space and corresponds to any two droplets having height h and the third height $1/h$ $(h, h, 1/h)$. This branch consists of stable centers when one droplet is sufficiently large and unstable saddle points otherwise.

We are interested in the symmetries of trajectories of this S_3 equivariant dynamical system. The system has no dissipation which implies all stable equilibrium points are centers. Furthermore, solutions lie in $\mathbb{R}^4$ and hence can be quasi-periodic

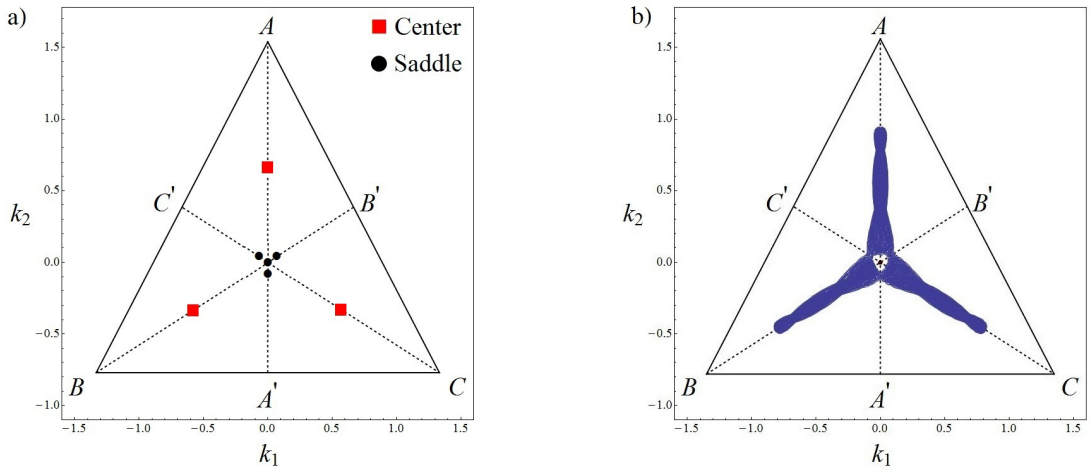

Figure 4.2: (a) Equilibrium points and lines of symmetry for $\lambda = 1.54$ and $\ell = 1.1$. Red squares are centers and black circles are saddle-points. (b) A fully symmetric chaotic trajectory projected into (k_1, k_2) space. The solution is symmetric with respect to reflections about the three lines of symmetry AA', BB' and CC' as well as rotations that map the lines to each other. The plotted triangle bounds points where all three droplets have positive volume.

or chaotic. As the phase space is four dimensional, quantification of it in its entirety is not tractable. Instead we restrict to initial conditions with zero initial velocity and positive initial volumes. We explore how the symmetries and dynamics change as the initial conditions are varied.

For visual inspection, trajectories are projected onto $\mathbb{R}^2$ using the coordinates

$$k_1 = \frac{\sqrt{3}}{2}(V_2 - V_3) \tag{4.5}$$

$$k_2 = V_1 - \frac{1}{2}(V_2 + V_3)\,. \tag{4.6}$$

In this space, the S_3 symmetry of the system manifests as the symmetries of a right triangle. A sample plot of a fully symmetric chaotic trajectory is shown in Figure 4.2b. As a set, this solution is symmetric with respect to reflections along the lines AA', BB' and CC' and rotations that map these lines to each other.

The triangular boundary is the set of points with positive volume. The nature of solutions starting in this triangular are explored as the total volume of the system changes. Symmetry detectives allow us to explore such initial conditions in an automated fashion. The question to answer is then:

Starting from rest, what sorts of trajectories do we expected? What symmetries do they have and are they chaotic or quasi-periodic?

4.2.1 Lyapunov Exponents

Let

$$\dot{\mathbf{x}} = \mathbf{f}(\mathbf{x}, t) \tag{4.7}$$

be our equations of motion. The question of chaotic or quasi-periodic is answered through the calculation of the largest Lyapunov exponent. Lyapunov exponents measure the stretching of phase space and can be computed numerically [35]. Let $\bar{x}_1$ and $\bar{x}_2$ be two solutions of equation (4.7) such that $|\bar{x}_1(0) - \bar{x}_2(0)| = \delta_0 \ll 1$. On average, they will separate with speed

$$\epsilon(t) = \delta_0 e^{\nu t}, \tag{4.8}$$

where ν is the largest Lyapunov exponent. If ν is positive the solutions are separating with exponential speed, a hallmark of chaotic behavior. For quasi-periodic dynamics ν will be zero; hence, the largest Lyapunov exponent can be used to distinguish between chaotic and quasi-periodic dynamics [46].

To calculate ν we use the Wolff algorithm as described in [21]. Solving equation

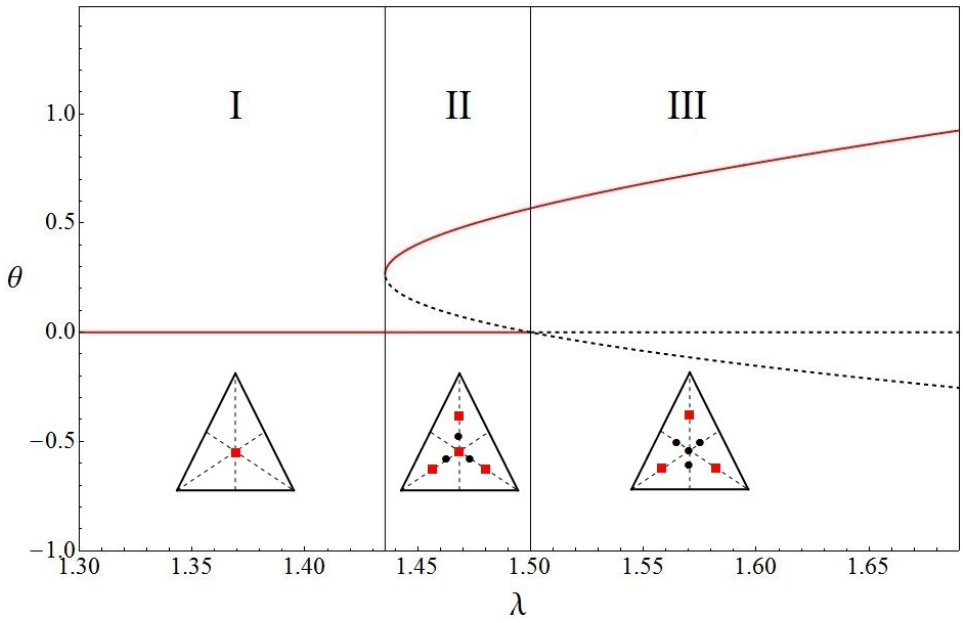

Figure 4.3: Bifurcation Diagram showing the three regions of parameter space. Sketches of equilibrium positions in (k_1, k_2) space are also shown with red squares indicating centers and black circles saddle points.

(4.7) and the first variational equation $\dot{\xi} = (D\mathbf{f})[\mathbf{x}(t), t)]\xi$ simultaneously yields

$$\nu = \lim_{T\to\infty} \frac{1}{T} \ln |\xi(T)| \tag{4.9}$$

as the largest Lyapunov exponent.

As the system has S_3 symmetry solving for 1/6 of the initial conditions is sufficient, as behavior of the rest may be generated by group actions[47]. There are three distinct regions of parameter space as depicted in Figure 4.3. In region I there is only one equilibrium point and it is a fully symmetric stable center. In region II, there are four stable centers and three saddle points, while for region III the fully symmetric equilibrium point has lost its stability and there are four saddles and three centers. All equilibrium points lie on one of the three symmetry manifolds (AA', BB' and CC' in Figure 4.2a) where at least two of the droplets are identical.

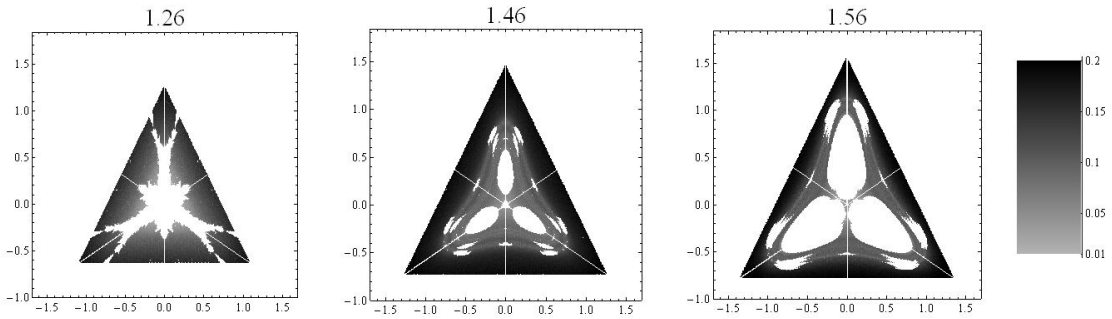

Figure 4.4: Grids of Lyapunov exponents for $\ell = 1.1$ and $\lambda = 1.26, 1.46$ and 1.56 for trajectories with positive initial volumes (bounding triangle) and zero initial velocity. The darker the dot the larger the Lyapunov exponent. White dots indicate quasi-periodic dynamics while gray dots indicate chaotic dynamics.

Lyapunov exponents calculated on a 0.007 spaced triangular grid for $T = 8000$ and $\ell = 1.1$ are shown in Figure 4.4. In these three plots, white indicates quasi-periodic dynamics ($\nu < 0.01$) while gray points are chaotic ($\nu > 0.01$). In region I, the fully symmetric equilibrium point has a basin of quasi-periodicity, indicated by white points on the graph. As λ increases, this region shrinks until it disappears at $\lambda = 1.5$. In region II, all four stable equilibrium have basins of quasi-periodicity, while in region III the fully symmetric equilibrium point has gone unstable and we are left with three stable centers each with its own basin of quasi-periodicity. Curiously, as λ varies, satellite regions of quasi-periodicity appear and disappear. Understanding these satellite regions is a driving force for the exploration of symmetries using detectives.

4.3 Symmetry Detectives

Symmetry detectives were introduced in 1993 by Barany et al. [48]. Here we give a brief introduction, roughly following Kroon and Stewart [49], to define the needed terminology and state the necessary results. The idea is to take a trajectory and map it into an appropriate representation space where determining symmetry requires computation of distances to fixed point subspaces of subgroups.

Let Γ be a finite group and let $f : \mathbb{R}^n \to \mathbb{R}^n$ be Γ equivariant. In other words, for each $\gamma \in \Gamma$, $f(\gamma x) = \gamma f(x)$. Let $\bar{x}(t)$ be some solution to $\dot{x} = f(x)$ and define $A = \{\bar{x}(t) \; \forall \; t > 0\}$. We are interested in the setwise symmetries of A. That is, A is γ symmetric if $\gamma A = A$ (in contrast pointwise symmetry requires $x(\gamma t) = x(t) \; \forall \; t$).

Definition 1 *An **observable** is a C^∞ Γ equivariant mapping $\phi : \mathbb{R}^n \to W$ where W is some (finite-dimensional) representation space of Γ. For an open set $A \subset \mathbb{R}^n$, an **observation** is*

$$K_\phi(A) = \int_A \phi d\mu \tag{4.10}$$

where μ is Lebesgue measure.

Suppose A is an open bounded subset of $\mathbb{R}^n$ which satisfies $\gamma A = A$ or $\gamma A \cap A = \emptyset$. Then it has been proven that there exists a representation W of Γ and an observation $\phi : \mathbb{R}^n \to W$ such that $\gamma K_\phi(A) = K_\phi(A)$ if and only if $\gamma A = A$. Such an observation ϕ is called a ***detective***. Note that $K_\phi(A)$ is a vector in a finite dimensional representation space, and thus it is γ symmetric if lies in the fixed point subspace of γ.

An appropriate representative space must distinguish all subgroups of Γ. Recall the fixed point subspace of $\Sigma \in \Gamma$ is $\mathrm{Fix}(\Sigma) \equiv \{x \in \mathbb{R}^n : \sigma x = x \quad \forall \sigma \in \Sigma\}$.

Definition 2 *A representation space distinguishes all subgroups of* Γ *if for all subgroups* Δ, Σ *such that* $\Delta \subset \Sigma \subset \Gamma$ *and* $\Delta \neq \Sigma$,

$$dim\ Fix_W(\Delta) > dim\ Fix_W(\Sigma).$$

Once we have a detective and an appropriate representation space calculating the symmetries is mostly routine. We need just enumerate the subgroups of Γ and calculate the distance from the observation of A to the fixed point subspace of each. If this distance is small we say that A has that symmetry.

There is an issue we have glossed over so far. As discussed in [49], if a trajectory $\bar{x}(t)$ is chaotic it requires an infinite amount of information to describe A exactly. Furthermore, A need not be an open set. This is typically dealt with in one of two ways. The first is to thicken A to an open set B by covering it with a finite number of open balls of radius ϵ. If the balls are sufficiently small the symmetry is unchanged. Unfortunately, the distance calculated depends on ϵ, adding a parameter to the method. The second method is to use the ergodic sum

$$K_\phi^E(A) = \lim_{N\to\infty} \frac{1}{N} \int_0^N \phi(x(t))dt. \tag{4.11}$$

When calculating the symmetries of an attractor, the dependence of (4.11) on $x(0)$ can be problematic. It turns out that that this is not an issue for this work as we are interested in the symmetries of trajectories rather than attractors. We choose to use the ergodic sum approach as it removes the need to specify a ball size ϵ and can be nicely adapted to numerical solutions.

4.3.1 A S_3 Detective and the Left Regular Representation

We adapt an observable proven to be a detective by Tchistiakov [50]. This detective maps into the *left regular representation* $R_{S_3} \cong \mathbb{R}^6$ of S_3 consisting of all real-valued functions on S_3. The left regular representation distinguishes all subgroups for any finite group. The action of $\gamma \in S_3$ on $\sigma \in R_{S_3}$ is induced by multiplication with the inverse on the left

$$(\gamma \circ \sigma)(\delta) = \sigma(\gamma^{-1}\delta) \quad \forall \delta \in V_{S_3}. \tag{4.12}$$

Theorem 4.3.1 *Let* $\phi : \mathbb{R}^3 \to V_{S_3}$ *be*

$$\phi(x) = \left(x_1x_2^2, x_2x_1^2, x_3x_2^2, x_1x_3^2, x_3x_1^2, x_2x_3^2\right). \tag{4.13}$$

Then ϕ *is a detective for* S_3.

For the coupled droplet system $x \equiv \{V_1, V_2, V_3\}$. Clearly if a solution is symmetric with respect to volumes it must also be symmetric with respect to velocities. Tchistiakov proved a more general form of a detective for S_n, a result we now state here for completeness. Let $p : \mathbb{R}^n \to \mathbb{R}$ be the polynomial mapping $p(x_1, \ldots, x_n) = x_1x_2^2 \cdots x_{n-1}^{n-1}$.

Theorem 4.3.2 *Let* R_{S_n} *be the left regular representation of* S_n *and let* $\psi : \mathbb{R}^n \to R_{S_n}$ *be*

$$\psi(x)[\gamma] \equiv p(\gamma^{-1}x).$$

Then ψ *is a detective for* S_n.

For S_3 symmetry, $p(x) = x_1x_2^2$ and

$$\psi(x) = \{(e)^{-1}, (12)^{-1}, (13)^{-1}, (23)^{-1}, (123)^{-1}, (132)^{-1}\}x_1x_2^2 \tag{4.14}$$

$$= \left(x_1x_2^2, x_2x_1^2, x_3x_2^2, x_1x_3^2, x_3x_1^2, x_2x_3^2\right) = \phi(x). \tag{4.15}$$

In order to compute the distances to the fixed point subspaces of each subgroup of S_3 the matrix representations of the group actions on R_{S_3} are needed. As an example, consider the flip (12) action. Ordering the elements as in the detective, the action of (12) can be written as

$$(12)^{-1}\{e \quad (12) \quad (13) \quad (23) \quad (123) \quad (132)\} \tag{4.16}$$

$$= \{(12) \quad e \quad (123) \quad (132) \quad (13) \quad (23)\}, \tag{4.17}$$

which corresponds to the 6×6 matrix

$$P_{(12)} = \begin{pmatrix} 0 & 1 & 0 & 0 & 0 & 0 \\ 1 & 0 & 0 & 0 & 0 & 0 \\ 0 & 0 & 0 & 0 & 1 & 0 \\ 0 & 0 & 0 & 0 & 0 & 1 \\ 0 & 0 & 1 & 0 & 0 & 0 \\ 0 & 0 & 0 & 1 & 0 & 0 \end{pmatrix}. \tag{4.18}$$

The eigenvectors of $P_{(12)}$ are $v_1 = \{1, 1, 0, 0, 0, 0\}, v_2 = \{0, 0, 0, 1, 0, 1\}$, and $v_3 = \{0, 0, 1, 0, 1, 0\}$. To determine if a vector $x \in R_{S_3} \cong \mathbb{R}^6$ is (12) symmetric, compute the distance from x to the subspaces spanned by v_1, v_2, and v_3

$$D_{(12)}(x) = \sqrt{(x_1 - x_2)^2 + (x_3 - x_5)^2 + (x_4 - x_6)^2}. \tag{4.19}$$

Similar calculations for the other three subspaces yield the distances to the other fixed point subspaces

$$D_{13}(x) = \sqrt{(x_1 - x_3)^2 + (x_2 - x_6)^2 + (y_4 - y_5)^2} \tag{4.20}$$

$$D_{23}(x) = \sqrt{(x_1 - x_4)^2 + (x_3 - x_6)^2 + (y_2 - y_5)^2} \tag{4.21}$$

$$D_{rot}(x) = \sqrt{\frac{2}{3}\left[\left(\sum_{j=1}^{6} x_j^2\right) - (x_2x_3 + x_2x_4 + x_5x_6 + x_1x_5 + x_1x_6)\right]}. \tag{4.22}$$

To summarize, in order to calculate the symmetries of a trajectory $\bar{x}(t)$, one first computes the observation of $\phi(\bar{x}(t))$ using the ergodic sum to obtain a point $y = K_\phi^E(\bar{x}(t))$ in the representation space. Then one calculates the distance from y to the fixed point subspace of each subgroup. If this distance is close to zero the solution has the symmetry. The final question is how to determine when a small number is 'close enough' to zero. A method for determining this is given in the next section.

4.3.2 Numerical Results

To compute the symmetries of trajectories equations (4.2) and (4.3) are rewritten as a system of four first order equations and solved numerically with a variable step size solver. This yields a numerical solution $\{\mathbf{V}_i, \dot{\mathbf{V}}_i\} \in \mathbb{R}^6$ with variable step size Δt_i for $0 \leq t \leq T$. The ergodic sum is then approximated using a Riemann sum

$$K_\phi^E(V(0)) = \frac{1}{T}\sum_{j=1}^{T} \phi(\mathbf{V}_j)\Delta t_j \tag{4.23}$$

The typical approach is to slowly vary a parameter and look for jumps in the distance functions. An example of this is shown in Figure 4.5, where analogously

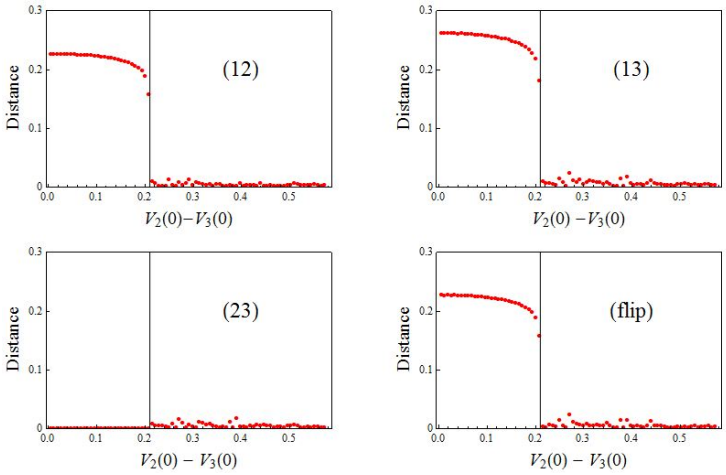

Figure 4.5: Distances to the four subgroups of S_3 for solutions starting with no initial velocity, $\lambda = 1.56$, and $V_1(0) = 0.891$. The distances for $(12), (13)$ and the flip jump from nonzero to near zero at $V_2(0) - V_3(0) = 0.21$. This indicates solutions with $V_2(0) - V_3(0) < 0.21$ are (23) symmetric while those with $V_2(0) - V_3(0) > 0.21$ are S_3 symmetric.

the initial conditions are slowly varied. In this plot, $\lambda = 1.56$, $V_1(0) = 0.891$, and the difference between $V_2(0)$ and $V_3(0)$ is varied from 0 to 0.672. To insure convergence of the ergodic sum we solve for T = 8000, which corresponds to between 20,000 and 100,000 steps depending on the nature of the trajectory. For $V_2(0) - V_3(0) < 0.21$, D_{23} is small compared to the other distances, implying trajectories are (23) symmetry. In contrast, for $V_2(0) - V_3(0) > 0.21$ all distances are small implying trajectories are S_3 symmetric.

Next we consider a grid of initial conditions with zero initial velocity and positive initial volumes for each droplet. On this grid solutions exhibit a variety of behaviors. For most points, calculating the ergodic sum as (4.23) works well. However, a difficulty arises for small oscillations near the fully symmetric equilibrium point. For $\lambda < 1.5$ this equilibrium point is a center and solutions starting near it stay near it for all time. This is a problem as we will now show.

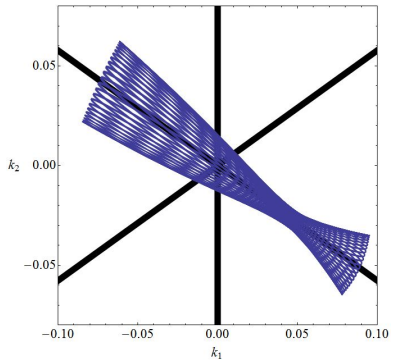

Figure 4.6: A small oscillation about the fully symmetric equilibrium point ($k_1 = k_2 = 0$) for which all the distances are small relative to other trajectories.

Let $\bar{x}(t) = (\bar{x}_1, \bar{x}_2, \bar{x}_3)$ be a trajectory and let $\epsilon_1(t) = \bar{x_1} - \bar{x_2}$ and $\epsilon_2(t) = \bar{x_1} - \bar{x_3}$. Then $\bar{x}(t)$ may be written in terms of $\epsilon_1(t)$, $\epsilon_2(t)$ and λ as

$$\bar{x}(t) = (\alpha(t), \alpha(t) + \epsilon_1(t), \alpha(t) + \epsilon_2(t)) \tag{4.24}$$

where $\alpha(t) = (1/3)(\lambda - \epsilon_1(t) - \epsilon_2(t))$. Let

$$\epsilon = \max_{t \in (0,T)} \left(|\bar{x}_1 - \bar{x}_2|, |\bar{x}_2 - \bar{x}_3|, |\bar{x}_1 - \bar{x}_3| \right) \tag{4.25}$$

be the maximum difference in volume of the three droplets. Now suppose $\epsilon \ll 1$ and λ is $O(1)$. Noting that $|\epsilon_1(t) + \epsilon_2(t)| < \epsilon$, the distance $D_{12}(\phi(\bar{x}(t))$ satisfies

$$D_{12}(\phi(\bar{x}(t))) = \sqrt{\frac{1}{2} \left(\bar{x}_1 - \bar{x}_2\right)^2 \left(\bar{x}_1^2 \bar{x}_2^2 + (\bar{x}_1 + \bar{x}_2)^2 \bar{x}_3^2 + \bar{x}_3^4\right)} \tag{4.26}$$

$$< \sqrt{\frac{1}{2} \epsilon^2 O(\alpha(t)^4)} = O(\epsilon \lambda^4) = O(\epsilon) \tag{4.27}$$

since λ is order 1. This is a problem, for regardless of the behavior of the trajectory the calculated distance for the flip (12) turns out to be small (similar calculations show the same behavior for the other subgroups).

For example if $\lambda = 1.3, V_1(0) = 0.4$, and $V_2(0) = 0.5$ the maximal difference in volumes over the trajectory is 0.11 and the four distances are given in row 2 of table

Symmetry	(12)	(13)	(23)	(flip)
Distance **without** scaling	3.77×10^{-3}	3.23×10^{-5}	3.74×10^{-3}	4.34×10^{-3}
Distance **with** scaling	3.455	0.030	3.426	3.973

Table 4.1: Distances for each subgroup for a small oscillation about the fully symmetric equilibrium point with and without applying the scaling map $s(x)$. After scaling, only the (13) distance is small, correctly indicating the trajectory is (13) symmetric

4.1. These distances are all small compared to those of other trajectories. Figure 4.6 shows the trajectory which is clearly only (13) symmetric. Closer examination of the distances reveals the method has detected the (13) distance to be two orders of magnitude smaller than the others,

The issue with small oscillations is readily fixed by introducing a scaling map $s(x)$, applied prior to calculating the observation. We choose to scale so that the maximal difference in volume over the trajectory ϵ is unity

$$s(x) \equiv x/\epsilon. \tag{4.28}$$

This scaling map $s(x)$ is S_3 symmetric and will not change the symmetries of trajectories. Calculating the observation of $s(x(t))$ instead of $x(t)$ normalizes the dependence on the maximal differences in volumes of a trajectory. For the trajectory, above the distances after scaling are given on the third row of table 4.1. They now correctly identify the trajectory as (13) symmetric.

Most solutions on our grid have O(1) distances, so the scaling has little effect. The scaling map also allows us to recognize small oscillations that possess no symmetry. Note, a naive solution would have been to scale four distances by the largest distance, to determine which distance is orders of magnitude smaller. This would fail to distinguish between trajectories with no symmetry and those with

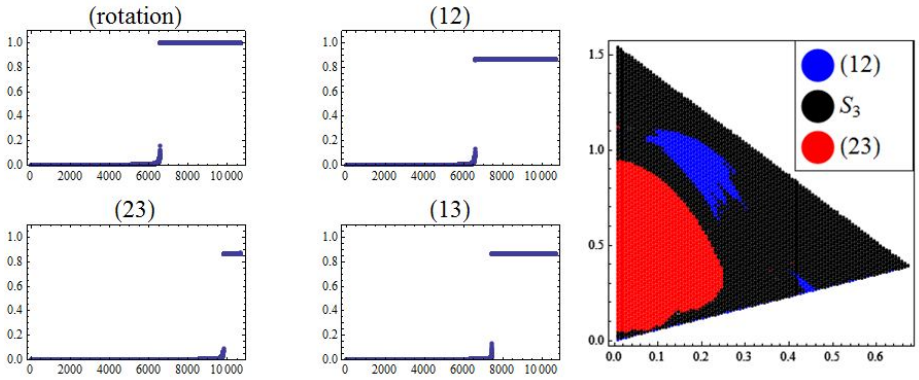

Figure 4.7: (Left) Scaled distances for a 0.007 grid of initial conditions with zero initial velocity and positive initial volume for 1/6 of the triangular phase-space. Each plot is sorted from shortest to longest distance to illustrate the jump from near zero to nonzero. Near zero distances indicate that trajectory had that symmetry. (Right) The grid of initial conditions plotted with their calculated symmetries.

full symmetry, an important difference as shown in the next section.

4.3.3 Symmetry Calculations

Symmetry detectives are employed for initial conditions on a 0.007 sized grid and the equations are solved for $0 \leq t \leq T = 8000$. For each point four distances are calculated, corresponding to the three flip and the rotational symmetry subgroups. There are three possibilities: one of the four distances is small, all are small, or none are small. To determine symmetry, the following process is applied to each point. If any single distance is two orders of magnitude smaller than the rest, normalize all four by the largest distance. This brings the three nonzero distances to near 1 and leaves the other small, resulting in a nice dichotomy between the nonzero and zero distances for points with a flip or rotational symmetry. If all four distances are within two orders of magnitude the values are left alone. These points either

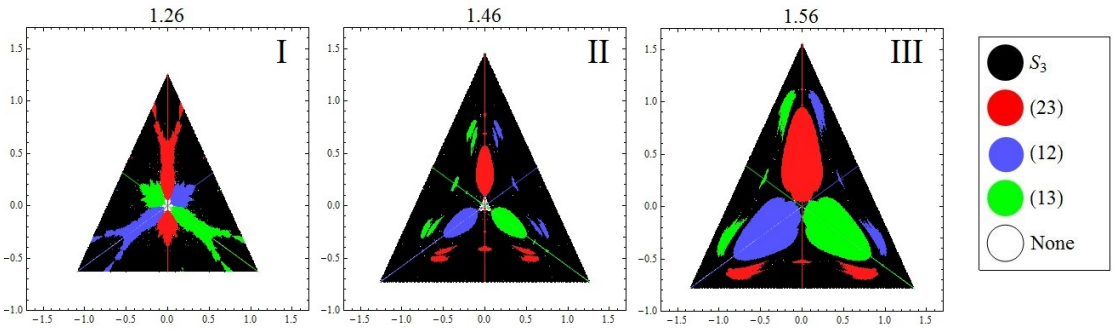

Figure 4.8: Grids of symmetries for $\ell = 1.1$ and $\lambda = 1.26, 1.46$, and 1.56 calculated using the symmetry detective method. Each color represents a different symmetry. In each case, between 30,000 and 40,000 initial conditions are displayed.

posses full symmetry or no symmetry. For example sorted distances for $\lambda = 1.56$ are given in figure 4.7. There are a few points that are mildly ambiguous with distances between .1 and .2, but this corresponds to roughly five points out of 100,000. For each plot, the distances have been sorted from smallest to largest to show the clear jump between small and non-zero. The symmetries of the various initial conditions are also shown in Figure 4.7, where we use a cutoff of 0.1 for having a particular symmetry. For this section of parameter space there are no points with (13) symmetry.

As noted above, regions I, II, and III are distinguished by different behaviors there are three different areas of parameter space. Figure 4.8 shows sample triangular sets for each region, corresponding to $\lambda = 1.26, 1.46$, and 1.56 respectively. In each plot between 30,000 and 40,000 initial conditions are displayed, First, note the similarities between Figures 4.4 and 4.8. Fully symmetric trajectories are chaotic, while those with flip symmetries are quasi-periodic. This correspondence carries over for all λ values calculated ($1 \leq \lambda \leq 1.7$). Furthermore, the satellite regions of quasi-periodicity have different symmetries than their adjacent larger basins of

quasi-periodicity.

In the first two plots there is a small region near the fully symmetric equilibrium point where the method has detected no symmetry. Small oscillations about this stable equilibrium point are in fact quasi-periodic with two frequencies; however, as the initial conditions approach the equilibrium point, one of the frequencies goes to infinity. This means, as we move towards the equilibrium point, that we need to solve for longer and longer time to detect the symmetry of these points. An example is shown in Figure 4.9, where $\lambda = 1.3$, $V_1(0) = 0.45, V_2(0) = .42$. Two plots are shown, one for $T = 8000$ and the other for $T = 150,000$. For this trajectory, the slow frequency is 150,000 time units, well beyond our stopping time of $T = 8000$. Figure 4.9 also shows the convergence of the four distances which is even slower.

As λ varies a multitude of arrangements of symmetries are observed. Sample plots are shown in Figure 4.11. In each case, Lyapunov exponents have also been calculated, with the correspondence that all with flip symmetries are quasi-periodic and all with S_3 symmetry are chaotic. As noted previously, for sufficiently small small oscillations no determination can be made because of the solving time issue just discussed. Such points are labeled white in the plots. Furthermore, the symmetries of satellite regions do not change as λ varies. More specifically, regardless of the size and shape of the satellite region, its symmetry depends only on which third of the triangle it lies in. In terms of initial volumes, a satellite region is symmetric with respect to whichever two initial volumes are the largest.

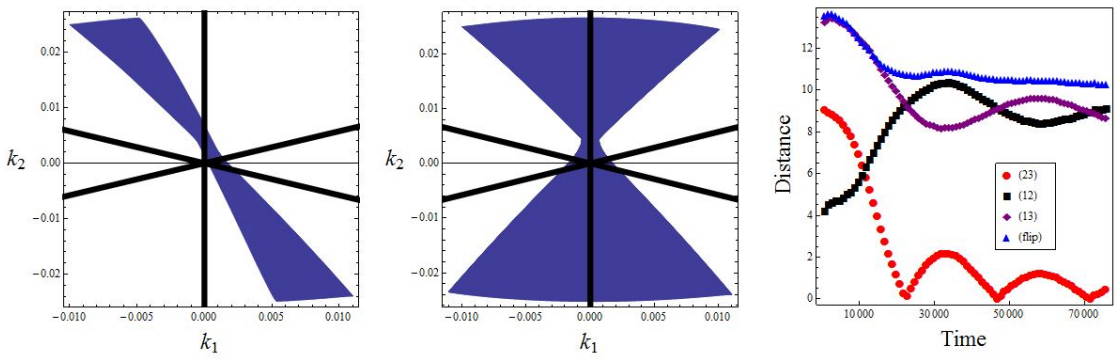

Figure 4.9: (Left): Trajectory for $\lambda = 1.3$, $(V_1(0), V_2(0)) = (.45, .42)$ for T = 8000 showing that the trajectory has not finished one pass through its complete trajectory and currently has no symmetry. (Middle) The same trajectory for T = 150000, showing it has finished a pass through its trajectory and is (23) symmetric. (Right) Convergence of the four distances for the trajectory. The solution is (23) symmetric, but the distance converges very slowly.

4.3.4 Concluding Remarks

The use of symmetry detectives allows for automated determination of symmetries of solutions of differential equations. Here we have used a detective to obtain a second metric to classifying trajectories of a system of three symmetric coupled droplets. We find that, for this system, chaotic solutions have S_3 symmetry while quasi-periodic and periodic solutions have one of the three flip symmetries. Furthermore, the satellite regions seen in the Lyapunov exponent plots posses different symmetries than the large basins. In these satellite regions the two large droplets exchange places, while in the larger basins two small droplets exchange. Figure 4.10a shows a trajectory from the large red basin in Figure 4.8III where droplet one stays large and droplets two and three oscillate symmetrically. Figure 4.10b is from one of the smaller blue regions and shows droplets one and two becoming large and droplet three staying small.

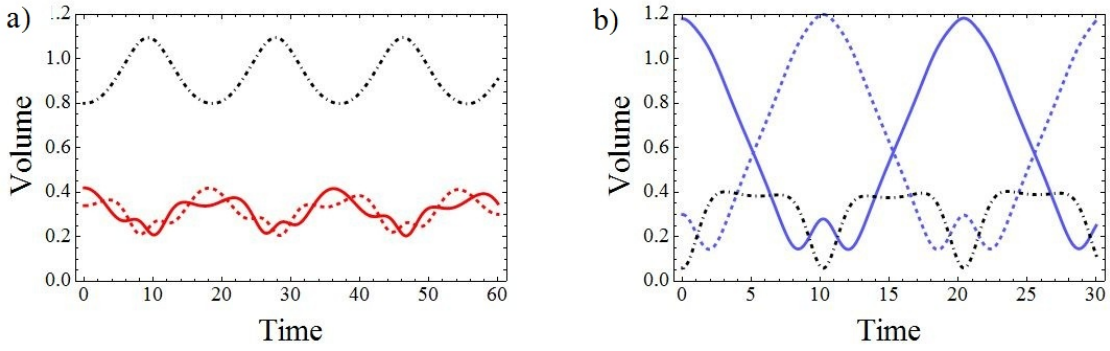

Figure 4.10: Quasi-periodic Trajectories for $\lambda = 1.56$. (a) An initial condition in the large red basin where droplet 1 stays large and droplets 2 and 3 switch back and forth. (b) An initial condition in the blue satellite region where droplet 3 stays small and droplets 1 and 2 oscillate back and forth.

The symmetry detective method presented here can be applied to most any other symmetric dynamical system. All finite subgroups of $O(n)$ have a left regular representation and it always distinguishes all subgroups. This means if Γ is a finite group, the detective we employ may be used for any Γ-equivariant dynamical system. Calculating symmetries is also fast compared to Lyapunov exponents as it only requires numerically solving the model equations, whereas Lyapunov exponents involves simultaneously solving the first variational equation. It is also well known that when computing Lyapunov exponents that solutions to the variational equations grow exponentially and have overflow issues[21]. Our intent is to illustrate the utility of symmetry attractors and their usefulness in a nonattractor setting.

4.3.5 Acknowledgments

This work was supported by NSF CBET-0653831 and NASA NNX09AI83G.

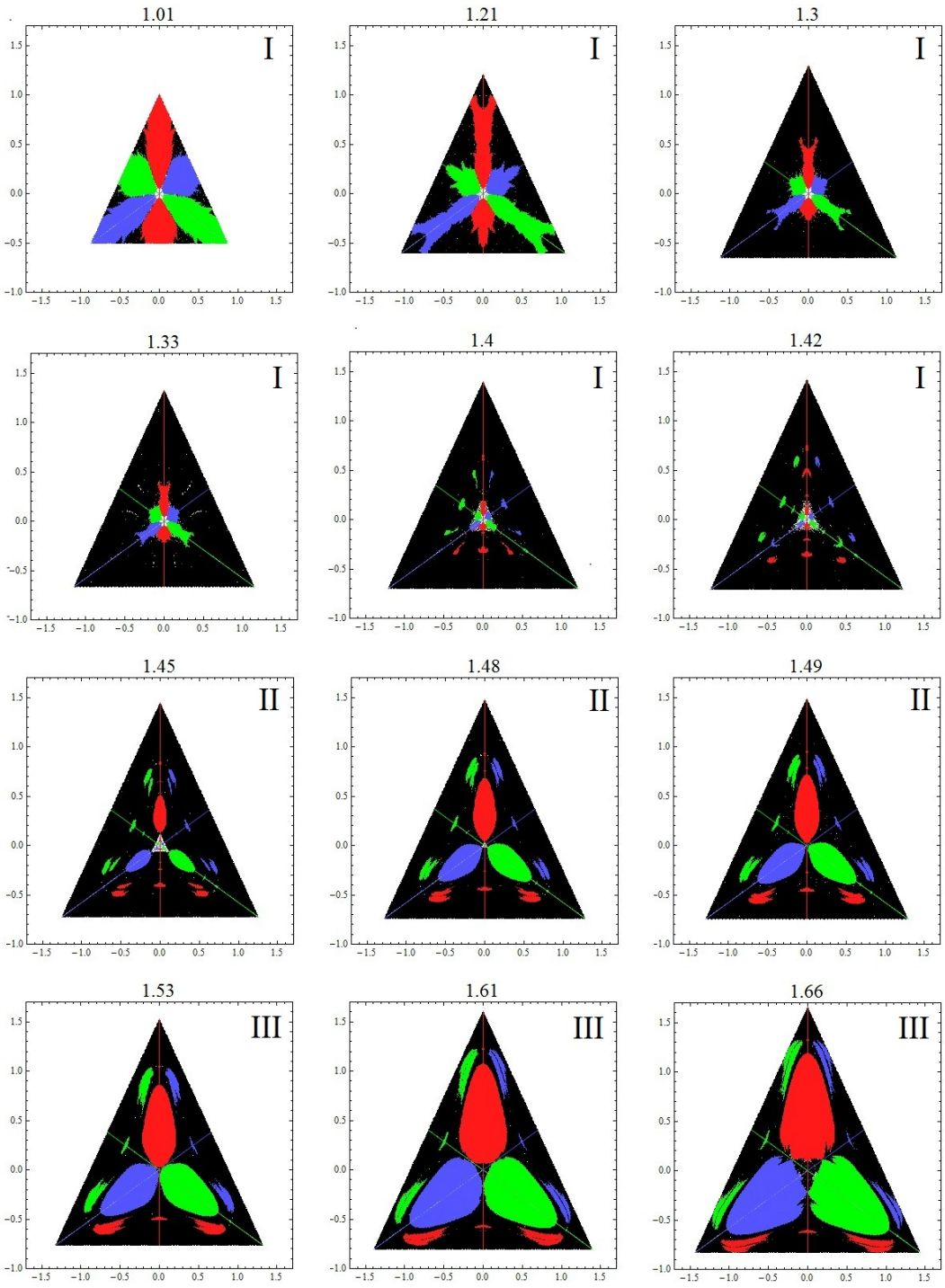

Figure 4.11: Symmetries of solutions starting with zero initial velocity and nonzero initial droplet volumes for various values of λ. In each case, black dots indicate S_3 symmetry, blue dots (12) symmetry, red dots (23) symmetry, green dots (13) symmetry and white dots no symmetry. Roman numerals indicate which region of parameter space each slice is from.

CHAPTER 5

NON-SMOOTH DYNAMICS OF A SWITCHING CAPILLARY DROPLET-BRIDGE SYSTEM

Abstract

A non-smooth model for a switching capillary system is studied. The system has alternative configuration-types: 'droplet-droplet', which consists of two spherical-cap droplets and 'bridge-droplet' which consists of an axisymmetric liquid bridge and a spherical-cap droplet where the bridge extends from the droplet holder to a nearby plate.). Total liquid volume and plate stand-off distance are the two scaled parameters that principally characterize the system. Surface tension is assumed to dominate throughout, keeping the shapes axisymmetric and thereby allowing the system to be modeled with ordinary differential equations. The limits of these assumptions are noted. Transitions between bridge and drop configurations are non-smooth. Moreover, these transitions occur at different places in phase space, resulting in a region in which the system is multiply-defined with consequent non-reversible dynamics. Each configuration-type is examined individually first to obtain two-parameter families of bifurcation diagrams. Oscillations within each configuration class, correspond to periodic orbits. The two configuration-types are then joined under the assumption that transitions are instantaneous with no loss of velocity across the joining transition. A two-parameter family of bifurcation diagrams for the bridge-drop switching system is then reported. Finally, the dynamics of configuration-switching trajectories are discussed. Hysteresis in transitions generates trajectories that lose energy in each cycle and dampen into periodic orbits within one of the two configuration types. By mapping to a semi-infinite cylindrical space it is shown that such trajectories may be understood solely by considering the region of space where the system is multiply defined.

5.1 Introduction

A 'capillary surface' is a liquid-gas interface whose shape is determined primarily by surface tension[3]. For typical liquids (e.g. water) in air, capillary surfaces occur on the millimeter or smaller scale where gravity has little influence on the shape. On these scales, the ratio of surface area to volume is high and many small surfaces may be coupled into a larger system (e.g. the veins of a leaf as part of a tree). That is, a capillary system is comprised of two or more coupled capillary surfaces. When the system can undergo a non-smooth transition, such as a breaking event, there can be complicated dynamics even if the dynamics within each configuration class exhibits only classical phase-plane behavior. The dripping faucet is an example and was an early system to be shown to be a chaotic system[53]. We examine a system consisting of two coupled capillary interfaces: a droplet and a surface that alternates between a bridge and a droplet. The droplet-droplet system and the drop-bridge system are each conservative phase-plane systems. However, when switching between configurations is allowed, complicated dynamics becomes possible. This system is a 2D system whose complexity arises from non-smoothness.

If each part (subsystem) of a capillary system exhibits more than one equilibrium state, then the number of equilibrium states for the full system scales nonlinearly. For example, a drop of water protruding from a hole under fixed pressure can exhibit one of two equilibrium states – a small droplet (sub-hemispherical) or a large drop (super-hemispherical). If n-droplets are coupled into a system where the system equilibrium is defined by a common pressure, the system will have 2^n equilibrium configurations, in general (2^{n-1} if the system is incompressible)[5]. From an energy perspective, such systems have a landscape with many energy wells. We are interested in dynamics that includes transitions where two or more of these

landscapes are stitched together. In this paper, a droplet-droplet landscape is glued to a droplet-bridge landscape.

A capillary system put into motion necessarily involves the flow of liquid underneath the liquid/gas surfaces. That is, inertia and/or viscous forces arising from the underlying fluid motion may influence the shape of individual elements and thereby the system. Our interest is in 'capillary-inertia' systems. These are frictionless – is assumed negligible. Liquid inertia tends to distort while surface tension tends to restore. Furthermore, we shall assume that the capillary surfaces individually and instantaneously will take equilibrium shape except for at the non-smooth jump-transitions, while system dynamics will be driven by pressure imbalances between capillary surface parts. This is referred to as the 'quasi-static assumption.' Finally, we shall track only the center-of-mass (COM) of the system. The governing model-equation can be written down from Newton's second law of the COM. In particular, we do not solve for the inviscid motions of the underlying liquid. As a consequence, we study ode systems. This allows us to focus on the non-smooth behavior and how it influences the global dynamics.

Our interest here is in dynamical-system aspects of model predictions. However, it should be noted that capillary-inertia systems exhibiting dynamics consistent with the above assumptions are observed. Capillary surfaces occur on length scales r where distortion due to gravity g is negligible relative to that due to surface tension σ,$\rho r^2 g/\sigma \ll 1$ (small Bond number), where ρ is liquid density. Effects due to viscosity μ on the motion are negligible relative to liquid inertia (away from solid boundaries) provided the Reynolds number based on capillary velocity scale $u = (\sigma/\rho r)^{1/2}$ is large, corresponding to $\mu/(\rho\sigma r)^{1/2} \ll 1$ (small Ohnesorge number). Finally, the quasi-static assumption is favored when the capillary time

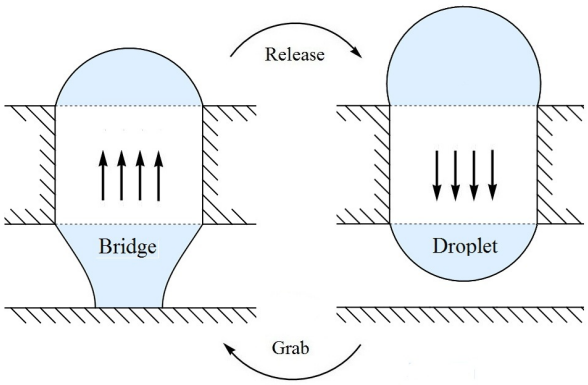

Figure 5.1: Schematic of cycling bridge-droplet system. As liquid flows from the bridge to the top droplet, the bridge shrinks until it breaks and transitions to a liquid bridge. If liquid then flows back to the bottom droplet it may grow until it impacts the substrate and reforms the liquid bridge.

scale is much shorter than the time scale for pressures to equilibrate between any two parts of the system. The latter depends on the height of energy barriers which, in this paper, varies with total liquid volume and stand-off distance, as will be made precise below. An example where these assumptions hold reasonably is the unforced drop-drop oscillator[1] and the forced-damped oscillator where chaotic motions are observed[45]. Comparisons of model predictions against experiment are made in both cases. Of course, the assumption of inviscid motion suffers the classical deficiency that weak damping occurs due to boundary layer effects near solid boundaries and thereby periodic motions of the model turn into under-damped oscillations in experiment. Here, the appropriate metric of comparison is the frequency of the oscillation – which compares well in the above studies. (Circumstances where viscosity dominates the flow between capillary surfaces, otherwise modeled similarly, have been studied [11, 5].)

Consider two coupled capillary-surfaces, formed by overfilling a cylindrical tube, the drop holder, with liquid so that droplets protrude from both ends, Fig-

ure 5.1(right). The system can oscillate between big-drop up and big-drop down via exchange of volume through the tube or vibrate about one of the two equilibria[1]. Now suppose a planar substrate with fixed stand-off distance is introduced below the tube. Depending on the stand-off, total system volume and initial conditions, the lower droplet may touch the plate and form a liquid bridge Figure 5.1(left). Since fat and thin bridges are possible, there can be oscillations within the drop-bridge configuration. If, during an oscillation, the bridge becomes slender enough to break, the system transitions back to a droplet-droplet configuration. In this way, one can anticipate a number of kinds of oscillations: drop-drop; drop-bridge; drop-bridge-drop; bridge-drop-bridge and so forth. We shall find that only certain of these oscillations can occur, however. Droplets and bridges are pinned on the circular tube edge, by assumption. Furthermore, the bridges are assumed to have a fixed contact-angle (taken to equal to $pi/2$, for simplicity). We shall refer to this as the 'fixed-angle' condition and label such bridges as 'pinned/angle' bridges.

The idea that coupled capillary surfaces, each pinned on the ends of a holder tube (Figure 5.1(right)), give rise to a bistable system has been known at least since the time of CV Boys [54]. Studies of the multiple equilibria that can arise from coupling various discrete capillary surfaces are motivated by low-gravity applications [55, 15], including a 'bucket with a hole, catastrophe theory classification for three droplets [39], biophysical studies of release from vesicles [56] and capillary switch applications [5, 34] which include a bridge and two droplets [40], where as many as 5 stable equibria can be arranged, and n-droplets [5] (with $n > 2$) where there are typically n stable equilibria. Studies of the inviscid dynamics of two or more coupled interfaces which resolve underlying inviscid motions include sloshing in a tube [57] and a spherical-drop pinned on a latitudinal circle [58]. An additional study that does not resolve the underlying inviscid motions (i.e. that is based on

COM motions) – in addition to those mentioned above – considers n droplet oscillators [47]. Finally, a preliminary experimental study examined the pressure 'kick' needed to switch between drop-drop and drop-bridge configurations; that is, the pressure pulse needed to impart to the top drop, Figure 5.1(right), to achieve the bridge below, Figure 5.1(left) [59, 60, 61].

Applied motivation for this study is the development of capillary adhesion devices. Drawing inspiration from the adhesion abilities of a leaf beetle found in nature, a switchable adhesion device has been engineered. The device combines two concepts: the surface tension force from a large number of small liquid bridges can be significant (capillarity-based adhesion) and these contacts can be quickly made or broken with electronic control (switchable). The device grabs or releases a substrate in a fraction of a second via a low-voltage pulse that drives electroosmotic flow. Notably, the device maintains the integrity of an array of hundreds to thousands of distinct interfaces during active reconfiguration from droplets to bridges and back, despite the natural tendency of the liquid toward coalescence. The device features compact size, no solid moving parts, and is made of common materials.[11, 2].

We are interested in the dynamics of transitions that can occur abruptly due to a breaking or joining of capillary elements. In between the breaking or joining events the system is conservative. At the instant of the event, the dynamics are non-smooth due to a change in the definition of the dynamical system.

The two non-smooth changes we shall consider are shown in Figure 5.2, denoted by 'grab' and 'release.' The terminology arises from the grab-release application that motivates this study. This pV response diagram shows drop (upper branch) and bridge (lower branch) equlibrium shapes. The arrows indicate instantaneous

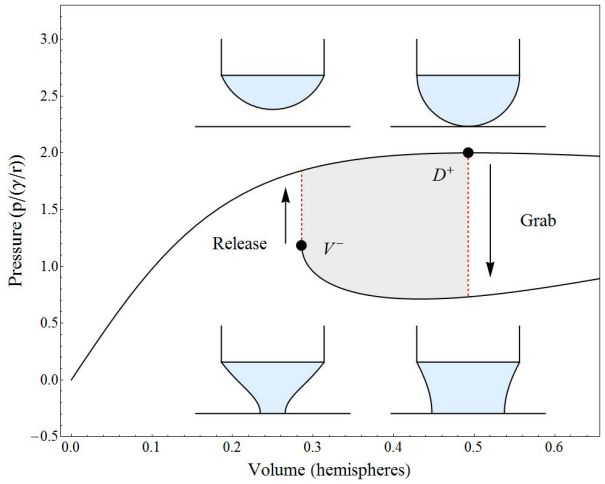

Figure 5.2: Non-smooth transitions of the capillary pressure in a bridge-droplet cycle. When the droplet volume reaches D^+ it impacts the wall and transitions to a liquid bridge, thereby decreasing capillary pressure. Then, if the bridge shrinks until point V^- it will break and transition back to a droplet.

non-equilibrium transitions. When the droplet impacts the substrate ('grab') at volume D^+, the pressure jumps to a lower value, whereas if the bridge volume reaches V^- it jumps to a higher pressure. The instantaneous nature of the transitions manifest as non-smoothness in the governing equations. Volume D^+ is set by the plate stand-off distance while volume V^- marks the turning point in the bridge response. This is the point of instability to constant-volume disturbances. It is important to note that grab and release occur at different volumes; between V^- and D^+ bridges and droplets coexist with the same volume. This can be thought of as hysteresis in the system response diagram. The system may also undergo other transitions. The first is a bifurcation to non-axysymmetric bridge shapes and marks a maximum-volume limit of the bridge. This type of bifurcation is either a sub- or super-critical bifurcations and has been documented[15]. The second occurs when a droplet reaches an negative hemispherical shape – beyond which the shape would intersect the tube wall. This marks a limit of physical

reasonableness; in experiment depinning of the contact-line would likely ensue.

When varying parameters, the system may also undergo a 'boundary equilibrium bifurcation' (BEB). This occurs when an equilibrium point reaches a non-smooth boundary and disappears[62]. The non-smoothness of the system also results in interesting non-reversible dynamics, primarily due to hysteresis in the state diagram. The system is multiply-defined between V^- and D^+ in Figure 5.2. This differs from many classic examples in non-smooth dynamical systems. In typical second-order non-smooth systems reported in the literature, the boundary is a line in phase space[63]. Drop-bridge hysteresis produces trajectories that spiral down to a periodic orbit in one of the two phase planes corresponding to the two configurations. Furthermore, in the context of a semi-infinite cylindrical space, *the long term behavior can be described solely by the dynamics in the region where the system is multiply-defined.*

The remainder of the paper is organized as follows. In section two the bridge-drop system is considered. A non-smooth dynamic model is formulated and analyzed. Bifurcation diagrams are constructed using the total volume and stand-off distance (bridge length) as parameters and the dynamics are discussed. In section three the non-smooth switching system is considered by combining the model from section two with an equivalent model of two coupled spherical-cap droplets. Bifurcation diagrams are constructed and the dynamics are discussed.

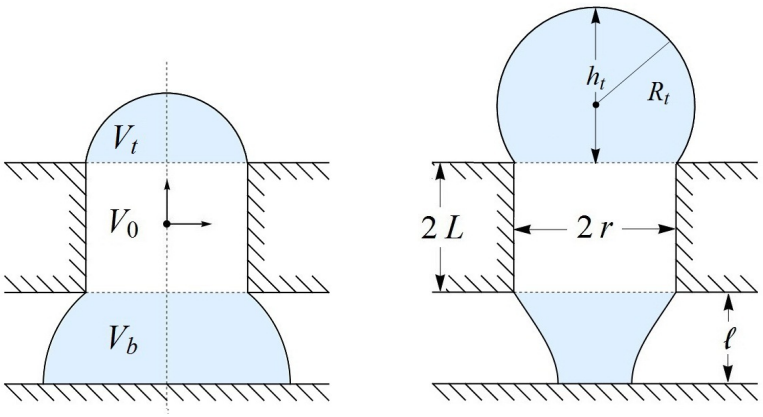

Figure 5.3: Schematics of the bridge-droplet system showing both rotund and slender bridges.

5.2 Bridge-Drop System

5.2.1 Model Formulation

Consider a cylindrical tube of length $2L$ and radius r filled to overflow with liquid so that droplets protrude. If a planar substrate is introduced close enough below the tube, for a partially-wetting liquid/substrate combination, the lower droplet will 'grab' the substrate and form a liquid bridge. Droplet and bridge are confined to axisymmetric static equilibrium shapes. For droplets, these are spherical-caps. As a result, the center-of-mass z_c of liquid volume $V_T = V_0 + V_t + V_b$ is axial. Here, V_t and V_b are bridge and droplet volumes (top and bottom), ℓ the 'stand-off' distance (gap length), and σ surface tension. Then, under the capillary-inertia assumption, Newton's second law for the COM can be written,

$$\frac{d}{dt}\left(\rho V_T \frac{dz_c}{dt}\right) = F_b - F_t \tag{5.1}$$

where $F_b = \pi\sigma r^2 p_b$ and $F_t = \pi\sigma r^2 p_t$ are capillary pressure forces resulting from curvature of the bridge and droplet, respectively. The spherical-cap droplet of

radius R_t has capillary pressure $p_t = 2\sigma/R_t$ by Young-Laplace, whereas the bridge pressure $p_b = p_b(V_b, \ell)$ and is found by solving numerically for bridge equilibria using AUTO[64] (see section 5.2.2).

It is convenient to non-dimensionalize by scaling lengths with r, volumes with $(4/3)\pi r^3$ and time with $\sqrt{\rho r^3/\sigma}$. Using these scalings and substituting the forces into equation (5.1) yields

$$\frac{d^2}{dt^2}\left(\rho V_T z_c\right) = \frac{3}{4}\left(p_b(V_b, \ell) - \frac{2}{R_t}\right) \tag{5.2}$$

in which all quantities are non-dimensional, yet employ the same notation as previous dimensional quantities.

Taking the origin to be the midpoint of the tube, the spherical-cap droplet's volume, center-of-mass and radius-of-curvature may all be written in terms of its height. The (non-dimensional) volume is given by $V_t = (1/8)h_t(3 + h_t^2)$, center-of-mass by $z_t = (1/2)h_t(2+h_t^2)/(3+h_t^2)$ and radius of curvature by $2R_t = (h_t + 1/h_t)$. Overall center-of-mass z_c is related to droplet and bridge centers-of-mass by $z_c V_T = (L + z_t)V_t - (L + z_b)V_b$, where $z_b = z_b(V_b, \ell)$ is the bridge center-of-mass relative to the bottom of the tube and is found numerically in the next section. Then equation (5.2) may be written

$$\frac{d^2}{dt^2}\left[(L + z_t)V_t - (L + z_b)V_b\right] = \frac{3}{4}\left(p_b(V_b, \ell) - \frac{2}{R_t}\right). \tag{5.3}$$

In addition, by inverting the cubic expression for V_t above, the droplet height h_t can be expressed as function of its volume $h_t = h(V_t)$. Furthermore, the fact that the combined bridge and droplet volume $\lambda = V_b + V_t$ is fixed may be exploited by replacing V_t by $\lambda - V_b$. Now, all quantities may be written as functions of the independent variable V_b and the parameters λ, L and ℓ. In summary, if $h_t =$

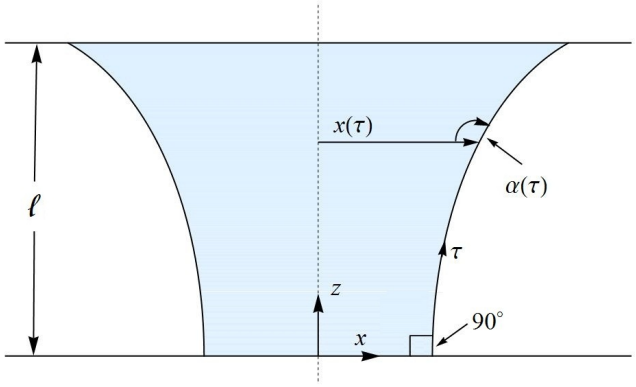

Figure 5.4: Definition sketch: liquid bridge has fixed (scaled) radius $x = 1$ at top and fixed contact angle of $pi/2$ at bottom.

$h(V_t) \equiv H(V_b, \lambda)$ and $R_t \equiv R(V_b, \lambda)$ similarly, equation (5.3) becomes

$$\frac{d}{dt}\left(\left[\frac{2}{3}H + 2L + z_b\right]\dot{V}_b + \dot{z}_b V_b\right) = \frac{3}{4}\left(\frac{2}{R} - p_b\right). \tag{5.4}$$

5.2.2 Liquid-Bridge Shapes

Liquid bridge static equilibrium shapes are obtained by solving the Young-Laplace equation, $p_b = \sigma\kappa$, where σ is surface tension and κ mean curvature. The Young-Laplace equation can be written in terms of arclength-angle coordinates (τ, α) as defined in Figure 5.4. Scale as in section 5.2.1. In particular, the Young-Laplace equation for a liquid bridge with pinned radius at the top ($x = 1$) and fixed contact angle of $pi/2$ degrees at the bottom, respectively, takes the form of the two-point boundary-value problem:

$$d\alpha/dt = (\sin\alpha)/x - p, \quad \alpha(0) = pi/2 \tag{5.5a}$$

$$dx/dt = -\cos\alpha, \qquad x(s) = 1 \tag{5.5b}$$

$$dz/dt = \sin\alpha, \qquad z(0) = 0. \tag{5.5c}$$

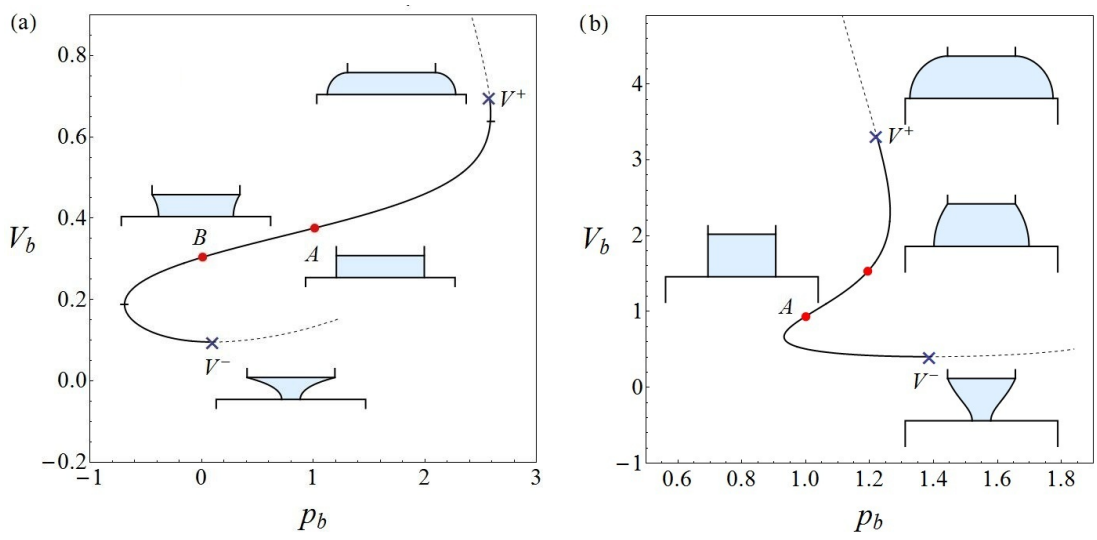

Figure 5.5: (pV) diagrams for pinned/angle $(pi/2)$ bridges of length $\ell = 0.5$ (a) and $\ell = 1.25$ (b). V^+ are maximum bridge limits (rotund), V^- minimum volume limits and breaking points. Dots A and B represents cylindrical bridges ($p_b = 1$) and the catenoid ($p_b = 0$) respectively.

The total arclength s is defined by the condition $\ell = \int_0^s x'dt$, the bridge volume by $V = (3/4)\int_0^s x^2 z'dt$ and the center-of-mass by $z_b = \ell - (3/4V)\int_0^s x^2 zz'dt$ (taking the system origin to midpoint of the tube as in Section 5.2.1). Solving this boundary value problem is a standard calculation[14]; AUTO is used and results are displayed in pV diagrams for various fixed lengths ℓ.

5.2.3 Phase-plane Boundaries

Consider the pV diagram for $\ell = 0.5$ and 1.25 (Figure 5.5a and b). First, observe that there is both a maximum V^+ and a minimum V^- admissible volume. If the bridge volume reaches V^-, the bridge pinches off leaving a bottom droplet on the holder. However, if the bridge-volume reaches V^+, a bifurcation to non-

axisymmetric shapes occurs.

Depending on where in parameter space they occur, these bifurcations may lead to non-axisymmetric shapes or to broken bridges[15]. The admissible region of bridge volumes ($V^- \leq V \leq V^+$) is plotted as a function of length ℓ in Figure 5.6 (left), where V^- is the solid line and V^+ the dashed line. The maximum length V^+ limit occurs at the 'rotund limit' (contact angle π), while V^- is the volume turning point. Point A is the cylindrical bridge where pressure $p_b = 1$; point B is the catenoid where $p_b = 0$.

Note that in solutions to equation (5.4) there is another bound for V_b that relates to droplet volume V_t. For physically relevant shapes, the lower bound for the droplet volume is a negative hemisphere within the tube. This corresponds to $V_t = -0.5$ or $V_b = \lambda + 0.5$. Thus, the system maximum volume V^* is defined as

$$V^* = \min\left[V^+, \lambda + 0.5\right], \tag{5.6}$$

and for a fixed total volume λ and length ℓ the system is defined for $V_b \in (V^-, V^*)$.

The focus of study will be restricted additionally to bridges with $\ell > 0.5$ (i.e. half the radius) since very short bridges are unstable to nonaxisymmetric perturbations before reaching V^-. The family of bridges considered here is related closely to pinned/pinned bridges (e.g. $x(0) = x(1) = 1$) because a pinned/angle bridge may be generated from the top-half of a pinned/pinned bridge symmetric about the midplane. In other words, a family of equilibrium shapes for the pinned/pinned case can be obtained from a family of pinned/angle by doubling volume and length while holding pressure constant. If the pinned/angle bridge is replaced by the pinned/pinned bridge, a similar bifurcation structure is observed (Appendix 5.5.1).

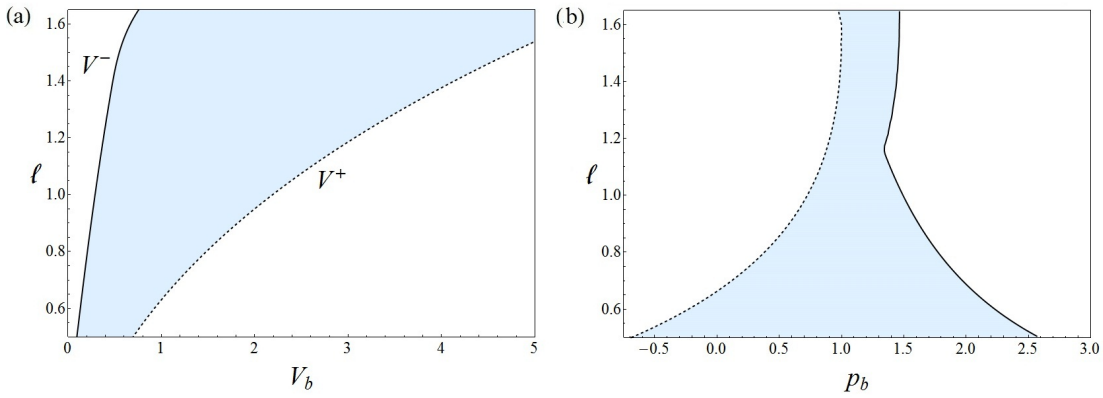

Figure 5.6: (a) Admissible bridge volumes: solid boundary is V^- while dashed boundary is V^+. (b) Admissible bridge pressures: the kink occurs when the maximum pressure changes from a pressure turning point to the minimum bridge length V^-.

5.2.4 Bifurcation and Stability

The bridge-droplet system is in equilibrium when the capillary pressures of the spherical-cap droplet and the liquid bridge are equal (i.e. $p_b = p_t = p$). For example, consider a droplet and a bridge with $\ell = 1.25$, whose pV diagrams are superimposed in Figure 5.7. For a pressure $p = 1.4$ (dot-dashed line), there are four pairs of equilibria: $(d_1, b_1), (d_1, b_2), (d_2, b_1)$ and (d_2, b_2). Using these equilbria of the bridge and drop in pV response, the system pV response can be constructed. However, for our purposes, traditional bifurcation diagrams present the equilibrium structure in a more convenient format.

Sample bifurcation diagrams in (λ, V_b) space for different bridge lengths are shown in Figure 5.8. Solid lines indicate 'centers', dashed lines 'saddle points', and $\times$ symbols 'boundary equilibrium bifurcations' (BEB). BEB occur when the bridge reaches either its minimum V^- or maximum V^+ volume and the bifurcation

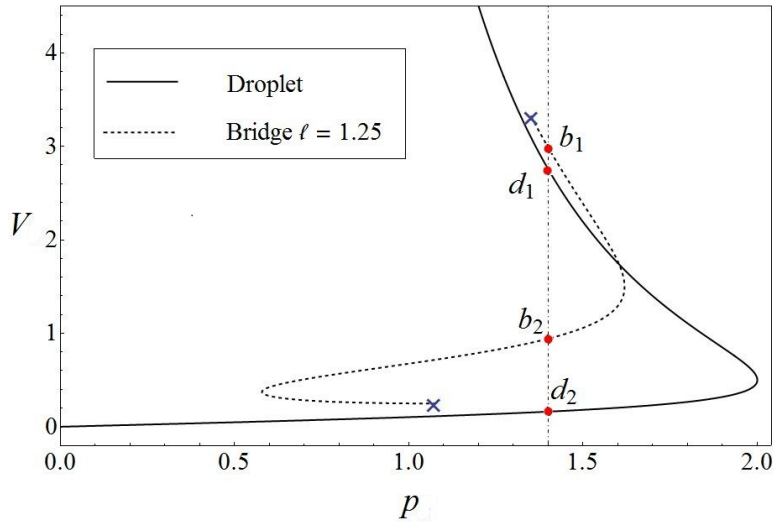

Figure 5.7: Superimposed pressure-volume diagrams for a spherical-cap droplet and pinned/angle bridge of length 1.25. The system is in equilibrium for bridge and droplet points on the same vertical line (e.g. pairs $(d_1, b_1), (d_1, b_2), (d_2, b_1)$ and (d_2, b_2)).

curve ends. Dots indicate locus of shapes shown.

For short bridges there is a single curve of stable centers (Figure 5.8A). Such a curve originates when a BEB occurs at a nonzero λ value (point a) with bridge volume V^-. As λ increases, the bridge volume grows until it reaches a maximum (point b) such that the bridge and droplet have $p = 2$; note that $p = 2$ is the greatest shared pressure for such short bridges. Figure 5.6b shows max and min bridge pressure as a function of stand-off distance ℓ while Figure 5.7 indicates the droplet has maximum pressure of two. As λ is further increased, the droplet assumes the majority of the volume; consequently, the branch approaches a zero pressure bridge asymptote since $p_t \to 0$ as $V_t \to \infty$.

If the length of the bridge is increased, a saddle-node bifurcation occurs and a second branch is born (Figure 5.8B). This new branch begins and ends at $V_b = V^+$ (point e) and consists of an upper branch of centers and lower branch of saddle

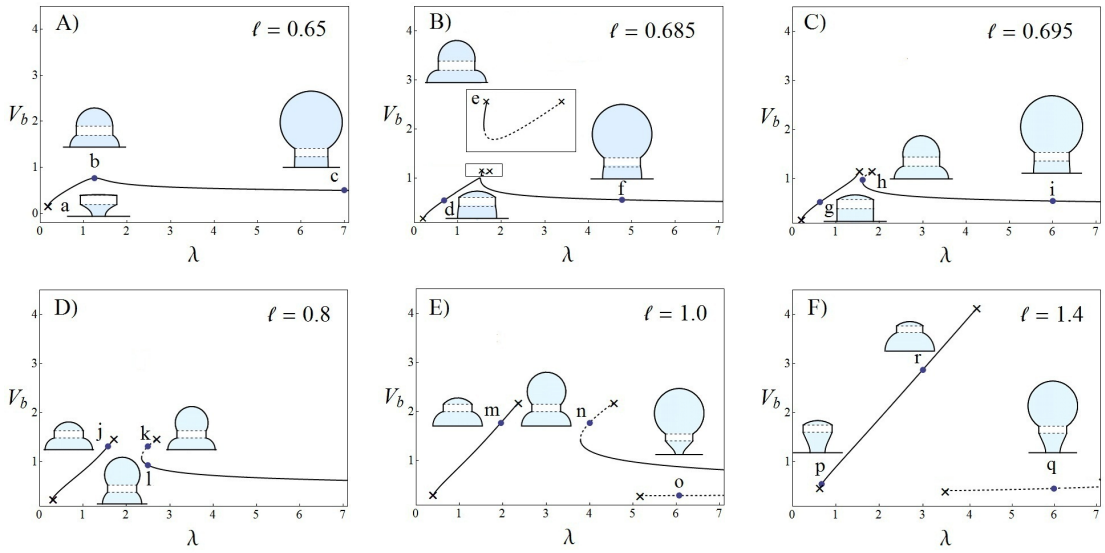

Figure 5.8: Bifurcation diagrams for varied bridge lengths. A cusp bifurcation occurs between $\ell = 0.685$ and $\ell = 0.7$. Solid lines denote centers while dashed lines denote saddle points. Boundary equilibrium bifurcation points are labeled with $\times$.

points. The appearance of this branch causes the number of equilibria to change as follows λ increases: one – three – two – one. A slight increase in length forces the two curves of equilibrium points to intersect and exchange branches. Figure 5.8C shows the system just after the exchange. For a brief parameter window the system still exhibits three equilibrium points near the intersection point, but as ℓ increases, the two curves of equilibrium points quickly separate, leaving a region with no equilibria between them (Figure 5.8D). Thus, as λ grows, (at these lengths) the number of equilibria evolves as one – zero – two – one.

As the bridge length is increased significantly, another branch of saddle points appears, for which the bridge volume is very small (Figure 5.8E). At the same time, the saddle-node curve moves to the right until it vanishes from the parameter window (Figure 5.8F). Observe that if the parameter window were expanded

to include larger λ values, the lowest two branches would join in a saddle-node bifurcation and disappear (e.g. for $\ell = 1.0$ this occurs when $\lambda = 21.4$). Additionally, note that in each plot, two equilibrium points on a horizontal line correspond to the same bridge volume and droplets with reciprocal heights (i.e. they are pieces of the same sphere). Examples of such pairs are (j, k), (m, n) and (p, q).

5.2.5 Phase-Plane Dynamics: Two-Parameter Family

The exchange of branches shown in Figure 5.8 is the hallmark of a cusp bifurcation. Figure 5.9 shows a two parameter bifurcation diagram (λ and ℓ) where such a cusp occurs at $(\lambda, \ell) = (1.528, 0.687)$. The cusp manifests on a curve of saddle-node bifurcations (solid line in the figure). However, there are other lines of BEBs; these lines correspond to the bridge attaining either its maximum (V^+) or minimum (V^-) volume. Dashed lines indicate the bridge reaching V^+ while dot-dashed lines indicate a bridge reaching V^-. Each region is labeled by its types of equilibria, ordered by increasing bridge volume. For example, in the region labeled (C, S), the bridge volume for the center is less than that of the saddle point (e.g. $\lambda = 4$ in Figure 5.8E), while in the region labeled (S, C) the bridge has more volume at the saddle point than the center (e.g. $\lambda = 4$ in Figure 5.8F).

Another future shown in Figure 5.9 is the phase-plane dynamics. The phase-plane trajectories consist of: closed orbits, equilibrium points, homoclinic orbits, and solutions that begin and end at one of the two boundaries. In each plot, bridge volumes are bounded on the left by V^- and on the right by the maximum system volume V^* defined in equation (5.6). A trajectory that reaches V^* is considered to go 'out-of-bounds', while reaching V^- is understood to imply the system 'switches' to the droplet-droplet state considered later.

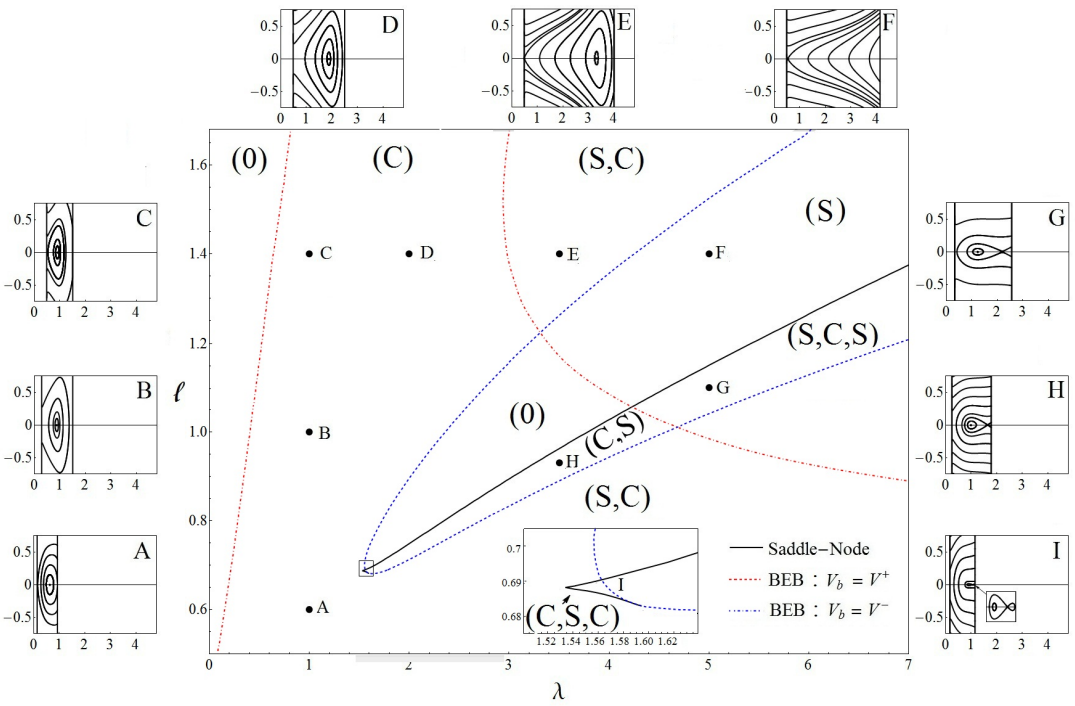

Figure 5.9: Bridge-drop two-parameter bifurcation diagram: total volume λ and bridge length ℓ. Each region is categorized by its types of equilibria, ordered by increasing bridge volume. Centers are labeled C and saddle points S. Phase-planes $(V_b, \dot{V}_b)$ for various points are also shown, where the left and right boundaries are the breaking point V^- and out-of-bounds limit V^* respectively.

In general, moving upwards on the bifurcation diagram shifts the right boundary V^* from V^+ to $\lambda + .5$. After this change, the right boundary will no longer move to the right. For example, movement from $A \to B$ shifts the right boundary, whereas from $B \to C$ does not. Moving from $C \to D \to E \to F$ forces the center to move to the right until it reaches the right boundary and disappears in a BEB. Also of note is that for points E and F, the saddle point remains very close to the boundary V^-.

Consider point F. If the length of the bridge is decreased ($F \to G$), then

a saddle-node bifurcation results in a region with a center separating two saddle points. Decreasing the bridge length further causes the larger saddle point and, in turn, the center to disappear.

In the center of the plot (0) there is a region with no equilibrium points where a BEB has destroyed the center and the saddle node bifurcation has not occurred. Following the saddle-node bifurcation (point H), there is a center and a saddle point. Furthermore, moving downward and to the left (toward the cusp), results in the phase-space shrinking. For example, point I has three equilibrium points that are nearly indistinguishable from a single equilibria.

Of particular interest are trajectories that reach one or both boundaries. In the next section we will view the bridge-droplet joined to a droplet-droplet model to create a system that can switch between configurations. In that case, when the bridge breaks at the left boundary (V^-) it reforms as a droplet.

5.3 Combined Bridge-Drop Configuration-Switching System

In order to observe noteworthy dynamics, it is desirable to explore a part of phase space in which trajectories that begin at the left boundary V^- do not in general terminate at the right boundary V^*; the aim is to have switching oscillations that do not go 'out-of-bounds' (i.e. reach V^*). A brief examination of the phase spaces presented in Figure 5.9 indicates that the most promising region is near points B and C. That is, consider $\ell \in (1, 1.5)$ and $\lambda \approx 1$.

As the bridge-droplet system oscillates the bridge may reach its minimum vol-

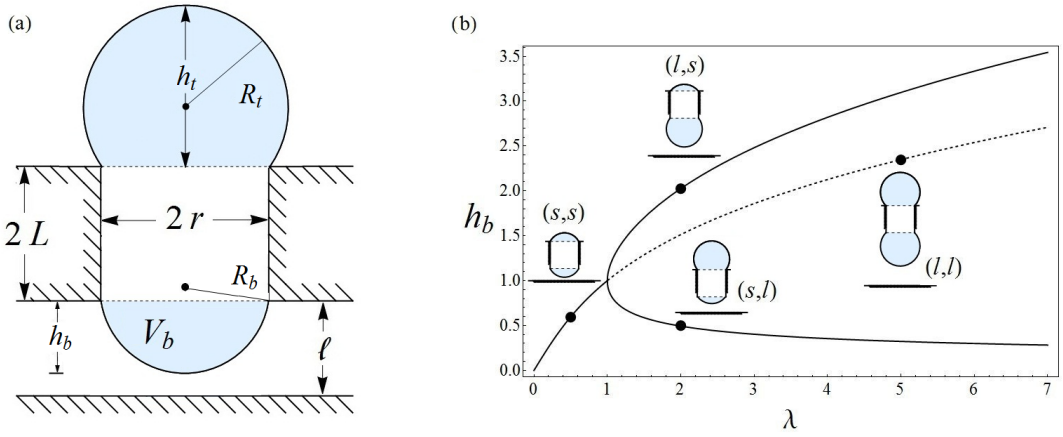

Figure 5.10: Droplet-droplet (a) schematic and (b) bifurcation diagram with typical equilibrium shapes. Solid lines indicate centers and dashed saddle points.

ume V^- and release from the substrate. When this occurs, the bridge pinches off at the substrate and transitions to a spherical-cap droplet. We shall assume that no drop remains on the substrate, for simplicity. That is, all the liquid from the broken bridge ends up in the bottom droplet After release, the system is two coupled spherical-cap droplets; this configuration has been studied previously[1, 45]. For the bottom drop in the holder, let V_b, z_b, h_b and R_b be the volume, center-of-mass, height and radius of curvature of the bottom droplet, that is, the droplet adjacent to the substrate, respectively (Figure 5.10a). Then, scaling as in section 5.2.1, these quantities may be written similarly. Thus, Newton's second law may be written

$$\frac{d^2}{dt^2}\left[V_t z_t - V_b z_b\right] = \frac{3}{2}\left[\frac{1}{R_b} - \frac{1}{R_t}\right]. \tag{5.7}$$

The two droplets can return to the bridge-droplet state if the droplet hits the substrate; this occurs when $h_b = \ell$. Upon impact, the droplet re-transitions to a liquid bridge. We will treat transitions between states as instantaneous.

We can now specify the configuration-switching bridge-droplet system in terms of a discontinuous dynamical system using the piecewise definition

$$\frac{d^2}{dt^2}\left[V_t z_t - V_b z_b\right] = \begin{cases} \left(\frac{3}{4}p_b - \frac{3}{2R}\right) & \text{if bridge-droplet} \\ \left(\frac{3}{2R_b} - \frac{3}{2R}\right) & \text{if droplet-droplet} \end{cases} \tag{5.8}$$

Note that here the subscript b refers to the either the bottom droplet or the bridge depending on the current configuration.

The transition from bridge-droplet to droplet-droplet occurs when $V_b = V^-$, while the transition from droplet-droplet to bridge-droplet occurs when the height of the droplet is equal to the gap length ℓ. Let $V_b = D^+$ when $h_b = \ell$. Note that, by assumption, in this model, no velocity is lost during these transitions. Simple calculations show that $V^- < D^+$ for gap lengths greater than 0.5, which corresponds to the the bridge lengths of interest. In other words, for the class of bridges studied, the bridge always breaks at a volume less than the maximum droplet volume. Consequently, the system exhibits hysteresis in transition, due to the system being multiply-defined for V_b between V^- and D^+. As we will see, this characteristic is fundamental to trajectory dynamics.

5.3.1 Drop-Drop System Recapitulation

A bifurcation diagram for the configuration-switching system requires combining the diagrams of the bridge-droplet (Figure 9) and droplet-droplet (Figure 5.11) subsystems. To that end, we now consider the droplet-droplet state defined in (5.7); it is in equilibrium when the radius of curvature of both droplets are equal. The (h_b, λ) bifurcation diagram is easily constructed using the relationships defined in Section 5.2.1 (Figure 5.10b) since $R(h) = 1/2(h + 1/h)$ which occurs when the

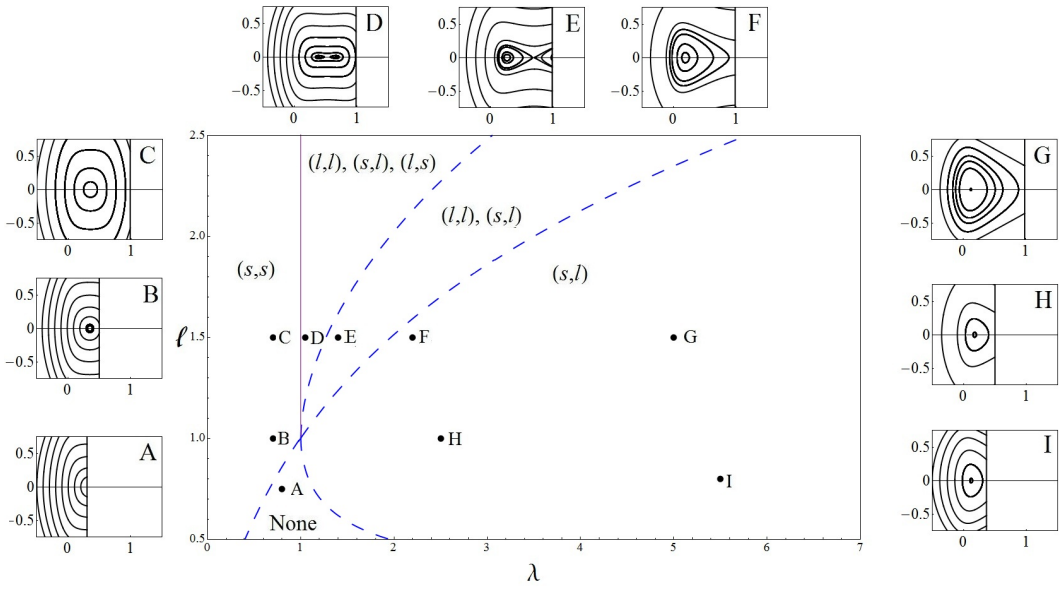

Figure 5.11: Droplet-droplet two-parameter bifurcation diagram. Solid lines indicate pitchfork bifurcations while dashed indicate boundary equilibrium bifurcations. In each region the types of equilibria are listed: s indicates sub-hemispherical (small) and l super-hemispherical (large) . Phase planes $(V_b, \dot{V}_b)$ for various labeled points are also shown, where the right boundary is the impacting point D^+.

two droplets have the same height ($h_t = h_b$) or reciprocal heights ($h_t h_b = 1$). When $\lambda < 1$, there is a single stable center such that the droplets are identical and sub-hemispherical (s, s). At $\lambda = 1$ a pitchfork bifurcation occurs, resulting in the loss of stability of the identical solution and in two pitchfork branches being born, consisting of stable centers. On the pitchfork branches, one droplet is large and the other is small (l, s or s, l); the identical state is now a saddle point with both droplets large (l, l).

When a substrate is introduced, the bottom droplet has a maximum height of ℓ. Thus for any fixed stand-off distance ℓ, the number of equilibrium points as a function of λ is the number of points below $h_b = \ell$ in Figure 5.10. This corresponds

to the two-parameter bifurcation diagram shown in Figure 5.11, in which the solid line and the dashed lines are curves of pitchfork and boundary equilibrium bifurcations respectively. For $\lambda < 1$, if the stand-off is greater than the dot-dashed curve, there is a single equilibrium point labeled (s, s) (e.g. points B and C) and no equilibrium points otherwise (e.g. point A). At $\lambda = 1$ a pitchfork bifurcation occurs, though the number of equilibrium points is dependent on ℓ (i.e. there can be zero, one, two, or three equilibrium points). If there are three equilibrium points, they manifest as two centers separated by saddle and are labeled accordingly as $(h_b, h_t) = (l, s), (s, l), (l, l)$ (e.g. point D). As ℓ decreases (or λ increases) the top curve disappears (h_b large and h_t small) in which case there are two equilibrium points labeled (l, l) and (s, l) (e.g. point E). Continuing to lower ℓ makes the (l, l) saddle-point point vanish (e.g. points F, G, H and I). Finally, for very short gaps the (s, l) center will disappear, leaving no equilibrium points.

5.3.2 Configuration-switching system: equilibria

A two parameter bifurcation diagram for the combined switching system can now be constructed by combining the diagrams for the bridge-droplet (Figure 5.9) and droplet-droplet (Figure 5.11), resulting in a (λ, ℓ) bifurcation diagram for the combined system (Figure 5.12). In the diagram, thin and long-dashed lines are drop-drop pitchfork and BEB bifurcation lines, while the thick and short-dashed lines are saddle-node and BEB lines for the bridge-drop configuration.

The parameter space is sectioned into 13 regions, each with a different equilibrium structure. Droplet equilibria are referred to as $(h_b, h_t) = (s, s), (l, l), (s, l)$, or (l, s) and reflect the droplet heights. The bridge-droplet equilibria are ordered left-to-right by increasing bridge volume and classified by C, a stable center, and

S, a saddle point. Note that for the region of most interest ($\ell \in (1, 1.5), \lambda \approx 1$) there is a single bridge-drop equilibria (center) while there may be anywhere from zero to three drop-drop equilibria.

5.3.3 Configuration-switching system: Dynamics

When considering the dynamics of the switching system, the most interesting trajectories are those that cross one or more of the switching boundaries (V^- and D^+), but do not reach the system maximum volume (V^*). As stated previously, the most promising parameter range is $\lambda \approx 1$ and $\ell \in (1, 1.5)$. Outside this region, nearly all trajectories that start at V^- will reach V^* and go out-of-bounds. Thus, for the remainder of this section, we consider only trajectories that do not reach the boundary V^*. Henceforth, references to 'all' trajectories means 'all trajectories that do not reach this boundary'.

Two examples of a switching trajectory are shown in Figure 5.13 for $\lambda = 1.1$, $\ell = 1.1$ and initial conditions $(V_b(0), \dot{V}_b(0)) = (1, -0.85)$ and $(0.9, -0.865)$. For these parameters, there is one bridge-drop equilibria (center) and two drop-drop equilibria (center and saddle). In the plots, solid lines indicate bridge-droplet states while dashed lines indicate droplet-droplet states. The three dotted vertical lines are the minimum bridge (V^-), maximum droplet (D^+) and system maximum (V^*) volumes. As previously discussed, during a trajectory the system can assume either the droplet-droplet or bridge-droplet state between V^- and D^+. The most striking characteristic of these trajectories is the 'dampening' down to a periodic orbit confined to one of the two states, despite the lack of active dissipation in the model. This behavior is to be a result of hysteresis during transitions between configurations (cf Figure 5.2).

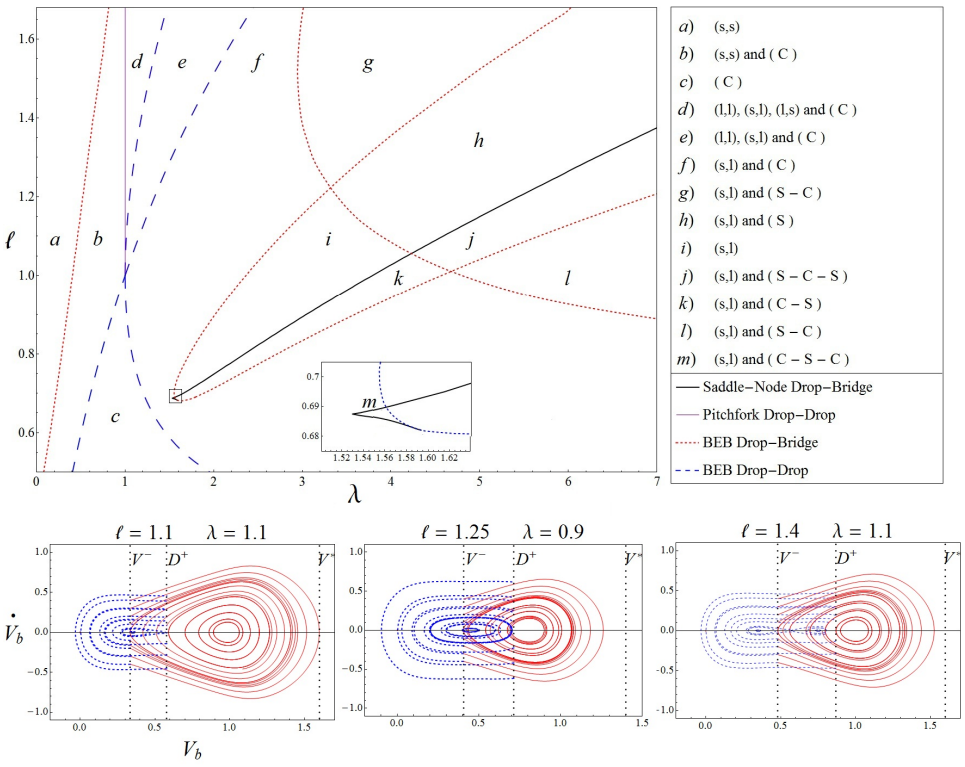

Figure 5.12: Configuration-switching two-parameter bifurcation diagram. Thick-solid and short-dashed lines are the boundaries in the bridge-droplet configuration; thin-solid and long-dashed lines are the boundaries for the droplet-droplet configurations. Each region is labeled and classified by the types of equilibria there. Sample phase portraits are also shown with solid lines indicating bridge-drop configurations and dashed lines drop-drop.

In each configuration, the system is a second-order conservative oscillator. As such, if the system switched at a vertical line in $(V_b, \dot{V}_b)$ space, it would follow that the entire system would be conservative. To clarify, recall that when a second-order conservative oscillator crosses a vertical line at a point $(V_1, \dot{V}_1)$ in $(V_b, \dot{V}_b)$ space, it necessarily crosses the same line at $(V_1, -\dot{V}_1)$. Since this is true on both sides of the switching line, it must also be true on the line. This implies that the system is conservative everywhere and all solutions must be fixed points, periodic orbits, homoclinc orbits or hetereoclinic orbits.

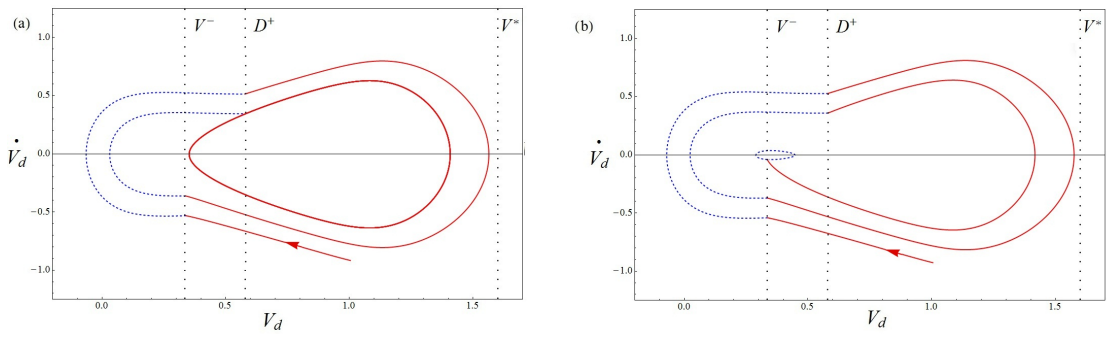

Figure 5.13: Switching trajectories for $\lambda = 1.1$ and $\ell = 1.1$ with initial conditions (a) $(V_b(0), \dot{V}_b(0)) = (1, -0.85)$ and (b) $(V_b(0), \dot{V}_b(0)) = (0.9, -0.865)$. Solid parts of the trajectory are bridge-droplets and dashed parts droplet-droplet. The dotted lines are the switching boundaries V^- (minimum bridge volume), D^+ (maximum droplet volume) and the 'out-of-bounds' boundary V^*.

In our system, the transition occurs at two different lines, namely $V_b = V^-$ and $V_b = D^+$. Consequently, the result is a region where the system is multiply-defined. The dynamics of all trajectories can be explained solely by considered only how they behave in the region between these two lines; this follows because if the trajectory leaves the region at $(V_b, \dot{V}_b)$ it returns at $(V_b, -\dot{V}_b)$. Thus, to determine the long-term behavior, only the behavior between V^- and D^+ are of import. Further, we can map into a semi-infinite cylindrical space by first confining the study to droplet-droplet configurations for $\dot{V} > 0$ and bridge-droplet configurations for $\dot{V} < 0$ and then joining the upper and lower-half planes via rotating the bottom half plane 180 degrees and moving it to the right of the top half half plane. This will now be illustrated with an example.

Consider the region (V^-, D^+) with the trajectory from Figure 5.13a. If only droplet-droplet configurations bridge-droplet configurations are plotted for $\dot{V} > 0$ and $\dot{V} < 0$ respectively, Figure 5.14a is obtained; outside of this region, the system

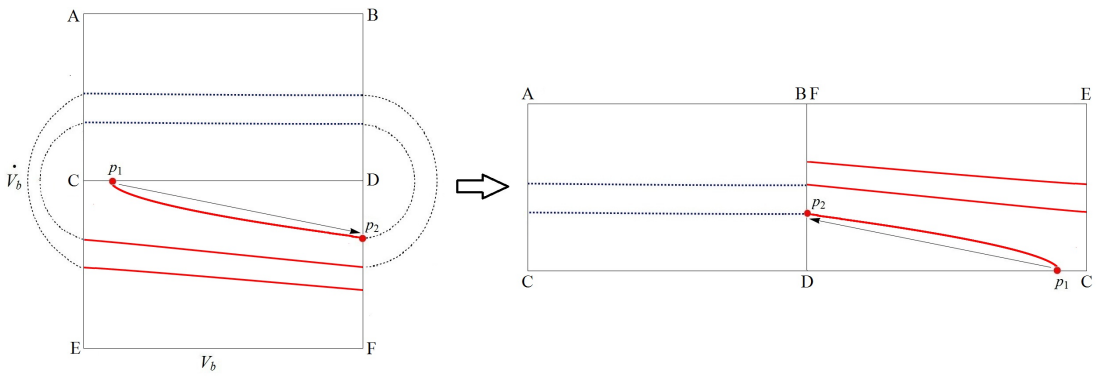

Figure 5.14: (a) trajectory from Figure 5.13a restricted to $V_b \in (V^-, D^+)$. Drop-drop points are plotted for $\dot{V}_b > 0$ while bridge-drop are plotted for $\dot{V}_b < 0$. Outside the region the trajectory is conservative and thus returns with the same speed. The trajectory shown spirals inward until it reaches a periodic orbit represented by the repeating line segment p2p1. (b) The trajectory from (a) mapped into a semi-infinite cylindrical space. Left and right edges are identified and the bottom edge represents escape to a periodic orbit.

is conservative. The trajectory returns to either boundary with the same speed as it left, allowing us to disregard the external dynamics. The shown trajectory spirals inward until it hits the $\dot{V}_b$ axis at p_1. Subsequently, it repeats its last oscillation (the line segment p_2p_1), which represents a bridge-droplet periodic orbit.

The trajectory can also be translated to a semi-infinite cylindrical space by cutting along the V_b axes and rotating the lower-half up and then positioning it to the right of the upper-half (Figure 5.14b). The left half of the space is bridge-droplet while the right droplet-droplet. Observe that the system is non-smooth at the mid-line as well as at the left- and right-edges which are identified with each other. If a trajectory reaches the bottom line, it enters a periodic orbit confined to one of the two configurations, which, in our figure, corresponds to its last line segment repeating indefinitely. One could alternatively view the bottom boundary

as escape from the cylindrical space to a non-switching periodic orbit.

For the parameter ranges considered, all trajectories calculated dampen down to a periodic orbit. Such behavior can be explained in the context of the phase portraits of the the bridge-droplet (Figure 5.9) and of the droplet-droplet (Figure 5.11) near their respective switching boundaries V^- and D^+. For the bridge-droplet, the magnitude of the velocity always decreases when approaching V^-. In contrast, for the bridge-bridge, the magnitude of velocity may increase as the trajectory approaches D^+, but we find that such an increase is insufficient for a net increase over one revolution in the cylindrical space.

5.4 Concluding Remarks

The model studied characterizes a capillary system that switches between bridge-droplet and droplet-droplet states. This system is noteworthy due to both its engineering applications (such as capillary adhesion) as well as its inherent mathematical complexity. The switching process involves breaking liquid bridges and droplets impacting on substrates, both of which are complicated non-smooth events. However, the system can be simplified by restricting bridges and droplets to static equilibrium shapes and assuming the transitions happen instantaneously so that an ordinary differential equation model may be obtained that captures a variety of interesting behavior. The non-smooth model is a piecewise second order-conservative oscillator that is multiply defined for a nonzero range of droplet values.

The bridge-droplet configuration is complicated due to a rich bifurcation structure. This structure is characterized in a two parameter bifurcation diagram (total volume λ and stand-off distance ℓ). Depending on parameter values, the number of equilibrium points varies from zero to three. Since liquid bridges have both a maximum and minimum volume, numerous lines of boundary equilibrium bifurcations (BEB) are computed. In addition, lines of saddle-node bifrucations are found and are shown to merge at a cusp bifurcation. The lines of BEBs and saddle-nodes intersect multiple times and give rise to nine different regions in the bifurcation diagram.

Once the bridge-droplet bifurcation structure is well understood, attention is turned to the switching system. Its bifurcation structure is obtained by combining the bridge-droplet diagram with a similar diagram for the droplet-droplet configuration. The result is a complicated two parameter bifurcation diagram that is partitioned into thirteen regions by the number, type and ordering of equilibria.

In these regions, bridge-droplet and droplet-droplet equilibria coexist and often reside in the region in which the system is multiply defined. The boundaries of the regions are lines of BEB, saddle-node (bridge-droplet) and pitchfork (droplet-droplet) bifurcations.

Finally, the dynamics of trajectories are studied. Since the system behaves as a typical second-order oscillator away from the non-smooth boundaries, the trajectories of interest are those that intersect one of the switching boundaries. We show that such switching trajectories 'relax' into periodic orbits that are confined to one of the two configuration spaces. Furthermore, by mapping trajectories to a semi-infinite cylindrical space it is shown that this relaxation is due to the behavior in the multiply-defined region. In other words, long term behavior can be obtained by considering only a slice of the phase space.

Further work is possible in a number of directions. One such extension is to explore other classes of bridges, for which the bifurcation structure will vary. For example, Appendix 5.5.1 explores the related family of pinned/pinned bridges. One complication to consider when examining other families is that, in general, the bridge pinches off at a place away from the substrate, resulting in two droplets (e.g. pinned/pinned bridges symmetric about a mid-plane pinch off at the midpoint). Thus, when the bridge breaks some volume will be left at the substrate. An additional modeling enhancement may account for how is that volume left may depend behind on the substrate may depends on the fluid velocity.

Other possible extensions include considering a system in which chaotic oscillations are possible (e.g. weakly dampened forced model) as well as incorporating the dynamics of impact and spreading into the model. With respect to the latter extension, as the droplet impacts the substrate, it spreads rapidly to form a liquid

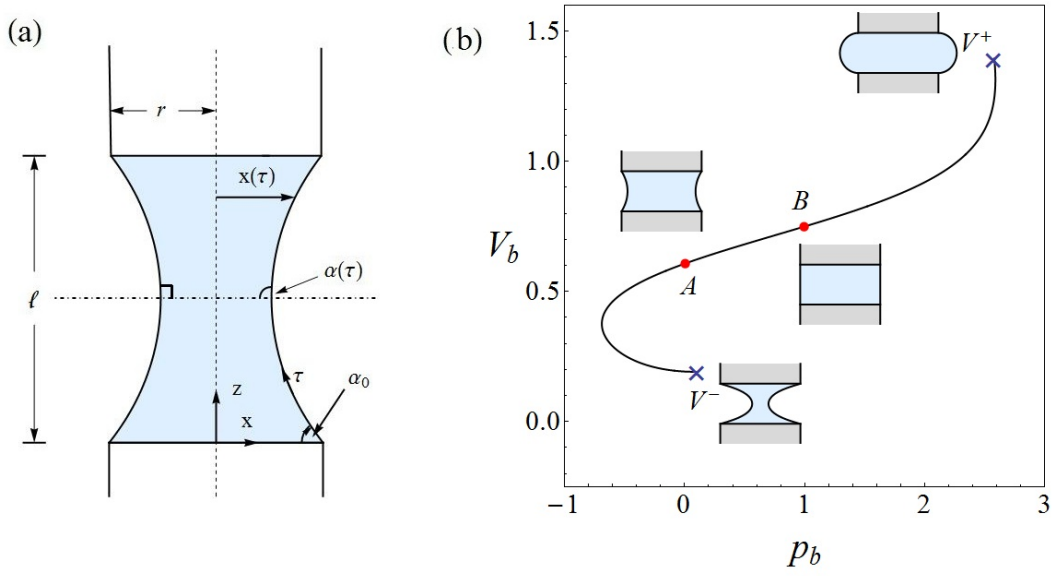

Figure 5.15: (a) Pinned-pinned bridge definition sketch. (b) (pV) diagram for a pinned-pinned bridge of length $\ell = 1.0$. V^+ and V^- are the maximum and minimum bridge limits respectively. A is a cylindrical bridge with $p_b = 1$ and B is a catenoid with $p_b = 0$

bridge. In the model considered here, this spreading is assumed to be instantaneous with no loss of velocity. In future work, the transition may be treated as fast when compared to the time scale of oscillation, resulting in a non-smooth multiple time-scale dynamical system.

5.5 Appendix

5.5.1 Pinned-Pinned Bridge System

The pinned-fixed-angle (90°) family of bridges is closely related to bridges that are pinned at both ends, a case we will now examine. Consider a bridge with radius

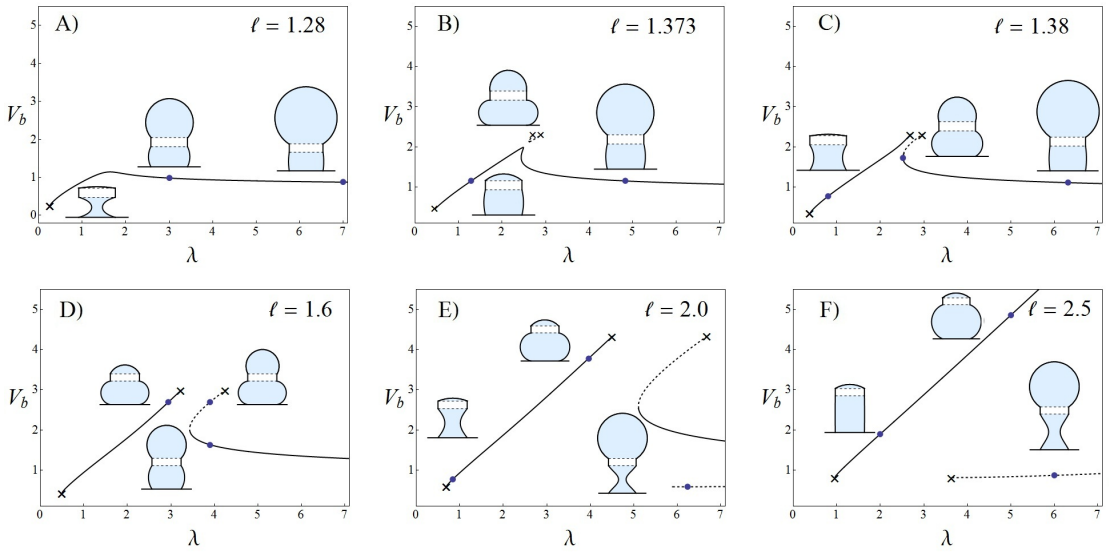

Figure 5.16: Pinned-pinned bridge-droplet bifurcation diagrams for different bridge lengths. Behavior of interest: cusp bifurcation between B and C; two saddle-node bifurcations in B. Solid lines denote centers while dashed lines denote saddle points. Boundary equilibrium bifurcation points are labeled with $\times$.

r at both ends (Figure 5.15a). Observe that equilibria are symmetric about the z axis as well as the midline. Further, at the midline, the contact angle is 90° which implies the top half of a pinned-pinned bridge is a pinned-fixed-angle bridge with half the height and half the volume. Moreover, since pressure is the same for full and half bridges, the results from Section 5.2.2 regarding pinned-fixed-angle bridges may be converted to pinned-pinned bridges by doubling length and volume while holding pressure constant. For example, Figures 5.4a and 5.15b show pV diagrams for a pinned-fixed-angle bridge with $\ell = 0.5$ and a pinned-pinned bridge with $\ell = 1.0$, respectively. These diagrams reflect that the families have the same pressures p_b while the pinned-pinned bridge has twice the volume.

For a pinned-pinned bridge, the bridge-droplet model may be formulated as in

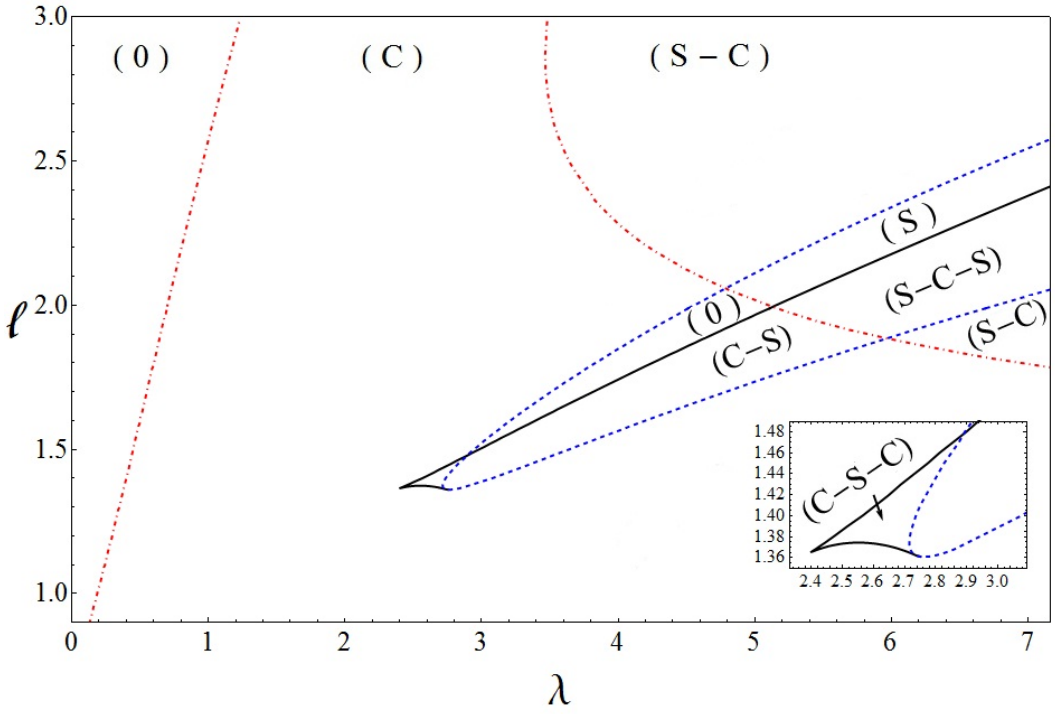

Figure 5.17: Two parameter bifurcation diagram for the bridge-droplet system with a pinned-pinned bridge. Each region is categorized by its types of equilibria, ordered by increasing bridge volume. Centers are labeled C and saddle points S.

Section 5.2.1. Using the same notation and recognizing that center of mass (for a pinned-pinned bridge) is fixed at $z_b = L + \ell/2$, the center-of-mass equation is

$$\frac{d}{dt}\left(\left[\frac{2}{3}H + 2L + \frac{1}{2}\ell\right]\dot{V}_b\right) = \frac{3}{4}\left(\frac{2}{R} - p_b\right). \tag{5.9}$$

This system is in equilibrium when bridge and droplet have equal capillary pressure. Bifurcation diagrams for various bridge lengths are shown in Figure 5.16. As bridge length increases, two equilibria curves exchange branches via a cusp bifurcation. As λ increases, the bifurcation diagram progression is similar to the pinned-fixed-angle case, the primary difference being the turnover of the lower

curve of equilibria prior to the cusp bifurcation; this results in a second saddle-node bifurcation (e.g. Figure 5.16B). In this case, as λ increases, the number of equilibria goes from 1 – 3 – 1 – 3 – 2 – 1. This progression can also be observed in the two parameter bifurcation diagram (Figure 5.17).

In the two parameter bifurcation diagram (λ, ℓ), three types of bifurcation curves exist: saddle-node (solid line), boundary equilibrium for $V_b = V^+$ (dashed line), and boundary equilibrium for $V_b = V^-$ (dot-dashed line). These curves separate parameter space into 9 regions, each with zero, one, two, or three equilibria. The equlibria are centers (C) and saddle-points (S) and are ordered by increasing bridge volume.

CHAPTER 6

BEETLE-INSPIRED ADHESION BY CAPILLARY-BRIDGE ARRAYS: PULL-OFF DETACHMENT[1]

This chapter represents a collaboration with contributions from Michael J. Vogel, Ashley M. Macner and Paul H. Steen. The SECAD design, development and construction was by MJV with guidance from PHS. PHS contributed Section 6.4 on hard- and soft-loading. The model for prying detachment (Section 6.5) originated with MJV. AMM contributed the measurements of the pinned-pinned liquid bridge (Figure 6.6). PHS guided the overall paper content and writing.

Abstract

Adhesion by capillarity ('wet' adhesion) depends on the surface tension of an array of many small liquid bridges acting in parallel against a substrate. A particular leaf beetle has been previously shown to defend itself using wet adhesion, and a man-made device, inspired by this beetle, has previously been demonstrated to exhibit electronically-controlled switchable wet adhesion. In both cases, measurements of detachment under load have been reported as pull-off strengths. In this paper, we pose models for pull-off adhesive failure and discuss the predictions of these models in relationship to available observations. The focus is on the role of array geometry and how net adhesive failure relates to the instability of a single liquid bridge.

[1]D.M. Slater, M. J. Vogel, A. M. Macner, P. H. Steen, *Beetle-inspired ahdesion by capillary-bridge arrays: pull-off detachment,* Journal of Adhesion Science, To Appear (2011).

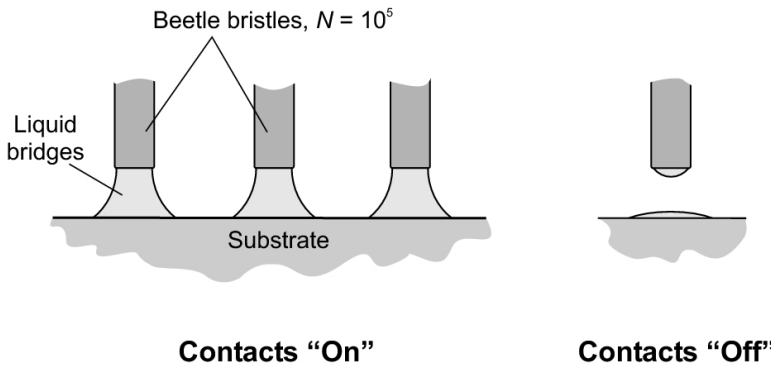

Figure 6.1: Capillary bridge array adhesion: idealized arrangement of liquid contacts between beetle tarsal bristles and substrate.

6.1 Introduction

Hemisphaerota Cyanea, a beetle native to the southeastern United States, exhibits extra-ordinary adhesion in defending itself by 'hunkering down' to its preferred substrate, the palm leaf (*serenoa* frond), with an adhesive strength of up to 100 times its body weight [9, 65]. Surface tension of a single liquid droplet contact of micron scale, amplified by parallel action of 120,000 contacts, is responsible (figure 6.1). A small drop of oil [10] is positioned at the tip of each bristle on the beetle's tarsi, which we will refer to as 'feet' henceforth. Each of these contacts can be thought of as a switch that is 'on' for adhesive contact or 'off' for no-contact. The beetle reconfigures the array in less than a second, switching 120,000 contacts 'on' or 'off'. Although nature abounds with other creatures who use both wet [66, 67, 68, 69, 70] and dry [71, 72] adhesion strategies, the beetle demonstrates the remarkable combination of strength and reversibility.

A 'switchable electroosmotic capillary adhesion device' (SECAD), inspired by *H. Cyanea*, has recently been demonstrated[2]. The SECAD is like the beetle in its strategy of parallel action and its ability to quickly switch on/off a vast array

of small liquid contacts, though the overall device structure and switching control differs from the beetle. The SECAD is a credit-card-thin rigid plate that uses a sub-second low-power voltage pulse to drive electroosmostic flow [11] within the device to push out or pull in small droplets, thus making or breaking contacts between the device and a substrate. It is estimated that a one square centimeter device with micron-sized contacts can adhere to a substrate against a 1 kg mass, while enjoying the benefits of electronically-controlled reversibility in a device made of common materials and with no moving parts.

The maximum adhesion of both SECAD and beetle scale with number of contacts N and surface tension σ. Maximum adhesion can also be expected to depend on the yield force of a single liquid bridge. For an axisymmetric bridge, the force on any cross-section f_b has two contributions, one proportional to perimeter and the other to sectional area. For a liquid/substrate contact of diameter ϵ, these contributions take the form

$$f_b = \pi\epsilon\ \sigma sin\alpha_0 - (\pi\epsilon^2/4)\ \sigma\kappa. \tag{6.1}$$

Here α_0 is the contact-angle and κ is the sum of the principal curvatures, a property of the shape. It is convenient to refer to these two terms as the 'perimeter' and 'shape' contributions to the adhesive force. The perimeter contribution always pulls the substrate upward - it is always adhesive - while the shape contribution can pull or push depending on the shape.

To emphasize the difference between perimeter and shape adhesion, consider the commonplace experience of trying to pull apart two glass plates which have a droplet of water trapped between them. The pull of surface tension is especially strong if the scale of the contact-line radius is large relative to that of the separation of the plates. In this case, the pull is due to the shape contribution since the mean

curvature (negative) scales inversely with the plate separation. That is, shape dominates perimeter in f_b. In contrast, the bridges controlled in the SECAD have lengths comparable to their diameters, in which case the perimeter force can dominate. This can be demonstrated for the SECAD, as reviewed in section 6.2. To the extent that it is true for the beetle has not been established, even though a perimeter-packing explanation has often been invoked [73, 74, 2].

There are a number of complications involved with modeling beetle pull-off detachment measured *in vivo*. The force of adhesion must be transmitted through the beetle exoskeleton, perhaps through 'muscles', through the array of liquid bridges and finally to the substrate. Videos of the beetle being attacked by the enemy ant suggest a real-time feedback control system that the beetle uses to maintain its hunkered-down position [75]. In summary, a detailed understanding of beetle pull-off detachment likely involves many influences that are challenging to identify and quantify.

The goal of this paper is to bring into focus some of these issues, especially regarding the mechanics of pull-off detachment. We do this by posing and solving some simple models for pull-off detachment under different loading scenarios and comparing the predictions against available measurements on the beetle. A secondary goal is to improve the design of the SECAD [2]. The main premise of this paper is that adhesive failure, for both SECAD and beetle, ultimately involves breaking of liquid bridges. And, to the extent that the breaking of a single bridge is the result of instability, failure will be mediated by single-bridge instability.

We first discuss the benefit of contact perimeter-packing in section 6.2, followed by a discussion of the response of a single liquid bridge and its stability in section 6.3. The loading scenarios that lead to pull-off detachment are specified

in section 6.4, followed by one-dimensional and two-dimensional models in sections 6.5 and 6.6. A discussion of the results and suggestions for further study can be found in section 6.7.

6.2 Perimeter-packing adhesion: SECAD

In perimeter-based estimates of beetle adhesion ('nominal' capacity), a static, uniform array of liquid contacts is assumed and the perimeter contributions of the wetted contacts are summed to estimate the net force. This simplified analysis is consistent with laboratory measurements [9]. The beetle deploys $N \approx 10^5$ oil contacts of $\epsilon \approx 2$ μm, with greatest measured capacity $F_\sigma/g \approx 3$ g where g is the acceleration of gravity.

To see the advantage that perimeter-packing conveys on the beetle, consider that beetle 'feet' project a total net area (i.e., including dry area between contacts) of $A_{net} \approx 2$ mm^2. The net perimeter force is $F_p = N\sigma\pi\epsilon \sin\alpha$. By introducing a contact packing density $\phi \equiv N\pi\epsilon^2/4A_{net}$, we find how adhesive force scales with contact size. Using ϕ to eliminate N yields the nominal scaled force for capillary bridge arrays as

$$\frac{F_p}{A_{net}} = \frac{4\phi\sigma \sin\alpha}{\epsilon}, \tag{6.2}$$

showing that $F_p \propto 1/\epsilon$ for fixed A_{net}. The benefit of packing a large number of small contacts into a fixed net area is evident from the amplification of adhesive force with $1/\epsilon$.

Amplification of the adhesion force as the inverse of liquid contact size has been demonstrated by the SECAD shown in figure 2A [2]. For our purposes,

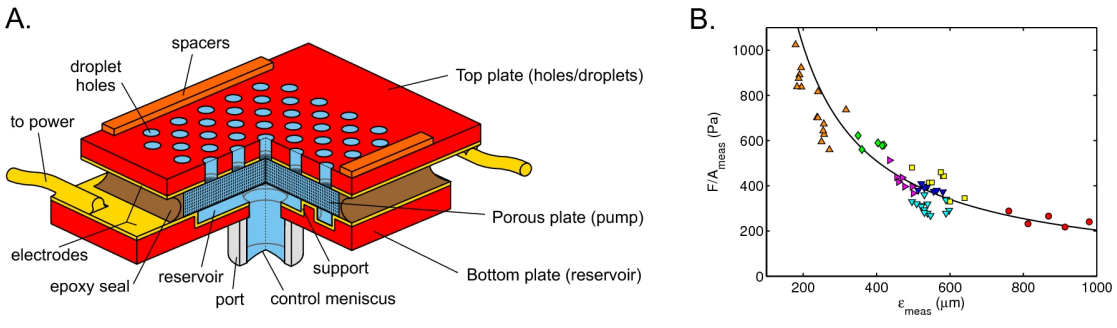

Figure 6.2: Switchable Electronically-Controlled Capillary Adhesion Device (SECAD), schematic and scaling of adhesion strength. (A) Main components in cutaway (not to scale for clarity). Primary layers are labeled to the right. (B) Adhesion strength F/A_{meas} versus contact size ϵ_{meas} , using normalized values. Solid line corresponds to model given in Eq. 6.2. Figures are adapted from [2]; see reference for details.

important features of the SECAD are number and size of the droplet holes, and the spacer which plays a role in preventing coalescence of contacts. The data in figure 2B represents a series of adhesive force measurements of the SECAD taken with a force transducer centered over the capillary bridge array ('pulling'). For the experiments, liquid bridges were all internally connected to each other and to atmospheric pressure, suggesting that bridge shapes were pieces of catenoids ($\kappa = 0$). The adhesion strengths in figure 6.2B therefore correspond to nominal values of adhesive force, and compare favorably to the simple scaling argument. The data represent a variety of experimental conditions: device fabrication methods include photolithography as well as traditional machining; contact diameters range from 150 μm to 900 μm, with N ranging from 100 to almost 5000; bridge length, hole packing density, and other parameters are also varied (see [2] for details). Despite these variations, the scaled adhesion strength agrees well with the nominal adhesion strength model.

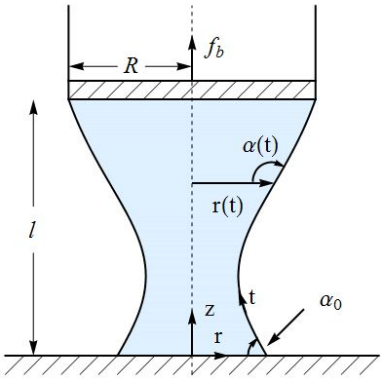

Figure 6.3: Single liquid bridge definition sketch.

Although measured adhesion capacity is modest for initial testing of SECADs, as contact size is scaled down to the micron range, predicted adhesion strengths approach those of synthetic bio-inspired tapes or commercial adhesives, with the advantage of controlled grab/release.

6.3 Single bridge force-length response

Capillarity-based or 'wet' adhesion relies on the force f_b transmitted by a single liquid bridge (figure 6.3). We model the contact with the beetle foot at top as pinned and with the substrate at bottom as making a fixed wetting-angle α_0. At equilibrium, the force on every axial section is the same, so one may evaluate on any section, at one's convenience. In terms of section radius r and the angle α, the angle the surface-tangent makes to the horizontal, measured through the liquid, the force is

$$f_b = 2\pi r\ \sigma sin\alpha - \pi r^2\ \sigma\kappa. \tag{6.3}$$

In the absence of distortion by gravity, static liquid bridges are shapes of constant mean-curvature ($\kappa/2$ =const). That is, κ is independent of z so that, in equation 6.3, only r and α vary with z. This means that the split between perimeter and shape contributions to f_b depends on axial position. Hence, for a fair comparison of shape and perimeter contributions between different bridges, a convention on an axial position is needed, say $z = 0$. This has been implicit in our discussion above. Note that, since $\epsilon = 2r(0)$ and $\alpha(0) = \alpha_0$, putting $z = 0$ in equation 6.3 recovers equation 6.1.

6.3.1 Equilibrium shapes

The mechanical response of a single liquid bridge is obtained by solving the local Young-Lapace equation, $p = \sigma\kappa$, for the bridge equilibrium shape. It is convenient to use arclength-angle coordinates (t, α) as defined in the definition sketch of figure 6.3. In what follows, f_b is scaled by σR, length l by R and volume V by R^3 where R is the bristle radius. We shall retain the notation f_b and l for scaled quantities. The scaled Young-Laplace equation takes the form of a two-point boundary-value problem,

$$d\alpha/dt = \sin\alpha/r - p, \quad \alpha(0) = \alpha_0 \tag{6.4a}$$

$$dr/dt = -\cos\alpha, \qquad r(s) = R \tag{6.4b}$$

$$dz/dt = \sin\alpha, \qquad z(0) = 0. \tag{6.4c}$$

Here s is the total arclength, defined by the condition $l = \int_0^s z'dt$. The solution $(r(t), \alpha(t))$ – note that the z equation decouples – is subject to the constraint of constant bridge-volume $V = \pi \int_0^s r^2 z'dt$ and is a standard calculation [13]. The plot of f_b against length l, shown in figure 6.4, is referred to as the force-length (FL)

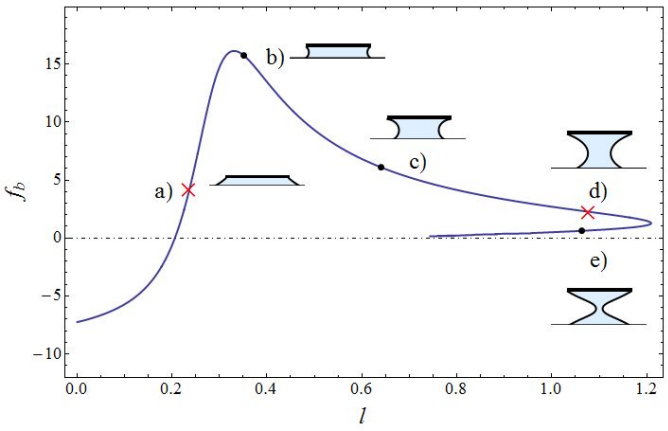

Figure 6.4: FL- response diagram for single bridge ($\alpha_0 = 30°$ and $V = 1.00$). Insets show corresponding shapes. Catenoidal shapes ($\kappa = 0$) are marked with an 'X'.

response. The pressure-volume (pV) response is more commonly encountered [14]. Alternatively, the FV response is sometime reported [76]. Note that equation 6.3 can be obtained as a first-integral of the system equation 6.4a [6].

In the bridge response, figure 6.4, negative force corresponds to a net push. Note that this only occurs for very short bridges ($l < 0.21$) where the shapes are sufficiently less slender than the catenoidal shape a), defined by $\kappa = 0$. For these shapes to the left of a), the push of the shape overcomes the pull of the perimeter. Between the catenoid shapes a) and d) the shape acts in concert with the perimeter pull. The maximum in net force f_b at about $l = 0.265$ results from a maximum in shape pull which dominates the change in perimeter pull that decreases monotonically from a) to d) due to a decreasing contact-radius.

For the beetle, the typical volume of oil deployed on a single foot can be estimated based on photos of 'footprints' left behind[9], although considerable variability might be expected. The value $V = 1.00$ corresponds to about one-quarter of a spherical-volume based on the bristle radius R. For the SECAD, a broader

range of volumes is relevant, as these are controlled.

The FL-response of figure 6.4 varies with volume as seen in figure 6.5a. On decreasing volume from $V = 1.5$, the shapes become more curvaceous and the shape-pull maximum increases, and shifts to lower l, resulting in an increase in the force maximum. In contrast, the length-maximum decreases. The length maximum is akin to a Plateau-Rayleigh instability[77, 19] and corresponds to a volume turning-point in a pV-response (not shown, but summarized by the VL stability envelope [6]), the context in which it is most easily understood.

For the SECAD, contact-angles near neutral-wetting, $\alpha_0 = 90°$, are relevant while, for the beetle, angles closer to complete wetting are of interest, $\alpha_0 < 30°$. Figure 6.5b shows, for contact-angles away from complete-wetting, $\alpha_0 > 30°$, that both force and length maxima decrease with increasing contact-angle. For contact-angles near complete-wetting, $\alpha_0 < 30°$, figure 6.5c shows that the force maxima decreases, as near neutral-wetting, yet the length maximum increases with increasing contact-angle. These plots indicate the sensitivity of the turning points to the parameters.

6.3.2 Stability and turning points

The force and length maxima are the key features of the FL-responses. As is well-known from the behavior of elastic materials, such maxima in a stress-strain response are responsible for instabilities when the body is loaded [78]. For an extension experiment under controlled strain (hard-loading), the maximum in l will cause instability. In contrast, under controlled stress (soft-loading), the maximum in f_b causes instability. The very different behaviors that occur under these dif-

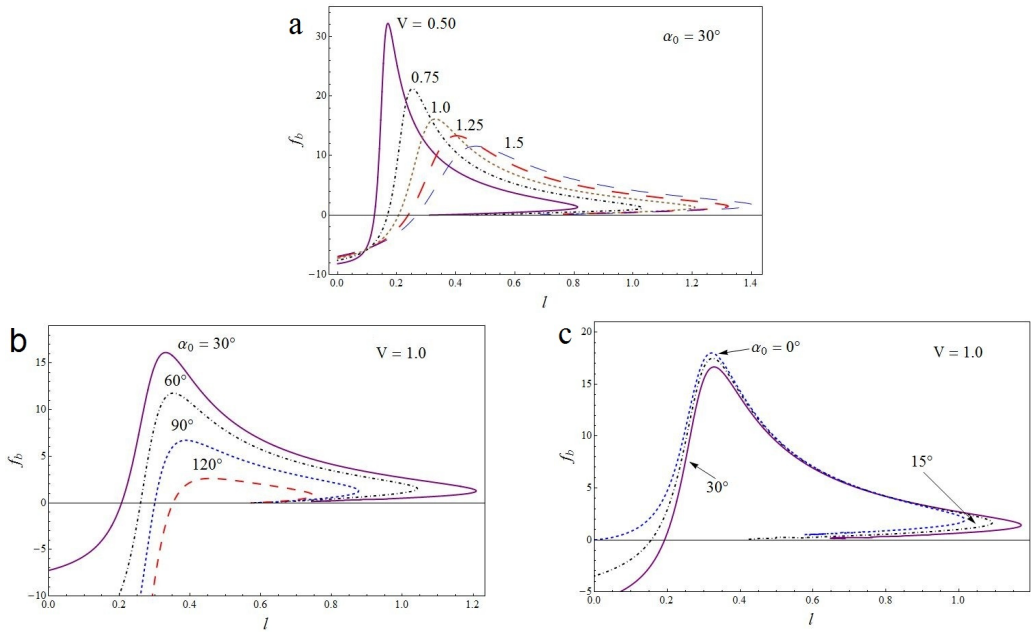

Figure 6.5: FL-response diagrams. Variation in a) volume for $\alpha_0 = 30°$ and contact-angle for $V = 1.0$ for b) $\alpha_0 > 30°$ and c) $\alpha_0 < 30°$.

ferent loading conditions are well-documented [79]. For liquid bridges, analogous instabilities occur at turning points in pressure and volume in the pV response [14]. The bridge breaks as a result of these instabilities [15]. The predictive theory of instability based on turning points in a response diagram finds application broadly [80] and has a long history that can be traced back to Poincaré [81]. That different loading scenarios lead to different instabilities is because of the different class of disturbances that are admissible under the different loading constraints. In summary, on increasing the load under soft-loading conditions, the bridge goes unstable at the maximum in f_b. Alternatively, while increasing the extension, under hard-loading, the bridge will reach longer lengths and go unstable at the maximum in l. For the conditions of figure 6.4, for the two different scenarios, this means an eleven-fold difference in 'yield stress' and a nearly four-fold difference in 'yield length.'

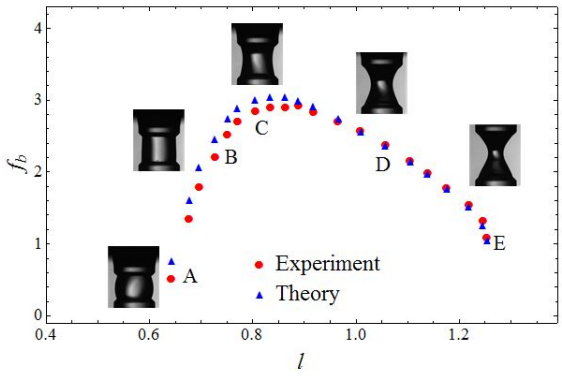

Figure 6.6: Experimental FL-response for a pinned-pinned water bridge under hard-loading, starting at A and increasing l to E, where the bridge breaks. Insets are photos of corresponding bridges. $2R = 2.8mm$; $1.7 < V < 2.3$ (experimental work of AM Macner)

To illustrate the predictive ability of the response diagram, figure 6.6 shows measurements from our laboratory of a single pinned-pinned water bridge subject to hard-loading. The experiment begins at left, photo A, and proceeds by quasi-statically increasing the length until the bridge breaks at photo E. Lengths (along with volumes and shapes) of the bridges are extracted from the images and force is measured by a digital balance (AND HR-200). These are the data labeled as 'experiment.' Because of the small scale of the bridge (R = 1.4 mm), there is evaporation, and the volumes vary considerably over the duration of the experiment (from 6.5 to 4.8 μl). There is also a detectable influence of gravity on the shapes. For these reasons, the model takes account of volume variation and shape-deflection by gravity and hence is plotted as symbols rather than a curve. Finally, for convenience in comparing to the previous response diagrams, we have reported l as half-length (and V as half-volume), since a pinned-pinned experiment, at least in theory, gives a force corresponding to that of a half-bridge that has contact-angle 90° at the mid-plane, based on its symmetry about the mid-plane. The point of this figure is to illustrate the extent of agreement between experiment and theory

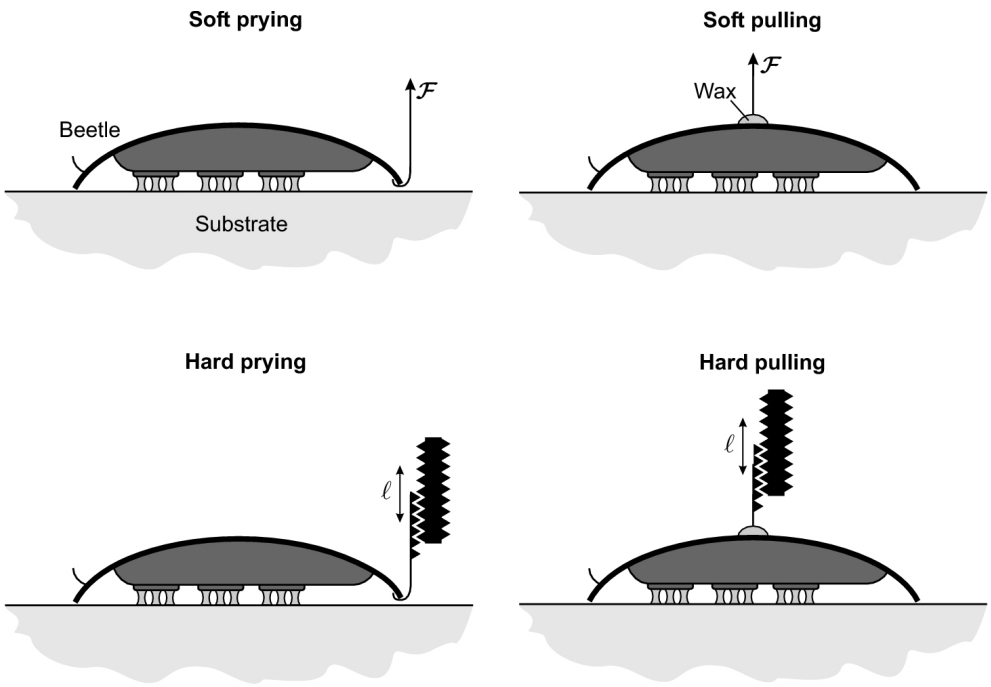

Figure 6.7: Detachment mechanisms.

for a hard-loaded single bridge.

6.4 Scenarios for pull-off loading

Beetle detachment can be voluntary or involuntary. Voluntary detachment is believed to proceed by a 'divide and conquer' strategy. The beetle peels off contact-by-contact (or row-by-row) using a rolling action [9]. However, involuntary detachment, or prevention thereof, is equally important to the beetle's survival. We shall limit our scope to involuntary detachment, in part, because measurements exist only for this case [9]. We consider various loading configurations, explained in the following paragraphs and illustrated in figure 6.7.

In the laboratory [9], detachment under duress occurs by pulling from the center

of the beetle's shell via dental wax. In the actual measurements, the substrate is pulled down while the beetle is attached above to a force transducer[65]. The beetle's resisting normal force is recorded as a function of time on an oscilloscope display. We refer to this as the 'pulling' detachment.

In nature, attacking ants try to pry up the shell of the hunkered-down beetle in order to render it defenseless and carry it back to the ant colony for processing [75]. Hence, the ant applies a force at the shell edge, creating a moment about the pivot at the opposite edge. This is what we call the 'prying' detachment location.

As described earlier, we shall further distinguish between 'hard-' and 'soft-loading' in the sense used in solid mechanics when describing the stress-strain response and yield of elastic materials. That is, in hard-loading, a displacement is controlled whereas, in soft-loading, the force is controlled. In summary, pull-off by pulling and prying under soft- and hard-loading will be modeled. For purposes of definiteness, the reader should think of these as arising from different single-bridge stability limits discussed in Section 6.3, although it is possible to relate these to physical models of beetle anatomical control.

6.5 1-D Pad Modeling

There are many differences between the beetle and a man-made adhesion device. For this study, we utilize an idealized adhesion pad that lies between the two. In particular, we consider the adhesion pad (including the beetle's shell, body, feet, etc.) to be perfectly rigid; the liquid bridge contacts are isolated from one another (i.e., scavenging time in the SECAD are long relative to detachment dynamics timescale [16]); the liquid bridges have fixed volumes, fixed contact angles at bot-

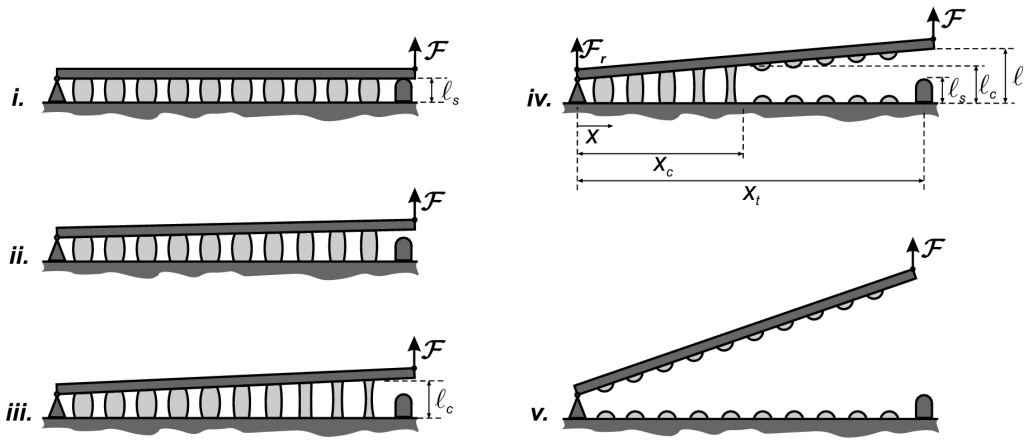

Figure 6.8: Capillary-bridge linear array model; detachment by prying. As right side is pulled up against left-side pivot, bridges are stretched and eventually break.

tom, pinned contact lines at top, and constant surface tension; and the dynamics are quasi-static.

While the beetle's nominal (static, perimeter-based) adhesive force provides an estimate of capacity, we are interested in modeling the dynamics of detachment. For the case of 'pulling' detachment, we assume the beetle and substrate remain parallel. The liquid bridges therefore change shape in unison, and the dynamic behavior can be readily computed from the single-bridge response diagram up to the transition to instability when the bridges break. But for 'prying' detachment, the bridges are stretched at non-uniform rates. One would expect the adhesion strength to increase initially as the bridges are stretched, according to the response diagram. Subsequently the bridges begin to break, starting at the higher prying edge.

Figure 6.8 shows this 'prying' detachment for a one-dimensional array of capillary bridge adhesion. A plate of length x_t pivots about a hinge and in the absence of duress is held a distance ℓ_s from the substrate by solid spacers on right and left

(rest state, sketch i). Note that solid spacers are used in the SECAD; the shell may play a role as spacer/pivot for the beetle. Adhesion occurs by a number N liquid droplets that bridge between the plate and substrate. Under duress, an applied force $\mathcal{F}$ or height ℓ is increased and nearby bridges lengthen (sketch *ii-iii*). Once a bridge's length exceeds a critical length ℓ_c, the bridge breaks and its contribution to the net attachment force is lost (sketch *iv*). Full detachment corresponds to all bridges being broken (sketch *v*). Note that figure 6.8 is not drawn to a scale consistent with beetle or SECAD adhesion. In the computations, we assume the angle between the plate and substrate is always small, so that bridges remain axisymmetric.

Suppose a plate with pad length x_t has been pried until the height of the prying point is a distance ℓ above the substrate. Then the height of the pad $H(x, \ell)$ at position x is given implicitly by $x_t(H(x, \ell) - \ell_s) = x(\ell - \ell_s)$, via similar triangles.

Bridges become unstable and break at the critical bridge length ℓ_c corresponding to the length turning point for hard-loading and the force turning point for soft-loading from the single bridge FL diagram (figure 6.4), respectively. The critical length occurs at $x = x_c$, where

$$x_c = \begin{cases} x_t & \text{if } \ell \leq \ell_c \\ x_t * \frac{\ell_c - \ell_s}{\ell - \ell_s} & \text{if } \ell > \ell_c. \end{cases} \tag{6.5}$$

Note that we consider bridges to break instantly and the dynamics of the break-up process are not considered in the present quasi-static model.

Let F_σ be the equivalent force of all the bridges applied at the centroid x_σ. Then if $x = 0$ corresponds to the pivot point, ϕ the bridge packing, and $\overline{F}$ the

average force of all the bridges, then

$$F_\sigma(\ell) = \sum_{i=1}^{N} (f_b)_i = (\phi x_c)\overline{F} = \phi \int_0^{x_c} f_b(H(x,\ell))dx. \tag{6.6}$$

Here we assume a continuum smearing of the bridges ($N \to \infty$ as $\epsilon \to 0$). The centroid is located at

$$x_\sigma(\ell) = \frac{1}{x_c \overline{F}} \int_0^{x_c} s f_b(H(s,\ell)dx. \tag{6.7}$$

A simple balance of forces relates the applied force $\mathcal{F}$ with F_σ and x_σ:

$$\mathcal{F}(\ell) = F_\sigma \frac{x_\sigma}{x_t} = \phi \int_0^{x_c} f_b(H(s,\ell))ds. \tag{6.8}$$

This expression for 'prying' can be contrasted with 'pulling' hard- and soft-loading where $\mathcal{F}_{pull}(l)$ is

$$\mathcal{F}_{pull}(\ell) = \phi x_t f_b(\ell) \quad \text{for} \quad \ell \leq \ell_c. \tag{6.9}$$

That is, since all bridges act in unison, the total force in pulling is proportional to the single-bridge response curve.

It should be noted that the perimeter-packing scaling $\mathcal{F} \propto 1/\epsilon$ is masked by the nondimensionalization of the equations. For the two-dimensional case (discussed in the next section), the force and area are scaled by factors of ϵ and ϵ^2, respectively, resulting in the expected $1/\epsilon$ dependence. However, in the one-dimensional case (one row of bridges) there is no benefit to adhesion strength in scaling down ϵ.

The model computations are shown as pseudo-dynamic traces of the force applied at the pulling point over time. The dependence on time is meant as a loose interpretation of what one might observe in a real experiment. Specifically, we show the force increasing linearly with time from $t = 0$ to 0.2 (a pre-loading period

where the reaction force due to the right spacer is transferred to the pulling mechanism), and then l increases linearly with time for $t > 0.2$ (so force is controlled in such a way that yields linear increase in l over time). Also, we use a value of $\phi = 1$ for convenience in the computations despite a theoretical maximum value of $\phi = 0.907$ for a hexagonal packing arrangement. A value of $x_t = 10$ is used in the calculations. Note that in all detachment scenarios $\mathcal{F}$ scales linearly with x_t.

Computations of release dynamics presented here are for single values of initial spacer length ℓ_s, bridge volume V, and contact angle α_0. Since FL response diagrams are qualitatively similar (figure 6.5), we expect the release dynamics to also be qualitatively similar for different values of V and α_0. For the computations we have chosen a value of $V = 1$ based on beetle footprints and $\alpha_0 = 30^\circ$ as a representative value between the beetle and SECAD cases. Also, since the FL curves are essentially linear in the starting region (the region of greatest influence), we don't expect significant changes in the curves as ℓ_s is varied from the presently-used value $\ell_s = 0.21$.

The force versus time system response for the one-dimensional model are shown in figure 6.9 for the four detachment mechanisms. The two pulling-release curves are identical up to the peak in force ($t = 0.33$), but the pulling-soft-loading curve exhibits an immediate drop to zero as all the bridges break at the force turning point. The pulling-hard-loading curve gradually falls to a lower value of force that corresponds to the length-turning point in the response diagram where all bridges uniformly break and the force then abruptly drops to zero ($t = 1.2$).

The two 'prying'-release curves are also identical at early time. The magnitude of $\mathcal{F}$ is roughly half of that for 'pulling'-release due to the reaction at the pivot. Soft- versus hard-loading is similar to those of the pulling curves, except for general

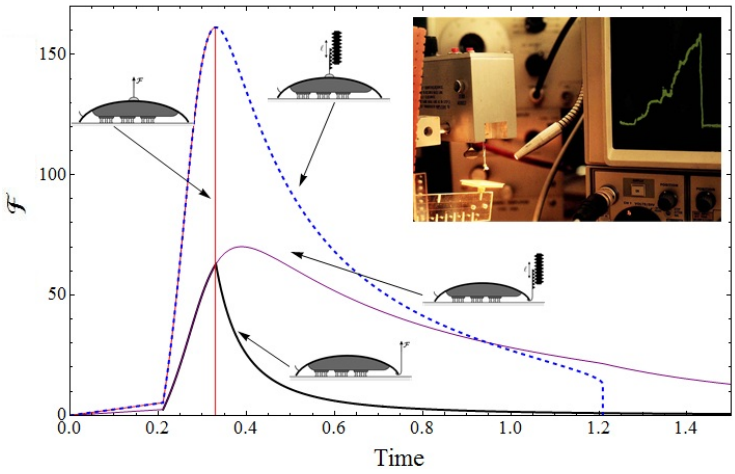

Figure 6.9: One-dimensional release dynamics for several detachment mechanisms. Inset shows experimental trace of force over time (oscilloscope) for soft-pulling experiment with beetle. Inset reproduced with permission from Thomas Eisner and Daniel Aneshansley, Cornell University.

smoothing of the curves due to the bridges not being stretched uniformly. So the prying-soft-loading curve begins to fall before the peak since the right-most bridges begin to break earlier (c.f. figure 6.8 *iii*), and the drop in $\mathcal{F}$ is more gradual as the plate is pried up. Both prying curves asymptote to zero due to the assumption of a continuum of bridges. As we assume the bridge diameter ϵ is small relative to the pad width, the angle remains small until a negligible number of bridges remain.

The curve for pulling-soft-loading (figure 6.9, thick red) should be compared to the oscilloscope trace in figure 6.9, inset, which is reproduced from the work of Eisner and Aneshansley [9]. The curves demonstrate sensitivity of the model to soft- and hard-loading protocols but, most importantly, note the remarkable qualitative resemblance of the prediction to the measurement, suggesting that the model has captured key features of the physics, despite its simplicity.

6.6 2-D Pad Modeling

The active adhesion area of the beetle is limited to the six feet, which total only about 10% of the beetle's body area. Further, these feet are spread asymmetrically about the beetle's body, with a centroid closer to the beetle's 'head'. The 1D model can be extended to two dimensions where one must also consider the beetle geometry. Here, we focus on prying-release, and for simplicity we assume the two dimensional beetle is pulled uniformly from one side so it rises like a rigid hinge.

Let $y(x)$ be the width of the beetle at position x. Then the equivalent force of all the bridges F_σ and the centroid are simply:

$$F_\sigma = N * \overline{F} = \phi \left(\int_0^{x_c} y(s)ds \right) \overline{F} = \phi A \overline{F} \tag{6.10}$$

$$x_\sigma = \frac{\int_0^{x_c} s f_b(H(s,\ell))y(s)ds}{\int_0^{x_c} f_b(H(s,\ell))y(s)ds} = \frac{1}{\overline{F}A} \int_0^{x_c} s f(H(s,\ell))y(s)ds, \tag{6.11}$$

where A is total area connected. The applied force is then

$$\mathcal{F}(l) = F_\sigma \frac{x_\sigma}{x_t} = \phi A \overline{F} * \frac{1}{\overline{F}Ax_t} \int_0^{x_c} f_b(H(s,l))y(s)ds \tag{6.12}$$

$$= \frac{\phi}{x_t} \int_0^{x_c} s f_b(H(s,l))y(s)ds. \tag{6.13}$$

Note that if $y(x) =$ constant this reduces to the 1D model, scaled by fixed width. In this way one can think of the 1D model as corresponding to a square beetle.

The beetle may be modeled by treating it as an ellipse with aspect ratio 5:4. It has six round feet as shown in figure 6.10, inset, that are closer to the head than the tail. Of particular interest is the applied force required to pry the beetle at its head, tail and one of its sides. This is shown in figure 6.10, where the three curves are scaled by the prying force peak for a beetle with the same number of

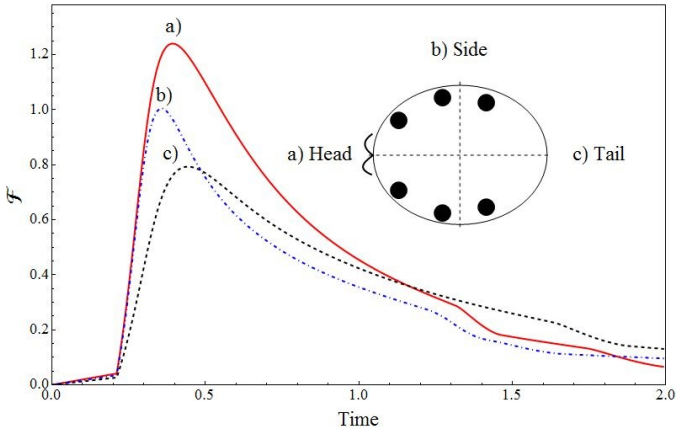

Figure 6.10: Release dyanmics for prying-hard-loading from prying positions a), b) and c). Results are scaled by the force peak for a beetle with a uniform distribution of contacts.

contacts uniformly distributed over its body. Here we see that prying the beetle from the side is roughly the same as the force required to remove the beetle if it had contacts uniformly distributed. Furthermore, it requires roughly 1.5 times the force to pry the beetle from its head versus its tail. The results suggest that the beetle is most vulnerable when the ant pries from the rear, where leverage is the greatest. Because the beetle sets down a defense, it cannot turn to fact the ant. That is, the ant is mobile but the beetle is not.

In terms of designing a capillary adhesion device we can use the beetle as a guide. The beetle is weaker from the tail because it has fewer connections near that side. If one is optimizing a device we would like to eliminate any potential weak points. To do so one should maximize symmetry of contact distribution. As it turns out, circular and square symmetry are virtually identical in their adhesion strength (including pulling a square from a corner). In figure 6.11 the applied force for any of these 'symmetric' configurations is compared with placing all contacts near the prying or the pivot point (fixed N, adjusting ϕ as necessary). The force

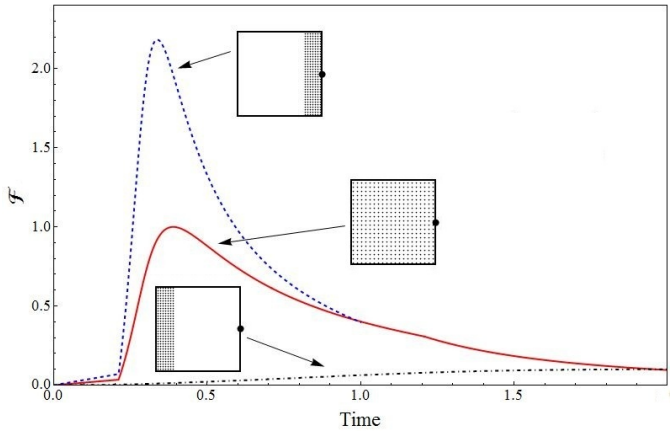

Figure 6.11: Release dynamics for a hard-loaded square SECAD device being pryed from one side (black dot). The dashed and dot-dashed curves are for a device with all its contacts on one side while the thick curve is for a device with its contacts uniformly distributed (same N for all curves). Results are scaled by the force peak of the uniformly distributed case.

peak of the uniform-distribution case is about half that of the prying case where bridges are packed in at the prying edge. However, when the bridges are all located at the pivot edge, very little force is required to remove the device. Furthermore, bridge distribution in the symmetric case has little effect on the applied force. That is, positioning bridges uniformly around all four edges with a bridge-free region in the center gives an essentially identical response to the uniform-distribution case. This could be useful from a fabrication perspective if, say, some region of the SECAD had to be void of contacts in order to serve some purpose such as device assembly.

6.7 Discussion

Both the beetle and the SECAD use parallel action of a large number N of liquid bridges to amplify the adhesive force due to surface tension σ of a single bridge. For the beetle, $\sigma \sim 30$ mN/m, appropriate for an oil with a composition close to the beetle's tarsal oil (in-house measurement), while for the SECAD, $\sigma \sim 55$ mN/m, appropriate for water that has been in contact with plastic tubes and rubber syringes[2]. In the case of the beetle, the number N of deployed bridges and the scale ϵ of a typical contact must be estimated while, for the SECAD, N is counted and ϵ is measured. For the beetle, under the assumption of full deployment, $N \sim 120,000$, and based on $\mathcal{F} \sim N(2\pi\epsilon)\sigma$, an estimate of net adhesion strength matches the measurement to an order-of-magnitude.

For the SECAD, the more precise estimate of net adhesion strength, $\mathcal{F} = Nf_b$, can be tested, where f_b is given by equation 6.1. Contact diameter ϵ is varied six-fold down to $\epsilon = 150$ μm and number of bridges N is varied fifty-fold up to $N \sim 5000$. Moreover, for the SECAD bridges, there is significant control over the shape. This occurs by uniformly removing or adding water to all the bridges simultaneously using a non-scavenging electro-osmotic pump. By this means, bridges with $\kappa \approx 0$ are achieved, in which case, $\mathcal{F} \sim \sigma/\epsilon$ is observed, as anticipated, since $N\epsilon^2 \sim$ const over the range of variation. This amplification of adhesion occurs truly by 'perimeter-packing' since only the perimeter contributes to f_b when $\kappa \sim 0$, according to equation 6.1. Note that $\alpha_0 \approx 68^\circ$ for our water against a Plexiglas substrate[2].

Eisner and Aneshansley[9] test the beetle *in vivo* against four substrates. They observe a measurable decrease in strength from *serenoa* to glass to parafilm to aluminum. They point out that this decrease from maximum strength against

the beetle's natural substrate *serenoa* indicates that the beetle clings by adhesion. Accepting this, one may ask whether beetle adhesion is predominately by perimeter or shape effect. To try to answer this, we have obtained measurements of the wetting angle of the tarsal oil proxy against the four substrates[82] and find, ordered by decreasing wettability, $\alpha_0 < 5^\circ$ for *serenoa* and aluminum foil, $\alpha_0 \sim 10^\circ$ for glass and $\alpha_0 \sim 33^\circ$ for parafilm. According to single bridge theory, figure 6.5c, for a soft-loading failure, the f_b should decrease with decreasing wettability. This would order serenoa and aluminum as comparable in strengths with a decrease in strength to glass and a further decrease to parafilm. Hence, apart from aluminum, the order measured is consistent with the order predicted. Details of the experiments are not available, so it is difficult to explain the anomalous results for aluminum, though a number of explanations (aside from inaccurate data) are possible. For example, electrostatics in the electrically conducting foil could play some role, or perhaps there is some dynamic response not accounted for in our model. One may note that, to reconcile figure 6.5c with equation 6.1 in the limit of $\alpha_0 \to 0^\circ$, the wetted diameter $\epsilon \to \infty$, consistent with complete wetting [83]. In any case, it seems likely that the shape contribution plays some role in beetle adhesion. How the beetle exerts control over the shape, if any, though, remains an open question.

What is known is that, for detachment, the oil contacts must break. What is also known, from the mechanics of liquid bridges, is that bridges break owing to instability. Furthermore, different loading conditions give different constraints and different instabilities. Consequently, breaking occurs at force- or length-turning-points in the bridge's response diagram depending on soft- or hard-loading. As stability is a matter of bridge physics, independent of the beetle anatomy and control, one might expect to observe differences without detailed knowledge of the anatomy and control.

In this spirit, a simple 1D model of a linear array of bridges, along with two loading geometries and two instability hypotheses, has been posed. The idea is to predict the time-course of force during pull-off detachment. The predictions, summarized in figure 6.9, show four significantly different responses. Under pulling, the force at detachment for soft-loading is 11-fold greater than that for hard-loading and the time-to-failure is roughly 4-fold longer. Under prying, the force for soft-loading is 10% greater than for hard-loading and the time-to-failure is about 5-fold longer.

Pulling is the only loading geometry where quantitative results from experiment are available. Eisner and Aneshansley[9] provide a photo of the time-course, reproduced in the inset of figure 6.9. The precipitous fall in force in the photo should be compared to figure 6.9. The good qualitative match suggests a soft-loading failure. On this basis, one may speculate that the beetle is not controlling the length of bridges, in contrast to our lab experiment on a single bridge (cf. figure 6.6), but is mediating the force, probably through its muscles under stress for this pull off.

The data of Eisner and Aneshansley[9], in their figure 6 (right), can be rearranged to plot failure-load against time-to-failure. The shape of this plot is suggestive of soft-loading failures at high loads and hard-loading failures at low loads, but the difference in maximum loads is only about a factor of 3. Note that these *in vivo* experiments are done on glass. Whether or not there are scenarios in which beetle adhesion yields as under hard-loading conditions is an open question.

Our 1D model is then extended to a 2D model with the main goal of understanding how geometry influences pull-off failure. Regarding the beetle, we learn that it is in the ant's best interest to pry from the rear of the beetle, 'blind-siding

it,' so to speak. Regarding SECAD design, we learn that a high degree of symmetry is desirable to eliminate weak points, yet we have considerable freedom with design specifics. For example, a square array and a circular array with the same number of contacts have nearly identical force responses. This is useful when designing a SECAD device as any deviations from a circular device due to fabrication issues will have minimal impact.

A number of extensions to this work are possible. Incorporating elasticity in the adhesion plate model may provide insight and aid in design of devices. For the beetle, elasticity likely becomes important as the beetle fatigues. The SECAD plate may realize greater adhesion strength in real-world applications since better compliance to curved or rough substrates will increase the number of adhesive contacts made. A future study may involve optimization of the balance between perfectly rigid and perfectly compliant devices.

It also may be of interest in the future to incorporate a physiological time-dependent model of the beetle's fatigue. Muscular action is presumed an important part in keeping the feet rigid to remain hunkered down. By estimating the beetle's available energy versus the energy expended in remaining rigid, a model that predicts the time duration of adhesion may be possible, and this data could be compared to existing data of beetle endurance [9].

The present model considered isolated bridges of fixed volume. While this may be a reasonable approximation to the beetle, the SECAD can be operated in various modes, some of which differ from this approximation. Specifically, the liquid bridges are typically connected internally (in communication with each other through a reservoir), which implies that any change in the shape of one bridge can affect all other bridges (although the rate of this communication can be controlled).

Further, the SECAD is often operated under a fixed-pressure (atmospheric) constraint rather than fixed-volume. Modeling these different operational modes is beyond the scope of this paper but may be investigated in the future.

6.8 Concluding remarks

The strength of an array of liquid bridges is at the source of the remarkable adhesion exhibited by the leaf beetle and that of the man-made SECAD. For the beetle, there are upwards of $100,000$ bridges of a size on order of 2 μm, while for the SECAD the number of bridges varies from 100 to nearly 5000 of a size from 1000 down to 200 μm. To the extent that liquid bridge instability must mediate any net pull-off detachment (adhesive failure), one might expect to observe signatures of those instabilities in the force against time measurements. Pulling and prying models of adhesive failure for hard- and soft-loading assumptions do indeed show significantly different time-to-failure courses. For pulling, the time-to-failure follows the single bridge case and the sole difference between hard- and soft-loading is due to the difference between hard- and soft-loading in the single-bridge response. In contrast, for prying, the bridges break sequentially as each reaches its own critical force/length limit of instability. In this case, the arrangement of bridges can make a significant difference. A simple model of the arrangement of groups of beetle feet show that prying from at rear of the beetle is most dangerous to the beetle. A similar model for a SECAD pad suggests that failure under prying is relatively insensitive to bridge array pattern as long as the geometry is symmetric. This may allow welcome flexibility in fabrication. There are a few measurements available on the beetle and we interpret these in terms of the predictions. Pull-off by pulling on the beetle back is argued to be a soft-loading failure. A number of

extensions to this work may further elucidate the beetle's detachment as well as provide important design improvements in the SECAD.

Acknowledgements

The authors would like to thank Tom Eisner and Dan Aneshansley for kindly supplying the photo in figure 6.9 and for useful clarifications. Useful discussions with Henrik van Lengerich and Brenton Cox are acknowledged. This work was supported by NSF Grant CBET-0653831 and the Defense Advanced Research Planning Agency.

CHAPTER 7

FUTURE WORK

In this section, we discuss potential implications for further study. Broadening the area of research provides an avenue for development of complementary material. Hence, we are able to infer additional properties of capillary-surface oscillators and thus further the understanding of this class of problems.

One logical extension of the S_n model in Chapter 3 is to relax the strict symmetry assumption and consider consider other networks. As such, other networks of droplets may be examined. For example, when the assumption of symmetry is relaxed, droplets can be arranged in a ring while connected to their nearest neighbors; this would generate an n droplet model with D_n symmetry. Another extension would be to consider a flat plate that houses a rectangular array of droplets coupled via a central reservoir. Modeling such a system can be achieved by coupling all droplets and scaling the effect of droplet i on droplet j by physical distance. This model would be D_4-symmetric. In either of these studies, bifurcation and stability results can be obtained for the resulting system. Further, if the system has maintained some degree of symmetry, detectives can be utilized to determine the symmetries of trajectories.

In addition to considering different networks, analysis can be varied in terms of classification of trajectories. In chapter 4 the S_3 symmetric three droplet system is analyzed using symmetry detectives and Lyapunov exponents. The data from these methods can be compared with the results of other methods such as 'group averaging' of symbol sequences. Any trajectory can be represented as a sequence of symbols using symbolic dynamics in a number of ways. To clarify, each time the trajectory crosses a line of symmetry, a symbol is added to a sequence: 1 for

AA', 2 for BB', and 3 for CC' (see Figure 4.2). Such crossings occur when two of the three droplets have equal volume (e.g. AA' is crossed when droplets two and three have the same volume). In this manner, a trajectory can be represented as a sequence of 1's, 2's and 3's. Once trajectories are mapped to a symbol sequence, they can be analyzed in terms of group averages that characterize the degree of symmetry of the sequence.

As noted previously in this dissertation, forced oscillations are another source of interest. Networks of droplets may be weakly dampened and forced resulting in chaotic dynamics and strange attractors. The dynamics of such systems can be analyzed with techniques such as a higher order Melnikov method. Note that forcing a single droplet in an S_n symmetric network reduces overall symmetry and gives rise to S_{n-1} symmetry. Naturally, systems with four or more droplets are of particular interest because they retain nontrivial symmetries. The symmetries of the resulting strange attractors can be determined using symmetry detectives.

The most significant extensions evolve from the bridge-droplet switching system presented in Chapter 5. One of the more noteworthy avenues of exploration is to treat the system as a fast-slow dynamical system, in which the slow subsystem is the current model and the fast subsystem would model the system during transitions between states. Because the transitions remain non-smooth, the interaction between non-smoothness and multiple-time scales is of particular interest as it can lead to complicated and interesting behavior.

The bridge-droplet system can also be extended to accommodate larger networks of droplets and bridges. For example, the S_n droplet model in Chapter 3 can be modified to incorporate bridges by introducing substrates above each droplet (or a subset of droplets). Then, like the model presented in Chapter 6, droplets make

contact with substrates and form bridges. For large n, such systems can serve as a model for a dynamic adhesion pad, with the droplets and bridges coupled through tubes or a central reservoir.

Additional topics of interest for bridge-drop systems include time dependence and other families of bridges. Time dependent bridge-droplet systems can behave chaotically. For instance, suppose the substrate (or the plate) in the bridge-droplet system experiences regular vibrations. Now, if small dampening (due to viscous resistance) is included in the model, it can be analyzed using the methods from Chapter 2. Possible extensions to other families of bridges include different contact angles (corresponding to different types of substrates) and bridges pinned at both ends (continuation of Section 5.5.1 but allowing the radius at each end to vary). Observe that these systems are complicated since the volume of the system may change due to satellite droplets being left on the substrate.

Finally, in the realm of adhesion modeling, several areas of future work are possible. First, the addition of elasticity may prove insightful: with respect to the SECAD device, increased adhesion strength is possible via better compliance to curved or rough surfaces. One simple way to incorporate elasticity is to consider a series of hinged flat plates to approximate a curved surface. Furthermore, incorporating physiological time-dependence in the model would account for the beetle's fatigue. Such a model could be compared with existing data from experiments done on the beetle's endurance. Lastly, different bridge couplings should be considered (e.g. a model with volume flow between bridges).

BIBLIOGRAPHY

[1] Theisen, E. A., Vogel, M. J., Lopez, C. A., Hirsa, A. H. & Steen, P. H. Capillary dynamics of coupled spherical-cap droplets. *J. Fluid Mech.* **580**, 495–505 (2007).

[2] Vogel, M. J. & Steen, P. H. Capillarity-based switchable adhesion. *Proc. Natl. Acad. Sci. USA* **107**, 3377–3381 (2010).

[3] Finn, R. Capillary surface interfaces. *Noptices of the AMS* **46**, 770–781 (1999).

[4] Basaran, O. A. Small-scale free surface flows with breakup: Drop formulation and emerging applications. *AlChe Journal* **48**, 1942–1848 (2002).

[5] van Lengerich, H. B., Vogel, M. J. & Steen, P. H. Coarsening of capillary drops coupled by conduit networks. *Phys. Rev. E* **82**, 066312 (2010).

[6] Gillette, R. D. & Dyson, D. C. Stability of axisymmetric liquid-fluid interfaces towards general disturbances. *Chem. Eng. J.* **3**, 196–199 (1972).

[7] López, C. A. & Hirsa, A. H. Electrochemically activated adaptive liquid lens. *Appl. Phys. Lett.* **87**, 134102 (2005).

[8] López, C. A. & Hirsa, A. H. Fast focusing using a pinned-contact oscillating liquid lens. *Nature Photon.* **2**, 610–613 (2008).

[9] Eisner, T. & Aneshansley, D. J. Defense by foot adhesion in a beetle (*Hemisphaerota cyanea*). *Proc. Natl. Acad. Sci. USA* **97**, 6568–6573 (2000).

[10] Attygalle, A. B., Aneshansley, D. J., Meinwald, J. & Eisner, T. Defense by foot adhesion in a chrysomelid beetle (hemisphaerota cyanea): characterization of the adhesive oil. *Zoology* **103**, 1–6 (2000).

[11] Vogel, M. J., Ehrhard, P. & Steen, P. H. The electroosmotic droplet switch: Countering capillarity with electrokinetics. *Proc. Natl. Acad. Sci. USA* **102**, 11974–11979 (2005).

[12] Chen, L.-H. & Chang, H.-C. Equilibrium shapes of liquid bridges under gravity: Symmetry breaking and imperfect bifurcations of two-dimensional bridges. *J. Colloid Interface Sci.* **120**, 377–388 (1987).

[13] Gospodonov, I. D. *Axisymmetric liquid bridges-calculation of equilibria and stability for various contacting conditions.* Master's thesis, Cornell University (2002).

[14] Lowry, B. J. & Steen, P. Capillary surfaces: Stability from families of equilibria with application to the liquid bridge. *Proc. Roy. Soc. A* **449**, 411–439 (1995).

[15] Slobozhanin, L. A., Alexander, I. D. & Resnick, A. H. Bifurcation of equilibrium states of a weightless liquid bridge. *Phys. Fluids* **9**, 1893–1905 (1997).

[16] van Lengerich, H. B., Vogel, M. J. & Steen, P. H. Dynamics and stability of volume-scavenging drop arrays: Coarsening by capillarity. *Physica D* **238**, 531–539 (2008).

[17] Ramalingam, S. K. & Basaran, O. A. Axisymmetric oscillation modes of a double droplet system. *Physics of Fluids* **22**, 112111 (2010).

[18] Basaran, O. A. & DePaoli, D. W. Nonlinear oscillations of pendant drops. *Physics of Fluids* **6**, 2923–2943 (1994).

[19] Rayleigh, L. On the capillary phenomenon of jets. *Proc. R. Soc. Lond.* **29**, 71–97 (1879).

[20] Guckenheimer, J. *Nonlinear Oscillations, Dynamical Systems and Bifurcations of Vector Fields* (Springer, New York, 1983).

[21] Rand, R. H. *Topics in Nonlinear Dynamics with Computer Algebra* (Gorden and Breach, Langhome, 1994).

[22] Moon, F. C. Experiments on chaotic motions of a forced nonlinear oscillator: Strange attractors. *ASME J. Appl. Mech.* **47**, 638–644 (1980).

[23] Moon, F. C. & Holmes, P. J. A magnetoelastic strange attractor. *J. Sound Vib.* **65**, 275–296 (1979).

[24] Moon, F. C. & Holmes, P. J. Addendum: A magnetoelastic strange attractor. *J. Sound Vib.* **65**, 339 (1980).

[25] Feng, Z. C. & Leal, L. G. Nonlinear bubble dynamics. *Annu. Rev. Fluid Mech.* **29**, 201–243 (1997).

[26] Semerka, P., Birnir, B. & Banerjee, S. Regular and chaotic bubble oscillations in periodically driven pressure fields. *Phys. Fluids* **30**, 3342–3350 (1987).

[27] Oh, J. M., Kim, P. J. & Kang, I. S. Chaotic oscillation of a bubble in a weakly viscous dielectric fluid under electric fields. *Phys. Fluids* **13**, 2820–2830 (2001).

[28] Parlitz, U., English, V., Scheffczyk, C. & Lauterborn, W. Bifurcation structure of bubble oscillators. *J. Acoust. Soc. Am.* **88** (1990).

[29] Maconald, C. A. & Gomatam, J. Chaotic dynamics of microbubbles in ultrasonic fields. *Proc. IMechE, Part C: J. Mech. Eng. Science* **220** (2006).

[30] Simon, G., Cvitanovic, P., Levinsen, M. T., Csabai, I. & Horvath, A. Periodic orbit theory applied to a chaotically oscillating gas bubble in water. *Nonlinearity* **15** (2002).

[31] Szeri, A. J. & Leal, L. G. The onset of chaotic oscillations and rapid growth of a spherical bubble at subcritical conditions in an incompressible liquid. *Phys. Fluids A* **3**, 551–556 (1991).

[32] Chang, H. C. & Chen, L. H. Growth of a gas bubble in a viscous fluid. *Phys. Fluids* **29**, 3530–3536 (1986).

[33] Siddavaram, V. K. & Hornsy, G. M. The effects of gravity modulation on fluid mixing. part 1. harmonic modulation. *J. Fluid Mech.* **562**, 445–475 (2006).

[34] Hirsa, A. H., López, C. A., Laytin, M. A., Vogel, M. J. & Steen, P. H. Low-dissipation capillary switches at small scales. *Appl. Phys. Lett.* **86**, 014106 (2005).

[35] Wolf, A., Swift, J. B., Swinney, H. L. & Vasano, J. A. Determining lyapunov exponents from a time series. *Physica D* **16**, 285–317 (1985).

[36] López, C. A. Capillary switches: Science and applications. *Ph.D. thesis, Department of Mechanical, Aerospace, and Nuclear Engineering, Rensselae Polytechnic Institute* (2006).

[37] Parlitz, U., Wedekind, I., Lauterborn, W. & Merkwirth, C. Tstool and user manual, ver1.11. http:www.physik3.gwdg.de/tstool/ (2001). Free download (as of July 2008).

[38] Muller, I. & Strehlow, P. *Rubber and Rubber Baloons: Paradigms of Thermodynamics*, vol. 637 (Springer, 2004).

[39] Wente, H. C. A surprising bubble catastrophe. *Pac. J. Math.* **189**, 339–376 (1999).

[40] Bhandar, A. & Steen, P. H. Liquid-bridge mediated droplet switch: countering capillarity with electrokinetics. *PNAS* **17**, 127107 (2005).

[41] Golubitsky, M., Stewart, I. N. & Schaeffer, D. G. *Singularities and Groups in Bifurcation Theory: Vol. II.* (Springer-Verlag, 1988).

[42] Panton, R. *Incompressible Flow* (Wiley-Interscience, New York, 1996).

[43] Golubitsky, M. & Stewart, I. *The Symmetry Perspective: From Equilibrium to Chaos in Phase Space and Phsyical Space* (Brikhäuser Verlag, 2002).

[44] Gray, R. M. *Toeplitz and Circulent Matrices: A review* (Now Publishers, 2006).

[45] Slater, D. M., López, C. A., Hirsa, A. H. & Steen, P. H. Chaotic motions of a forced droplet-droplet oscillator. *Physics of Fluids* **20**, 092107 (2008).

[46] Hilborn, R. C. *Chaos and Nonlinear Dynamics* (Oxford University Press, 1994).

[47] Slater, D. M. & Steen, P. H. Bifurcation and stability of n coupled droplet oscillators with s_n symmetry. *Siam Journal of Applied Mathematics* (2011). (To Appear).

[48] Barany, E., Dellnitz, M. & Golubitsky, M. Detecting the symmetry of attractors. *Physica D* **67**, 66–87 (1993).

[49] Kroon, M. & Stewart, I. Detecting the symmetry of attractors for six oscillators coupled in a ring. *Inter. Jnl. of Bifurcation and Chaos* **5**, 209–229 (1995).

[50] Tchistiakov, V. Detecting symmetry breaking bifurcatioins in the system describing the dynamics of coupled arrays of josephson junctions. *Physica D* **91**, 67–85 (1996).

[51] Ashwin, P. & Nicol, M. Detection of symmetry of attractors from observations. part i: Theory. *Physica D* **100** (1997).

[52] Ashwin, P. & Nicol, M. Detection of symmetry of attractors from observations. part ii: An experiment with s_4 symmetry. *Physica D* **100** (1997).

[53] Dreyer, K. & Hickey, F. R. The route to chaos in a dripping water faucet. *American Journal of Physics* **59**, 619–627 (1991).

[54] Boys, C. V. *Soap Bubbles, Their Colors and Forces Which Mold Them* (Dover, New York, 1959).

[55] Orel, V. R. Stability of an incompressible fluid acted by surface tension forces. case of a doubly connected equilibrium surface. *J. Appl. Mech. Tech. Phys* **15**, 767 (1974).

[56] Frolov, V. A., Lizunov, V. A., Dunina-Barkovskaya, A. Y., Samsonov, A. V. & Zimmerberg, J. Shape bistability of a membrane neck: A toggle switch to control vesicle content release. *Proc. Natl. Acad. Sci. U.S.A.* **100**, 8698 (2003).

[57] Bian, X., Perlin, M., Schultz, W. W. & Agarwal, M. Axisymmetric slosh frequencies of a liquid mass in a circular cylinder. *Phys. Fluids* **15**, 3659–3664 (2003).

[58] Bostwick, J. B. & Steen, P. H. Capillary oscillations of a constrained liquid drop. *Phys. Fluids* **21**, 032108 (2009).

[59] Ciuryla, M., Chin, R., Hirsa, A. H. & Steen, P. H. Making and breaking liquid connections with a capillary switch. *PNAS* **17**, 127107 (2005).

[60] Ramalingam, S., Basaran, O., Lopez, C., Martinovic, I. & Hirsa, A. Computational analysis of coalescence and breakup between a capillary switch and a pendant drop. *Bull. Amer. Phys. Soc.* **52**, 188 (2007).

[61] Hirsa, A., Martinovic, I., Lopez, C., Basaran, O. & Ramalingam, S. Coalescence and breakup between a capillary switch and a droplet. *Bull. Amer. Phys. Soc.* **52**, 188 (2007).

[62] di Bernardo, M., Budd, C. J. & Kowalczyk, P. *Piecewise-smooth dynamical systems: Theory and Applications.*

[63] Awrejcewicz, J. & Lamarque, C. *Bifurcation and Chaos in Nonsmooth Mechanical systems* (World Scientific, 2003).

[64] J., D. E. *et al.* Auto 2007p: Continuation and bifurcation software for ordinary differential equations (with homcont). http://cmvl.cs.concordia.ca/auto (2007).

[65] Eisner, T. *For Love of Insects* (Belknap Harvard, Cambridge, 2003).

[66] Drechsler, P. & Federle, W. Biomechanics of smooth adhesive pads in insects: influence of tarsal secretion on attachment performance. *J. Comp. Physiol. A* **192**, 1213–1222 (2006).

[67] Waite, J. H. Adhesion a la moule. *Integr. Comp. Biol.* **42**, 1172–1180 (2002).

[68] Hanna, G. & Barnes, W. J. P. Adhesion and detachment of the toe pads of tree frogs. *J. Exp.Biol.* **155**, 103–125 (1991).

[69] Graham, L. *et al.* Characterization of a protein-based adhesive elastomer secreted by the australian frog notaden bennetti. *Biomacromolecules* **6**, 3300–3312 (2005).

[70] Federle, W., Riehle, M., Curtis, A. S. G. & Full, R. J. An integrative study of insect adhesion: Mechanics and wet adhesion of pretarsal pads in ants. *Integr. Comp. Biol.* **42**, 1100–1106 (2002).

[71] Autumn, K. *et al.* Adhesive force of a single gecko foot-hair. *Nature* **405**, 681–695 (2000).

[72] Autumn, K. *et al.* Evidence for van der waals adhesion in gecko setae. *Proc. Natl. Acad. Sci. USA* **99**, 12252–12256 (2002).

[73] Arzt, E., Gorb, S. & Spolenak, R. From micro to nano contacts in biological attachment devices. *Proc. Natl. Acad. Sci. USA* **100**, 10603–10606 (2003).

[74] De Souza, E. J., Brinkmann, M., Mohrdieck, C. & Arzt, E. Enhancement of capillary forces by multiple liquid bridges. *Langmuir* **24**, 8813–8820 (2008).

[75] Weaver, C. & Eisner, T. Television video: Secret weapons, see e.g. clip 1b0677_0049. *BBC Natural History Unit* (1983).

[76] Langbein, D. & Naumann, R. J. Double float zones. *Microgravity Sci. Technol.* **8**, 226–235 (1995).

[77] Plateau, J. A. F. Experimental and theoretical researches on the figures on equilibrium of a liquid mass withdrawn from the action of gravity. *A. Rep. Board Reg. Smithson. Inst.* 207–285 (1863).

[78] Eriksen, J. L. Equilibrium of bars. *J. Elas.* **5**, 6191–201 (1975).

[79] James, R. D. Co-existant phases in the one-dimensional static theory of elastic bars. *Arch. Ration. Mech. An.* **72**, 99–140 (1979).

[80] Maddocks, J. H. Stability and folds. *Arch. Rational Mech. An.* **99**, 301–328 (1987).

[81] Poincaré, H. Sur l'équilibre d'une masse fluide animée d'un mouvement de rotation. *Acta Mathematica* **9**, 259–380 (1885).

[82] Faria, J. Contact angle measurements of beetle oil used in the defense of the florida palm beetle. *Personal communication* (2003).

[83] de Gennes, P.-G., Brochard-Wyart, F. & Quéré, D. *Capillarity and Wetting Phenomena: Drops, Bubbles, Pearls, Waves* (Springer, New York, 2004).